Endao Han

Transient Dynamics of Concentrated Particulate Suspensions Under Shear

Springer

Springer Theses

Recognizing Outstanding Ph.D. Research

Aims and Scope

The series "Springer Theses" brings together a selection of the very best Ph.D. theses from around the world and across the physical sciences. Nominated and endorsed by two recognized specialists, each published volume has been selected for its scientific excellence and the high impact of its contents for the pertinent field of research. For greater accessibility to non-specialists, the published versions include an extended introduction, as well as a foreword by the student's supervisor explaining the special relevance of the work for the field. As a whole, the series will provide a valuable resource both for newcomers to the research fields described, and for other scientists seeking detailed background information on special questions. Finally, it provides an accredited documentation of the valuable contributions made by today's younger generation of scientists.

Theses are accepted into the series by invited nomination only and must fulfill all of the following criteria

- They must be written in good English.
- The topic should fall within the confines of Chemistry, Physics, Earth Sciences, Engineering and related interdisciplinary fields such as Materials, Nanoscience, Chemical Engineering, Complex Systems and Biophysics.
- The work reported in the thesis must represent a significant scientific advance.
- If the thesis includes previously published material, permission to reproduce this must be gained from the respective copyright holder.
- They must have been examined and passed during the 12 months prior to nomination.
- Each thesis should include a foreword by the supervisor outlining the significance of its content.
- The theses should have a clearly defined structure including an introduction accessible to scientists not expert in that particular field.

More information about this series at http://www.springer.com/series/8790

Endao Han

Transient Dynamics of Concentrated Particulate Suspensions Under Shear

Doctoral Thesis accepted by the University of Chicago, IL, USA

Springer

Endao Han
Joseph Henry Laboratories of Physics
Princeton University
Princeton, NJ, USA

To my family

The greatest obstacle to discovery is not ignorance—it is the illusion of knowledge.

—Daniel J. Boorstin

Supervisor's Foreword

How does the flow of a simple liquid change when particles are added to it? This was calculated by Albert Einstein in his PhD thesis over 100 years ago for small volume fractions of particles and subsequently extended by others to increasingly larger fractions. The result is that the suspension's resistance to applied shear, i.e., its viscosity, rises rapidly as more and more particles are added, to the point where all flow becomes arrested and the suspension's viscosity diverges. Underlying this divergence is the mechanism of jamming: beyond some critical volume fraction there simply is no longer room for neighboring particles to move with respect to one another and the whole suspension turns rigid, exhibiting a solid-like yield stress. Exactly when the jamming transition will occur, i.e., what value the critical volume fraction for jamming will assume, depends on details of the particle–particle interactions, which in turn is controlled by aspects such as the particles' shape and their surface properties. This type of isotropic jamming transition, controlled only by the particle density, describes the response to applied shear when the suspension is at rest. There is, however, another possibility to induce jamming, namely by driving an initially fluid suspension into a rigid state. This type of dynamic jamming occurs without any overall change in the volume fraction of particles. Instead, it is a consequence of the fact that shear reorganizes particles into anisotropic configurations. These configurations can establish load-carrying force chains as long as the particle volume fraction is not too low and the particle–particle contacts are sufficiently frictional. This thesis demonstrates how suspensions provide a model system for investigating such jamming by shear and it describes some of the remarkable consequences of the associated dynamic transformation that converts a fluid into a solid in a fully reversible manner.

A key aspect of jamming by shear in suspensions is that the process proceeds along rapidly moving fronts. Ahead of a front the suspension is still in its initial, fluid state, while behind the front the suspension has been transformed into a solid-like state. The thesis breaks new ground in establishing a constitutive framework that relates the properties of shear-jamming fronts, such as their propagation speed, to the applied shear stress and strain. In treating the dynamic, effectively transient conversion of fluid into solid, this significantly extends prior work on jamming

phase transitions, which only considered steady-state conditions. As the thesis shows, the local shear stress in the front region is set by the external stress applied at the boundary of the suspension. This enables a completely new way of performing stress-controlled experiments: by using the jamming fronts to generate conditions of controllable local stress, a method is introduced that overcomes a critical limitation of standard steady-state rheology, which cannot establish spatially uniform stress conditions in the interior of a concentrated suspension as jamming is approached. Finally, the thesis introduces high-speed ultrasound imaging as a powerful experimental technique to image propagating shear jamming fronts and extract the associated flow field.

As a whole, the work described here has significantly advanced our understanding of how jamming by shear can reversibly solidify a dense suspension and how this transformation depends on both the suspension properties and the kind of forcing that is applied. In concert with the powerful experimental techniques that are introduced, this opens up exciting new avenues for further research.

Chicago, IL, USA   Heinrich Jaeger
January 29, 2020

Acknowledgments

I want to express my most sincere gratitude to my advisor, Heinrich Jaeger, for all the support he consistently provided over the years. Nothing that I have been working on at Chicago could have been achieved without his insights, advice, encouragement, and patience. From Heinrich, I learned not only how to be a good scientist, but also how to be a better person. His influence on me is on a wide range of scales.

At the James Franck Institute, I am incredibly fortunate to have had the chance to be around faculty who are interested, open-minded, and treat every scientific problem seriously. I want to thank Sidney Nagel and Thomas Witten for many inspiring discussions and useful advice. Every moment with them was a memorable learning experience for me. Bozhi Tian always had great ideas during a discussion, and no matter when I sent him an email, he replied within a few minutes. I would also like to thank my thesis committee members, Arvind Murugan and Stephan Meyer, for their valuable inputs on my research and thesis.

I am very grateful to my collaborators at Chicago and other institutions. Matthieu Wyart showed me how an outstanding theorist thinks. Working with him was both challenging and exciting. Patrick La Riviere provided much help when we set up the ultrasound system, and his lectures kick-started my research with ultrasound. Yin Fang, Yuanwen Jiang, Xianghui Xiao, and Jin Wang opened doors for me that led to brand new research opportunities. I am delighted to have been part of this wonderful collaboration between people with such diverse backgrounds. I enjoyed working with Rui Zhang, Tonia Hsieh, Swapnil Pravin, and Kenneth Bader on various projects. I also appreciate the expertise of Qiti Guo, Justin Jureller, Helmut Krebs, Luigi Mazzenga, and John Phillips. They were always there when I was in trouble.

I am particularly thankful for my labmates. Ivo Peters is a good mentor, collaborator, and friend. I can never thank him enough for all the help he offered. I can hardly think of a better person than Nicole James to share an office with for five years. When I needed to work with any chemical that was not tap water, I asked Nicole first. Scott Waitukaitis and Qin Xu provided great help when I was an innocent rookie and had no idea what to do. I would also like to thank Victor

Parts of This Thesis Have Been Published in the Following Journal Articles

1. E. Han, I. R. Peters, and H. M. Jaeger. High-speed ultrasound imaging in dense suspensions reveals impact-activated solidification due to dynamic shear jamming. *Nature Communications*, 7:12243, 2016.
2. E. Han, N. Van Ha, and H. M. Jaeger. Measuring the porosity and compressibility of liquid-suspended porous particles using ultrasound. *Soft Matter*, 13(19):3506-3513, 2017.
3. E. Han, M. Wyart, I. R. Peters, and H. M. Jaeger. Shear fronts in shear-thickening suspensions. *Physical Review Fluids*, 3(7):073301, 2018.
4. E. Han, N. M. James, H. M. Jaeger. Stress controlled rheology of dense suspensions using transient flows. Physical Review Letters 123(24):248002, 2019.

Contents

Chapter 1
Introduction

In our daily lives, most materials we see are in one of the three states of matter: solid, liquid, or gas. When a material in one state is broken up into small particles and mixed with material in another state, rich and interesting phenomena can happen. For example, the air is so "soft" that most of the time one can hardly feel its existence. However, when many air bubbles are distributed in water, the foam that forms develops a rigidity that can hold its shape against gravity. Another famous example of such mixtures is a suspension of hard cornstarch particles in water, which is sometimes referred to as the "Oobleck" in Dr. Seuss' stories. One striking behavior of this solid-liquid mixture is that it flows like a viscous fluid under normal conditions, but solidifies under a sudden impact. The transition is so dramatic that people can jog or jump on the surface of such mixtures. When they stop moving, the material can no longer support their weight, and they slowly sink in. This reversible, dynamic fluid-solid transition is the main focus of this thesis.

Suspensions are mixtures of solid particles and liquids. The "particles" can have various shapes, such as spheres, rods, plates, etc. Here we consider suspensions comprised of spherical or non-spherical particles with an aspect ratio close to 1. At the same time, we only focus on non-Brownian suspensions, which means that the particles are so big (1–100 μm) that the effect of thermal motion can be ignored. Such systems are far from thermal equilibrium. We will show that the dynamic fluid-solid transition in concentrated non-Brownian suspensions is purely driven by mechanical stress. The applied stress plays two major roles: it provides kinetic energy for the system to explore phase space, and also it changes the interactions between the particles on a microscopic level. Such microscopic interactions at the points where surfaces of particles come into contact determine the stable (or unstable) configurations that can form locally, and subsequently control the macroscopic mechanical properties of the material. It is the complex interplay of forces arising from hydrodynamic interactions and frictional contacts that makes the behaviors of such suspensions so rich and fascinating.

1.1 Steady-State Rheology of Suspensions

The mechanical properties of suspensions are usually characterized by rheology experiments. Rheology is the study of the deformation and flow of matter [1]. Any deformation of a material can be written as the sum of a hydrostatic compression (Fig. 1.1a) and a pure shear (Fig. 1.1b) [2]. In practice, normally rheologists test the mechanical properties of a material by applying a simple shear as illustrated in Fig. 1.1c, which can be decomposed into a pure shear in two dimensions and solid body rotation. When a material is sheared, its volume keeps invariant.

If the material under simple shear is solid, when a tangential force F is applied on its upper surface with area A, a finite shear strain $\gamma \equiv \Delta x/y$ will be reached at the end as shown in Fig. 1.1c. The shear stress is defined as $\Sigma \equiv F/A$, and the ratio $G = \Sigma/\gamma$ is called the shear modulus, which represents the rigidity of the solid. In comparison, for a fluid sheared under constant stress, the deformation keeps accumulating. Now shear stress Σ controls the rate of deformation, or shear rate $\dot{\gamma} \equiv d\gamma/dt$, instead of the absolute amount of shear strain γ. For a fluid under simple shear, the ratio between Σ and $\dot{\gamma}$ is its viscosity $\eta = \Sigma/\dot{\gamma}$ [3].

The research on how solid particles change the viscosity of suspensions dates back to Einstein [4]. In his Ph.D. thesis, he calculated the viscosity of very dilute suspensions where the interactions between particles can be ignored, and found a linear relationship between the viscosity of the suspension and the volume fraction of the particles (also called the packing fraction) ϕ:

$$\eta_r \equiv \frac{\eta}{\eta_0} = 1 + 2.5\phi, \tag{1.1}$$

where η is the viscosity of the suspension, η_0 is the viscosity of the solvent or the liquid phase in the suspension, and η_r is the relative viscosity. For denser (more concentrated) suspensions, higher order terms need to be taken into consideration [5, 6].

On the end of the ϕ axis, we have the phenomenon of jamming [7, 8]. Jamming occurs when the particle concentration becomes so large, and there is so little space
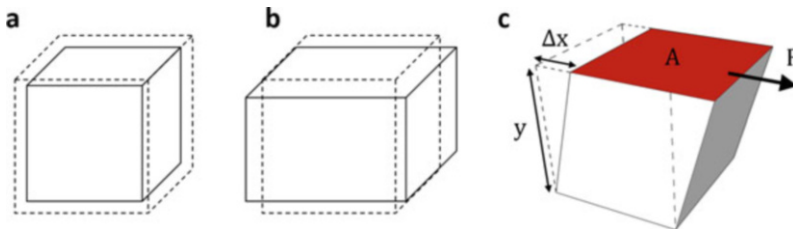
Fig. 1.1 Examples of how a material deforms: (**a**) hydrostatic compression, (**b**) pure shear, (**c**) simple shear. The dashed black lines represent the shape of the material before deformation, and the solid black lines represent the shape after deformation. In (**c**), a tangential force F is applied on the red surface, which has an area of A

for each particle to move that the whole system cannot flow anymore. This critical packing fraction is named the jamming packing fraction ϕ_J. For mono-disperse hard spheres, the jamming point approaches random close packing $\phi_J = \phi_{RCP} \approx 0.64$ as the system size goes to infinity [7]. For a dense suspension, while ϕ approaches ϕ_J, the viscosity diverges. This behavior is captured by a more general relation between η_r and ϕ,

$$\eta_r = \left(1 - \frac{\phi}{\phi_J}\right)^{-\alpha},\tag{1.2}$$

which is based on the work of Maron and Pierce ($\alpha = 2$) [9], Krieger and Dougherty ($\alpha = 2.5\phi_J$) [10], Brady [11], and others. Krieger and Dougherty's model [10] reproduces Einstein's equation (Eq. 1.1) in the low-ϕ limit, but according to the experimental results obtained from both colloidal and non-colloidal suspensions, Maron and Pierce's model [9] better describes the data [12]. Here in this thesis we use $\alpha = 2$.

Very dilute suspensions are Newtonian fluids, which means that their viscosity does not change with how fast or how strongly they are sheared. Air, water, and glycerol are all Newtonian fluids. Their viscosity is independent of the shear rate $\dot{\gamma}$. At the same time, there are fluids whose viscosity changes when they are sheared faster or slower, and these are the so-called non-Newtonian fluids. If the viscosity of a fluid increases with $\dot{\gamma}$, it is a shear thickening fluid, and a cornstarch-water mixture is a typical example. In comparison, if the viscosity decreases while $\dot{\gamma}$ increases, the fluid is a shear thinning fluid, such as paint or blood. Another type of non-Newtonian fluid does not flow unless the applied shear stress exceeds a certain threshold, which is called the yield stress. These fluids are referred to as Bingham fluids [1]. Shaving foam and toothpaste are Bingham fluids.

For most suspensions, the viscosity is not only a function of the packing fraction ϕ. As shown in Fig. 1.2 [13], they can exhibit complex non-Newtonian behaviors under different steady-state driving conditions.[1] Correspondingly, various mechanisms have been proposed. At low shear stress, suspensions can be Newtonian (at low ϕ), shear thinning, or have non-zero yield stress (at high ϕ). The possible causes of shear thinning include attractive interactions [14, 15], repulsive interactions [16], changes in particle structure (entropic) [17], plus others [18]. As the applied shear stress increases, normally there is a Newtonian regime where η_r remains constant, and then the suspension shear thickens. At a relatively low packing fraction, typically up to $\phi \approx 0.4$, the increase in η_r is mild and continuous. This behavior is named continuous shear thickening (CST) [19]. To explain CST, Brady and Bossis introduced a model based on hydrodynamic interactions between particles [20, 21]. The model demonstrates that at high enough Péclet number, particles form clusters due to hydrodynamic couplings. This model is normally referred to as the hydrocluster model, and hydroclusters have been observed experimentally with confocal microscopy [17]. At higher packing fractions, typically above $\phi \approx 0.5$, a

---

[1]Note that Eq. (1.2) is valid only when the viscosity $\eta_r(\phi)$ is measured in the "Newtonian regime."
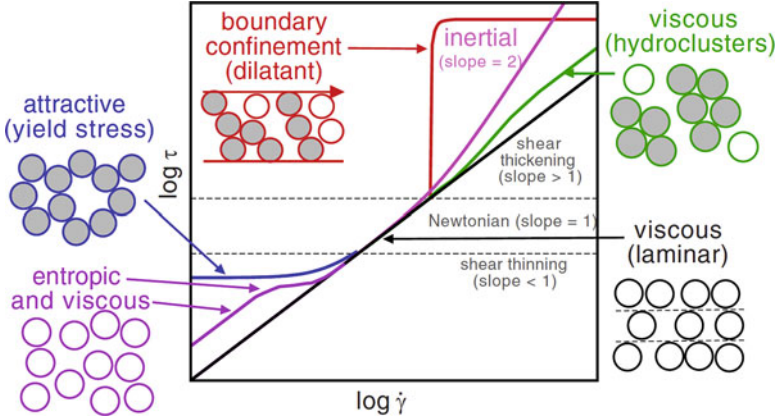
Fig. 1.2 Different regimes of suspension rheology and corresponding mechanisms. In this plot, $\dot{\gamma}$ is the shear rate and τ represents the shear stress. Figure reproduced from E. Brown and H. M. Jaeger, Shear thickening in concentrated suspensions: phenomenology, mechanisms and relations to jamming, Rep. Prog. Phys. (2014) [13] with permission

more dramatic increase in η_r can be observed, where η_r shoots up discontinuously as a function of $\dot{\gamma}$ [22]. Consequently, this behavior is named discontinuous shear thickening (DST). For steady-state rheology, Brown and Jaeger [23] related DST to frustrated dilation, which pointed out the significance of direct particle–particle contacts in the process of shear thickening [24, 25].

1.2   Shear Jamming in Dry Granular Materials and Dense Suspensions

Jamming is the onset of rigidity in granular materials [7, 8, 14]. For frictionless particles, jamming can be achieved by increasing the packing fraction ϕ across the jamming point ϕ_J [26]. Applied shear stress Σ unjams the system when Σ exceeds the yield stress Σ_{yield}. Interestingly, when the interaction between particles is frictional, the system can be jammed by shear at a packing fraction below ϕ_J [27]. As shown in Fig. 1.3a, for a two-dimensional dry granular system under quasi-static pure shear, while ϕ is in the range of $\phi_S < \phi < \phi_J$, the system goes through three different states as Σ increases: In the fragile state (red), the strong force networks[2] only percolate in the compression direction, so perturbations in the transverse direction can cause instability in the system [8, 27]. At higher Σ, the strong force networks percolate in all directions, and the system reaches a shear-jammed state (green). At even higher Σ, the jammed solid yields and goes into

---

[2]Strong force is defined as $F > F_{ave}$, where F is the local contact forces, and F_{ave} is the average of F across the whole system [27].
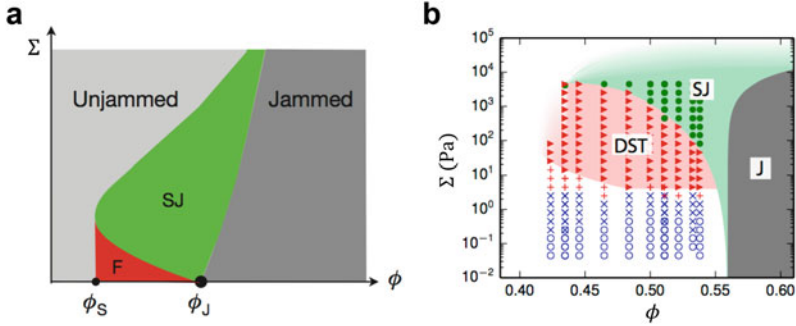
Fig. 1.3 Shear jamming state diagrams for dry grains (**a**) and suspensions (**b**). F represents the fragile state, DST represents discontinuous shear thickening, SJ represents the shear-jammed state, and J represents the frictionless jammed state. (**a**) reproduced from D. Bi et al., Jamming by shear, Nature (2011) [27]. (**b**) reproduced from I. R. Peters, S. Majumdar, and H. M. Jaeger, Direct observation of dynamic shear jamming in dense suspensions, Nature (2016) [28]

the unjammed regime (light gray). Jamming by shear was also found in frictionless systems [29] or with weakly attractive particles [30] by numerical simulations.

Shear jamming in dense suspensions was observed by Peters et al. [28] with a wide gap Couette cell. The macroscopic feature of shear-jammed suspensions is that they develop a non-zero shear modulus.[3] A state diagram has been mapped out for dense suspensions under steady-state driving conditions, as shown in Fig. 1.3b. Similar to dry granular systems, in suspensions, the transitions are also controlled by ϕ and Σ. One significant difference is that at low Σ, suspensions flow like a viscous fluid because of the lubrication interaction between the particles. The strongly non-Newtonian rheological properties become most pronounced at high ϕ and Σ, where suspensions start to exhibit characteristics also found in dry granular material [8, 26, 27, 31, 32]. Recent experiments [25, 33–37] and numerical simulations [38–41] point to the existence of a stress threshold above which the dominant interaction between particles switches from hydrodynamic lubrication to frictional contact forces.

In dry granular systems, there are three interesting thresholds: the minimum packing fraction needed for shear jamming ϕ_S, the onset stress $\Sigma_{SJ}(\phi)$ of shear jamming, and a strain scale that represents the necessary deformation to rearrange the particles from a uniformly distributed initial state into contact networks [42]. In suspensions there are three scales as well: a lower boundary for shear jamming at packing fraction ϕ_m, a stress threshold Σ^* that is related to the breakdown of the lubrication layer between particles, and a strain scale γ^*. The stress scale Σ^* is relatively well understood based on studies using steady-state rheology. In

---

[3]Some literature does not clearly distinguish shear thickening and jamming. Sometimes discontinuous shear thickening is referred to as "temporary jamming." In this thesis, jamming is only designated to a state that does not flow under applied stress (with a non-zero shear modulus) during the time scale of the experiments.

contrast, before the work in this thesis, ϕ_m was never tested experimentally, and the importance of γ^* was not recognized, especially for transient phenomena. These will be discussed in Chap. 4.

1.3 Wyart–Cates Model for Steady-State Rheology

The basis of a phenomenological model developed by Wyart and Cates [43] is that there is a transition in particle–particle interactions from hydrodynamic lubrication forces to frictional contact forces and this transition is controlled by stress. This model unifies CST, DST, and jamming under a common framework for suspensions under conditions of steady-state driving. The central ideas are as follows:

1. Frictional contacts between particles will be made beyond a characteristic pressure P^*. The fraction of frictional contacts $f(P)$ should be a smooth function that grows with P, such as

$$f(P) = 1 - \exp(-P/P^*). \tag{1.3}$$

2. The packing fraction ϕ_J at which jamming occurs is known to depend on the friction coefficient [44]. In suspensions, ϕ_J must then depend on P, and this can be captured by a linear interpolation

$$\phi_J(P) = f(P)\phi_m + [1 - f(P)]\phi_0, \tag{1.4}$$

where ϕ_0 and ϕ_m are the frictionless and frictional jamming packing fractions, respectively. The exact value of ϕ_m is controlled by the friction between particles. Importantly, "friction" here is a phenomenological parameter that can have different microscopic origins, which include direct solid–solid contact [33, 41], surface roughness of particles [45, 46], interactions between polymer brushes [36], or hydrogen bonding [47].

3. When a suspension with packing fraction ϕ is under shear, the ratio between normal stress P and shear rate $\dot{\gamma}$ diverges at ϕ_J (see Eq. (1.2)):

$$\frac{P}{\dot{\gamma}} \propto \left[1 - \frac{\phi}{\phi_J(P)}\right]^{-\alpha}. \tag{1.5}$$

For frictionless particles the exponent α can be computed analytically, leading to $\alpha = 2.85$ [31], whereas for frictional particles it is smaller [48]. Here we pick $\alpha = 2$, which is in good agreement with previous experimental results [34, 49, 50].

4. Equations (1.3)–(1.5) allow one to compute $P(\dot{\gamma})$, eventually leading to a state diagram predicting CST, DST, and jamming in the (ϕ, P) plane. A further
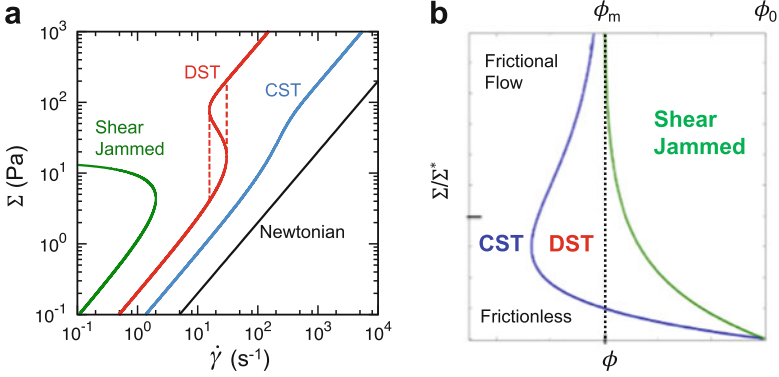
Fig. 1.4 Wyart–Cates model for suspension rheology. (**a**) Exemplary Σ-$\dot{\gamma}$ relations for Newtonian, CST, DST, and SJ suspensions. (**b**) State diagram. Panel (**b**) reproduced from M. Wyart and M. E. Cates, Discontinuous shear thickening without inertia in dense non-Brownian suspensions, Phys. Rev. Lett. (2014) [43]

prediction of the shear stress can be obtained following the relation $\Sigma = \mu P$, where μ is the macroscopic friction coefficient [34]. In principle, μ depends on P and ϕ, but in practice, the dependence is weak; thus μ can be well approximated as a constant of order one. Therefore, we can replace P with Σ, and P^* with Σ^* in Eqs. (1.3)–(1.5). Then Eq. (1.5) will have the same form as Eq. (1.2).

Some Σ-$\dot{\gamma}$ curves predicted by the Wyart–Cates model are shown in Fig. 1.4a. At $\phi = 0$, the system only consists of the solvent, which is a Newtonian fluid. For a denser suspension, the curve continuously shifts towards larger η as Σ increases. In the CST regime, there is a one-to-one correspondence between $\dot{\gamma}$ and Σ. However, at even higher ϕ, the Σ-$\dot{\gamma}$ curve becomes sigmoidal. For curves like this, stress-controlled experiments and rate-controlled experiments will lead to different results, because for each Σ there is only one corresponding $\dot{\gamma}$, but for some $\dot{\gamma}$, there are more than one possible Σ. A stress-controlled experiment will reproduce the solid red curve in Fig. 1.4a, while in a rate-controlled experiment discontinuous jumps will happen as shown by the dashed red lines, and there will be hysteresis [51]. In this regime, we obtain DST. When $\phi > \phi_m$, the Σ-$\dot{\gamma}$ curve intersects with the vertical axis where $\dot{\gamma} = 0 \text{ s}^{-1}$. At the intersection, the suspension is in a state of zero shear rate, but non-zero shear stress, which means that it must have developed a non-zero shear modulus, i.e., turned into a solid. The stress at the intersection, therefore, is the onset stress of shear jamming Σ_{SJ}.

From the Σ-$\dot{\gamma}$ curves, a state diagram is obtained, as shown in Fig. 1.4b. In steady-state rheology, the state of a suspension is controlled by two parameters ϕ and Σ. Here we call it the $\eta(\phi, \Sigma)$ rheology. This phenomenological model allows us to predict the various behaviors of an unknown suspension by measuring four parameters (η_0, ϕ_0, ϕ_m, and Σ^*) with a rheometer, without the necessity of knowing any details about the material on the microscopic level.

1.4   Dynamic Jamming and Transient Flows Under Impact, Extension, and Shear

Although steady-state rheology of dense suspensions has been studied extensively in the past decade or so, the experimental observation of shear jamming under steady-state conditions occurred only very recently [28]. In contrast, dynamic jamming of dense suspensions was noticed much earlier in transient phenomena. Under a wide range of dynamic conditions, dense suspensions can undergo a fluid-solid transformation, for example, ahead of quickly sinking objects [52, 53], during sudden impact at their free surface [54–57], under shear [28] or during rapid extension [58]. Detailed investigation of the dynamics during impact has shown how such solidification is associated with a propagating front that converts fluid-like, unjammed suspension into a solid-like, jammed material in its wake [54, 59]. This dynamic front moves much faster than the impactor itself.

To explain "impact-activated solidification" and the formation of the front, a model was proposed [54] that assumed the impact pushes the particles closer together until they jam. This densification scenario was based on the standard jamming phase diagram for frictionless hard particles, where entry into a jammed state requires an increase in particle packing fraction ϕ [7]. Since the volume of particles is conserved, the front propagation speed U_f along the direction of impact then is related to the impactor speed U_p via [60]

$$U_\mathrm{f} = \frac{\phi_\mathrm{J}}{\phi_\mathrm{J} - \phi} U_\mathrm{p}, \tag{1.6}$$

where ϕ_J is the packing fraction at which jamming occurs and $\phi\,(<\phi_\mathrm{J})$ is the packing fraction of the initially unjammed suspension at rest. The closer the initial packing fraction is to jamming, the faster the front will propagate, and in principle the ratio $U_\mathrm{f}/U_\mathrm{p}$ diverges at ϕ_J. This model shows excellent agreement with measurements of U_f in systems where the local packing fraction can change easily, such as dry granular particle layers that are being compacted snowplow-like from one end [60].

However, this model has certain limitations. Firstly, since compression is required, it does not explain why suspensions can also jam under simple shear or extension. Secondly, since the liquid is effectively incompressible for speeds U_p that are only several meters per second, compression would imply migration of particles. Since the particles are non-Brownian, the concentrated regions would be unable to return to the original state when the stress is removed, which contradicts experimental observations. Lastly, as shown in [59] where the flow field in 2D was measured accurately, the suspension does not turn into a jammed solid before the front interacts with a solid boundary. A small but non-zero velocity gradient was observed behind the freely propagating front, which means the suspension is only solid-like, but not a solid yet. All these issues point to the need for a revised and more detailed understanding, and in this thesis, we will get there step by step.

1.5   The Scope of This Thesis

The primary goal of this thesis is to understand the transient dynamics of dense particulate suspensions, especially in the shear jamming regime. The main body is comprised of four parts: In Chap. 2 we introduce several ultrasound techniques that are useful for characterizing the properties of suspensions, including imaging interior flows, measuring the bulk modulus using the speed of sound, and measuring the porosity of porous microparticles. In Chap. 3 we use high-speed ultrasound imaging to non-invasively probe how the interior of a dense suspension responds to impact. By measuring the speed of sound we demonstrate that the solidification proceeds without any detectable increase in packing fraction, and by imaging the evolving flow field we find that the shear intensity is maximized right at the jamming front. Taken together, this provides direct experimental evidence for jamming by shear, rather than densification, as driving the transformation. To develop a quantitative description of such transient flows, in Chap. 4, we study the fronts that appear when dense suspensions are subjected to sudden shear in a quasi-one-dimensional system. Based on the experimental findings, we point out that the $\eta(\phi, \Sigma)$ rheology is not sufficient to explain the transient flows. To fix this, we generalize the original Wyart–Cates model by introducing a sole additional parameter: the characteristic strain scale that controls the crossover from start-up response to steady-state behaviors. Chapter 5 demonstrates how transient shear flows can be used to perform stress-controlled rheology tests. This technique enables us to map out properties of dense suspensions in the shear jamming regime, which is difficult if not impossible with standard steady-state rheology. Chapter 6 contains conclusions and outlines some open questions that future work might be able to address.

Chapter 2
Ultrasound Techniques for Studying Suspensions

2.1 Introduction

Compared to the Higgs boson or exoplanets, colloidal or non-colloidal particles are much easier to visualize. However, imaging is still a challenging task for soft matter experiments in general, because they may involve a wide range of length scales, require a high temporal resolution, need information deep in the bulk, or deal with optically opaque materials [61]. These are the challenges we must meet to understand the transient dynamics of dense suspensions.

As an important diagnostic imaging technique, ultrasound has been studied extensively in medicine. At the same time, it has become a useful tool for granular material and suspensions, either to make observations or to manipulate the tested material. For example, diffusion acoustic wave spectroscopy (DAWS) was developed to measure relative velocity and strain rate in suspensions [62]. Combined with steady-state rheology, ultrasound speckle velocimetry has been used to measure the flow field [63, 64]. The transmission of compression or shear waves can be used to probe the mechanical properties of jammed granular materials [65–68]. As a well-developed technique, ultrasound has much potential for soft matter experiments, especially for aqueous but optically opaque materials.

One advantage of ultrasound is its high acquisition frequency. One major limitation, however, is the attenuation due to scattering or absorption, which limits the penetration depth of the signals [69]. Standard medical ultrasound has a frequency f that ranges approximately from 1 to 20 MHz, and is coupled[1] to water or soft tissues, in which the speed of sound c is around 1500 m/s. Therefore the range of wavelength $\lambda = c/f$ covered is about 0.1–1 mm. For suspensions comprised of microparticles, λ usually is at least one order of magnitude larger than the particle diameter, so scattering is relatively weak. The absorption, though, can

---

[1]Here "couple" means that the acoustic impedance is matched. Details see Sect. 2.6.

still be significant, especially in highly viscous fluids such as dense suspensions. Higher frequency leads to finer spatial resolution but stronger absorption, thus it shortens the range of view into the material. Ultrasound imaging with a spatial resolution beyond the diffraction limit has been achieved [70], but the temporal resolution has to be sacrificed to accumulate data for statistics. Depending on the purpose of the observation, we need to find a balance between temporal resolution, spatial resolution, and penetration depth.

For suspensions, there are three essential length scales: the surface interaction is at nanometer or sub-nanometer scales, the particle diameter is one micron to tens of microns, and the characteristic length scale in the transient shear flow is of order 1 mm. Even with the ultra-fast ultrasound localization microscopy (uULM) technique (a few μm resolution) [70], it is difficult to visualize individual particles. Luckily, sometimes to model a system, we only need to choose the "appropriate" length scale and do not need to have a complete understanding of the details at smaller scales [71]. As will be discussed later, models can be developed treating suspensions as a continuum. Experimentally, this allows us to push the limit of temporal resolution and penetration depth while we only aim for a "reasonable" spatial resolution.

2.2   Introduction to the Ultrasound System

The apparatus we used for the experiments described in this thesis was a Verasonics Vantage 128 research ultrasound platform, which is shown in Fig. 2.1a. It has three main parts: the data acquisition hardware, the host controller computer, and an ultrasound transducer. The data acquisition hardware has 128 independent channels that control and communicate with the ultrasound transducer. Transducers are made of piezoelectric materials that transform pressure signals into electrical signals and vice versa. Our ultrasound system works with transducers with a linear array, a curved array, or a phased array. We primarily used a Philips L7-4 linear array transducer, which has a flat surface as schematically illustrated in Fig. 2.1b. Its working part is comprised of a one-dimensional linear array of 128 piezoelectric elements. The width of each element in the x direction is 0.250 mm, and the distance between the centers of adjacent elements is 0.298 mm. In the y direction, each element has a length of about 7 mm, but the beam is focused, so the transducer only scans a thin sheet in the x-z plane.

A transducer can be used as an ultrasound transmitter, receiver, or both (transceiver). Each element in the array can transmit or receive ultrasound signals independently. The shape, duration, frequency, and other parameters of the transmitted signal are all adjustable according to the specific application. Our most commonly used transmitted signal is a $f = 5.00$ MHz sinusoidal wave with the amplitude modulated by a Gaussian envelope, as shown in Fig. 2.1c. When all the elements transmit the same signal simultaneously, we get a plane wave that
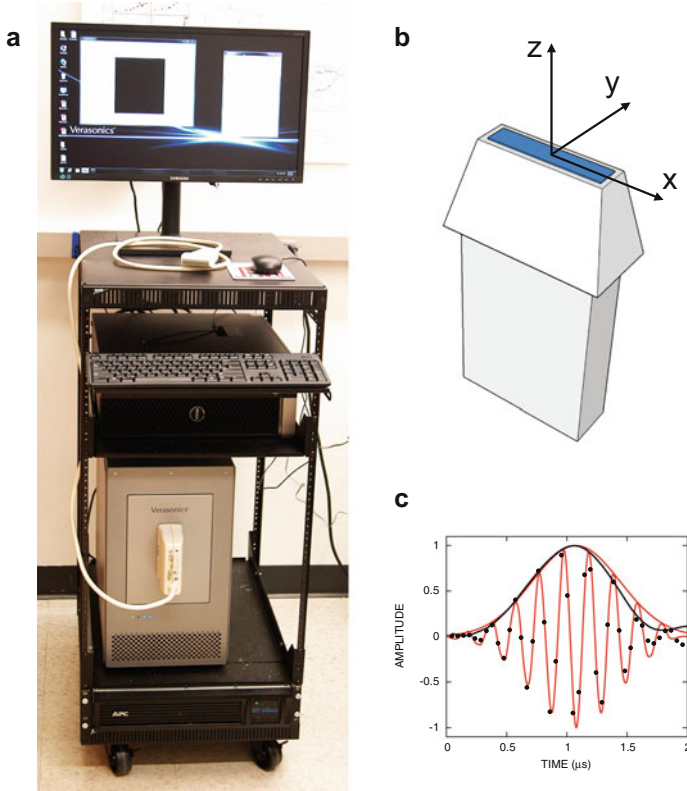
Fig. 2.1 Introduction to the ultrasound system. (**a**) Photo of the Verasonics Vantage 128 system with a Philips L7-4 transducer connected. (**b**) A schematic illustration of an L7-4 transducer, with the conventional coordinate system labeled. (**c**) An exemplary transmitted signal. The red curves show the functional form of the signal and its Gaussian envelope. The black dots show the measured transmitted signal reflected from a surface parallel to the $x - y$ plane. The black line is the envelope of the reflected signal. The amplitude of the signals is normalized by the peak heights of the envelopes

propagates in the z direction. By controlling the relative transmission time of each element, we can also realize tilted plane waves, beam sweeping, or focused beams.

After sending out a signal, the transducer is switched to the receiving mode. For $f = 5\,\text{MHz}$ signals, we set the center frequency of data acquisition f_c to be $5.208\,\text{MHz}$. The actual sampling frequency is $4 \times f_c = 20.832\,\text{MHz}$, so the system acquires a bit more than 4 data points in one period of the transmitted signal. The bandwidth of the L7-4 transducer is 4–7 MHz. The original acquired signal is called the radio frequency (RF) data, which is a time series of the amplitude of the echo signals. Each ultrasound element provides one such series, so with all 128 elements, we obtain an $N_{\text{RF}} \times 128$ matrix, where N_{RF} is the number of acquisitions. We chose N_{RF} based on the maximum depth z_{max} required for the images:

$$N_{\mathrm{RF}} \geq \frac{z_{\max}}{c} \cdot 4 f_{\mathrm{c}} \cdot 2, \tag{2.1}$$

where c is the speed of sound, $4 f_{\mathrm{c}}$ is the data acquisition rate, and the factor 2 is because of the round-trip of the signals. For image reconstruction, the RF data are transformed into in-phase and quadrature (IQ) components. Then two-dimensional brightness mode (B-mode) images can be reconstructed based on the IQ data. In the experiments, we had the freedom to use the RF data, the IQ data, or the B-mode images depending on the purpose of the measurement. The data acquisition module can take RF data at a very high rate, and save the data in the local memory. Transferring data to the host computer takes more time, and following that is the slowest process—image reconstruction. The highest frame rate can be obtained by taking RF data consecutively, then transferring and processing the data afterward. The image depth $z_{\max}$ is also a limiting factor. The time interval between two adjacent frames should not be shorter than $2z_{\max}/c$ to make sure that the echoes are from one transmitted signal only. The maximum frame rate we used for imaging when all 128 elements were active was 10, 000 frames per second. It can be even faster if the imaging window is shrunk.

2.3   Speed of Sound Measurements

The speed of sound c (phase speed of the compression wave) in a homogeneous and isotropic fluid is

$$c = \sqrt{\frac{1}{\kappa \rho}} = \sqrt{\frac{K}{\rho}}, \tag{2.2}$$

where ρ is the density, κ is the compressibility, and $K = 1/\kappa$ is the bulk modulus [69]. For a solid, the speed of sound depends on the shear modulus G as well

$$c = \sqrt{\frac{K + \frac{4}{3}G}{\rho}}. \tag{2.3}$$

So for liquids and soft solids ($G \ll K$), a speed of sound measurement is a convenient way to obtain their bulk modulus.

For a dilute suspension of solid non-porous particles in a liquid, Eq. (2.2) still applies, but ρ and κ should be replaced by the effective density ρ_{eff} and the mean compressibility $\bar{\kappa}$, respectively. In the long wavelength limit, where the ultrasound wavelength λ is much larger than the particle size, the mean density $\bar{\rho}$ and compressibility $\bar{\kappa}$ of the suspension can be written as

$$\bar{\rho} = \phi\rho_s + (1 - \phi)\rho_l,$$
$$\bar{\kappa} = \phi\kappa_s + (1 - \phi)\kappa_l,$$

(2.4)

where ϕ is the volume fraction of the solid particles. The subscripts "s" and "l" represent "solid" and "liquid," respectively. For suspensions in which the particles and the liquid have the same density (density-matched suspensions), the effective density and the mean density are the same [72, 73]: $\rho_{eff} = \bar{\rho}$. However, for suspensions that are not density-matched, a correction term ρ_δ has to be added: $\rho_{eff} = \bar{\rho} + \rho_\delta$. The detailed form of ρ_δ is introduced in Appendix A. According to Eqs. (2.2) and (2.4), by measuring c, we can calculate the compressibility of the suspending particles κ_s if we know ϕ, or measure ϕ if we know κ_s. For porous microparticles, we can even use this method to measure their porosity, as will be discussed in Sect. 2.4

A schematic illustration of the experimental setup for the speed of sound measurements is shown in Fig. 2.2. The suspension samples were placed in a rectangular container. Within the four vertical walls of the container, three were aluminum and one was acrylic. The dimensions of the container were: length $l = 16.4$ mm and width $w = 29.0$ mm as labeled in the figure. The thickness of the acrylic wall was 6.1 mm. We adjusted the position and direction of the transducer so that the ultrasound beam propagated within a horizontal plane, and consequently, it was perpendicular to the acrylic surface of the container. The transmitted ultrasound signal was a pulse of a sinusoidal wave at $f = 5$ MHz, modulated with a Gaussian profile, as shown in Fig. 2.1c. After being emitted from the transducer, it traveled through the water toward the front (acrylic) wall of the container, passed through this wall, penetrated the suspension, and finally hit the back (aluminum) wall of the container. During this process, the wave was reflected from three interfaces: the water–acrylic interface, the acrylic–suspension interface, and the suspension–aluminum interface. Consequently, there are three major peaks in the time series of the received signal, as shown in Fig. 2.2c. The time difference between P2 (acrylic–suspension interface) and P3 (suspension–aluminum interface) is the round-trip time of flight τ of the ultrasound signal in the tested suspension. Since the length l of the container is fixed, the measured time τ is inversely proportional to the speed of sound c_{sample} in the tested sample. Since the speed of sound in pure water c_{water} is well known, here we use it as a reference, thus

$$c_{sample} = \frac{\tau_{water}}{\tau_{sample}} c_{water}.$$

(2.5)

The temperature of the water in the tank and the temperature of the suspension samples were both kept at $20.8 \pm 0.4\,°C$ during the experiment. At this temperature $c_{water} = 1484.8 \pm 1.2$ m/s [74, 75]. We measured the time of flight in deionized water and got $\tau_{water} = 22.127 \pm 0.007$ μs. The mean and standard deviation are from 13 independent measurements.
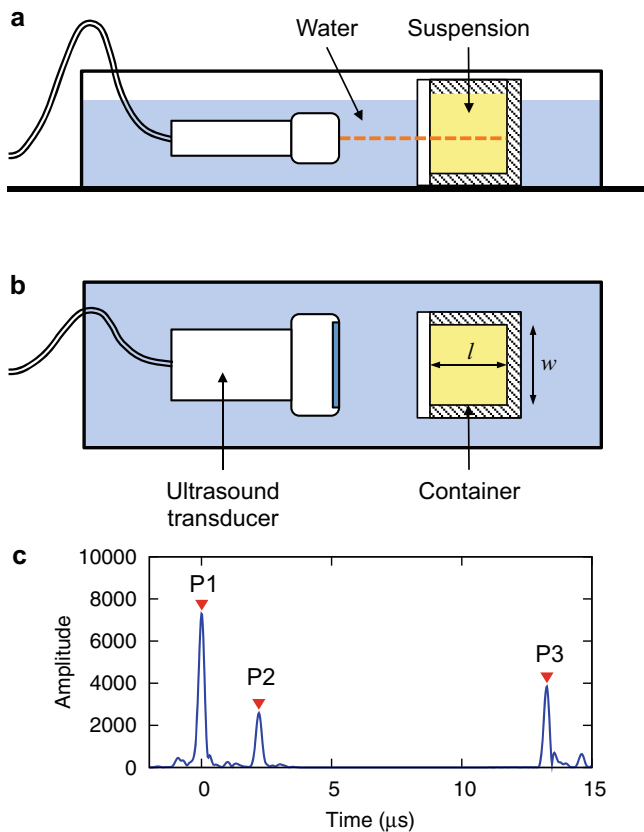
Fig. 2.2 Experimental setup for the speed of sound measurement: (**a**) side view, (**b**) top view. The ultrasound transducer was submerged in water, and it scanned a horizontal slice as represented by the dashed orange line. The tested material, which can be either a liquid or a soft solid, was placed in the rectangular container. Shaded parts of the container were made of aluminum, and the white wall was acrylic. To show it more clearly, we plot the container in cross-section in panel (**a**). (**c**) Envelope of an exemplary received RF signal. The three peaks labeled are reflections from the water–acrylic interface (P1), the acrylic–sample interface (P2), and the sample–aluminum interface (P3), respectively

2.4 Measurement of Porosity and Bulk Modulus of Microparticles in Liquids[2]

A key parameter controlling the mechanical properties of suspensions is the volume fraction of the solid particles ϕ. For suspensions with non-porous particles such as solid glass or acrylic beads, ϕ can be easily calculated using the masses and densities

---

[2]This section is based on [76].

of the corresponding liquid and solid. However, when there are porous particles, obtaining accurate values for ϕ becomes difficult, because some of the liquid will be absorbed into the pores and enclosed by a solid outer shell. Cornstarch suspensions are widely used as a model system for shear thickening fluids, but the starch granules are porous: They are mostly comprised of amylose and amylopectin, which are hydrophilic polymers [77]. These polymers tend to form a layered structure with concentric growth rings [78] and small voids between adjacent lamellae [77]. When immersed in an aqueous solvent, starch particles will absorb some of the solvent [79, 80], which makes it difficult to ascertain the correct value for the particle volume fraction in the suspension.

As far as the rheological properties of a suspension are concerned, the packing fraction that matters is the effective volume occupied by the particles. For any given particle, this is the space enclosed by the outer surface that can come in contact with neighboring particles. Therefore, the volume of hollow regions and connected pores inside a particle should still count as the "effective" particle volume. Given the difficulty of reliably extracting the particle porosity in systems like cornstarch, there has been no general, agreed-upon method for calculating the volume fraction. Typically, the volume of the particles is considered as the mass of the dry particles divided by the density of the corresponding material, and the porosity of the particles is ignored. In the literature, a cornstarch suspension loses the ability to flow (or is reported as "hard to handle") when this dry-material-based volume fraction reaches 0.42–0.45 [53, 55]. Compared to the random close packing of mono-disperse spheres ($\phi \approx 0.64$), or the packing fraction at which glass spheres exhibit strongly non-Newtonian effects such as discontinuous shear thickening ($\phi \approx 0.58$) [81], this value is considerably smaller. It is known that non-spherical particles, poly-dispersed particles, and particles with rough surfaces could have a higher jamming packing fraction. However, even considering all these factors, this discrepancy still seems too large. To compare cornstarch suspensions with other particulate suspensions, dry granular systems [7, 27] or theoretical calculations [38, 43], it is therefore essential to find accurate volume packing fractions by accounting for the particle porosity. We will now demonstrate how to achieve this by measuring the speed of ultrasound.

Here we define the particle porosity ψ as the ratio between the pore volume and the total volume enclosed by the particle surface. In a suspension, when the pores become filled with the suspending solvent, the volume fraction of the saturated particles ϕ is

$$\phi = \frac{1}{1 - \psi} \phi_M, \qquad (2.6)$$

where ϕ_M is the mass fraction given by Eq. (B.1). By plugging Eqs. (2.4) and (2.6) into Eq. (2.2), we get

$$\frac{1}{1 - \psi}(\kappa_s - \kappa_l)\phi_M + \kappa_l = \frac{1}{c^2 \rho_{\text{eff}}}. \qquad (2.7)$$

Here c can be directly measured, and the method to obtain the effect density ρ_{eff} is described in Appendix A (Eq. A.2). Equation (2.7) is the essential equation for the data analysis. For suspensions in the same solvent (thus the same κ_1), $\frac{1}{c^2 \rho_{\text{eff}}}$ is a linear function of ϕ_M. Its slope $S_\kappa = \frac{1}{1-\psi}(\kappa_s - \kappa_1)$ is a function of the solvent compressibility κ_1.

Note that in Eq. (2.7), κ_s is not the compressibility of the solid material, but the mean compressibility of the saturated porous particles, which is a function of κ_1 as well. To calculate $\kappa_s(\kappa_1)$, we use Gassmann's equation [82–84]

$$\kappa_s(\kappa_1) = \kappa_0 + \left(\frac{1}{\kappa_d - \kappa_0} + \frac{1}{\psi} \frac{1}{\kappa_1 - \kappa_0} \right)^{-1}, \qquad (2.8)$$

where κ_0 is the compressibility of the solid material by itself, κ_d is the compressibility of the dry particles including all the pores, and ψ is the porosity.[3] Thus the complete expression for the slope S_κ is

$$S_\kappa = \frac{1}{1-\psi} \left[\kappa_0 - \kappa_1 + \left(\frac{1}{\kappa_d - \kappa_0} + \frac{1}{\psi} \frac{1}{\kappa_1 - \kappa_0} \right)^{-1} \right]. \qquad (2.9)$$

When particles are non-porous, we have $\psi = 0$, $\kappa_0 = \kappa_d = \kappa_s$, and thus $S_\kappa = \kappa_0 - \kappa_1$. This means S_κ is a linear function of κ_1 with a slope of -1. If the particles are porous but have a much smaller compressibility than the liquid ($\kappa_0 \ll \kappa_1$ and $\kappa_d \ll \kappa_1$), then $S_\kappa \to \frac{1}{1-\psi}(\kappa_d - \kappa_1)$. In this "soft liquid" limit, the slope of the S_κ-κ_1 curve approaches $-1/(1-\psi)$ as $\kappa_d/\kappa_1 \to 0$. In the regime where κ_1 is comparable to κ_0, the function $S_\kappa(\kappa_1)$ deviates from the straight line $\frac{1}{1-\psi}(\kappa_d - \kappa_1)$ and approaches $\kappa_0 - \kappa_1$. This means that we can measure the speed of sound in cornstarch suspensions comprised of different solvents (therefore different κ_1), fit the S_κ-κ_1 data with Eq. (2.9), and obtain the parameters ψ, κ_0, and κ_d. Here we assume ψ, κ_0, and κ_d do not vary when the particles are submerged in different solvents.

To find the porosity and compressibility of cornstarch particles experimentally, we measured the speed of sound c in dilute suspensions with various solvents. For each suspension, we measured the masses of the cornstarch m_{cs} and the solvent m_1, then calculated ϕ_M with Eq. (B.1) and $\bar{\rho}$ with Eq. (B.2). We performed experiments with both density-matched and non-density-matched suspensions. The effective density ρ_{eff} of a non-density-matched suspension was calculated using Eq. (A.2) [87].

---

[3]Gassmann's equation applies in the "low frequency limit," which means that the time for the pore pressure to equilibrate is sufficiently long [85, 86]. Though the central frequency of our ultrasound signal was 5 MHz, which is not normally considered a "low frequency" wave, we could still use this equation reasonably, because the cornstarch particles are small ($\sim 10\,\mu$m) and permeable, thus the time it takes for the Biot wave to diffuse through the whole particle is sufficiently short.
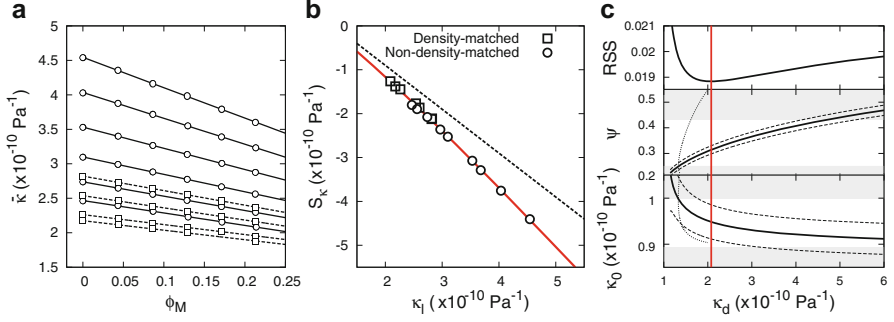
Fig. 2.3 Measuring the porosity and compressibility of microparticles in liquids using the speed of sound. (**a**) Linear relations between the mean compressibility $\bar{\kappa} = 1/(c^2 \rho_{\mathrm{eff}})$ and the material volume fraction ϕ_M for cornstarch suspensions in different aqueous solvents. Solid and dashed lines are the best fits of non-density-matched (circles) and density-matched (squares) samples, respectively. (**b**) Slopes S_κ of the lines in (**a**) as functions of κ_l. The solid red line shows the best fit using Eq. (2.9). The black dashed line shows slope -1. (**c**) Uncertainty of the fitting parameters κ_d, κ_0, and ψ. RSS is the residual sum of squares. The solid red line goes through its minimum at $\kappa_d = 2.08 \times 10^{-10}$ Pa^{-1}. In the lower two panels the solid black lines show the best fits, and the dashed black lines label the region of 95% confidence. The dotted black lines show the boundaries based on Eq. (2.10). The white central areas bound by the horizontal gray regions indicate the range of ψ or κ_0 plus or minus one standard deviation

As shown in Fig. 2.3a, for both density-matched (squares) and non-density-matched (circles) suspensions, the mean compressibility of a suspension $\bar{\kappa} = 1/(c^2 \rho_{\mathrm{eff}})$ was indeed a linear function of ϕ_M as Eq. (2.7) predicts. The solvents in the non-density-matched suspensions were mixtures of glycerol and deionized water at different mass ratios. In Fig. 2.3a, from top to bottom, the mass ratio of glycerol was 0, 15, 30, 45, 60, and 75%. For density-matched suspensions, we added an appropriate amount of CsCl into each glycerol water mixture, so that its density was 1.63×10^3 kg/m^3. In Fig. 2.3a, from top to bottom, the mass ratio of glycerol (over the sum of glycerol and water) was 0, 25, 50, and 60%. From linear regression, we obtained the slopes of these lines S_κ.

The relation between S_κ and κ_l is shown in Fig. 2.3b. We fit the data with Eq. (2.9) and obtain, $\psi = 0.31 \pm 0.12$, $\kappa_0 = (0.95 \pm 0.06) \times 10^{-10}$ Pa^{-1}, and $\kappa_d = (2.1 \pm 1.7) \times 10^{-10}$ Pa^{-1}, where ψ, κ_0, and κ_d are independent fitting parameters. In reality, however, they are not three independent variables, which allows us to narrow down the range of the parameters. Now we vary κ_d from 1×10^{-10} Pa^{-1} to 6×10^{-10} Pa^{-1}. For each κ_d, we fit the data in Fig. 2.3b with the other two parameters ψ and κ_0. From the residual sum of squares (RSS) we find that the best fit is obtained at $\kappa_d = 2.1 \times 10^{-10}$ Pa^{-1}. For a dry, porous material, its compressibility increases with porosity [88, 89], thus κ_d satisfies

$$\kappa_d > \frac{1}{1 - \psi} \kappa_0. \tag{2.10}$$

This boundary is plotted with dotted lines in Fig. 2.3c. Possible values of κ_d lie on the right-hand side of these dotted lines. Therefore, the lower limit of ψ becomes 0.25, and the upper limit of κ_0 becomes 1.0×10^{-10} Pa^{-1}. We get $\psi = 0.31^{+0.12}_{-0.06}$, $\kappa_0 = 0.95^{+0.05}_{-0.06} \times 10^{-10}$ Pa^{-1}, and $\kappa_d = 2.1^{+1.7}_{-0.8} \times 10^{-10}$ Pa^{-1}.

With the compressibility of the dry granules κ_d measured in other experiments, the uncertainty associated with these parameters can be further reduced. Waitukaitis [90] extracted the Young's modulus E_{cs} of dry cornstarch granules from indentation tests with atomic force microscopy (AFM), and found $E_{cs} \approx 5$ GPa. The Poisson's ratio of dry cornstarch particles ν_d is not well known, but for most polymers, the Poisson's ratio is higher than 0.25 [91]. Assuming $\nu_d > 0.25$, we can use the relation $\kappa_d = 3(1 - 2\nu_d)/E_{cs}$ to obtain $\kappa_d < 3.0 \times 10^{-10}$ Pa^{-1}. This leads to $\kappa_d = 2.1^{+0.9}_{-0.8} \times 10^{-10}$ Pa^{-1} and $\psi = 0.31^{+0.06}_{-0.06}$.

2.5 Ultrasound Imaging

One of the most powerful functions of ultrasound is imaging the interior of optically opaque materials. Essentially, what the ultrasound system measures is the time of flight of the sound wave. The reconstruction process of B-mode images is translating the time information to position information. A schematic illustration of one data acquisition event is shown in Fig. 2.4. A plane wave of the signal shown in Fig. 2.1c is transmitted by the transducer and propagates along the z direction. When the plane wave interacts with a scatterer, it will be reflected, but the echo back to the transducer has a curved wavefront. By comparing the phase difference of the
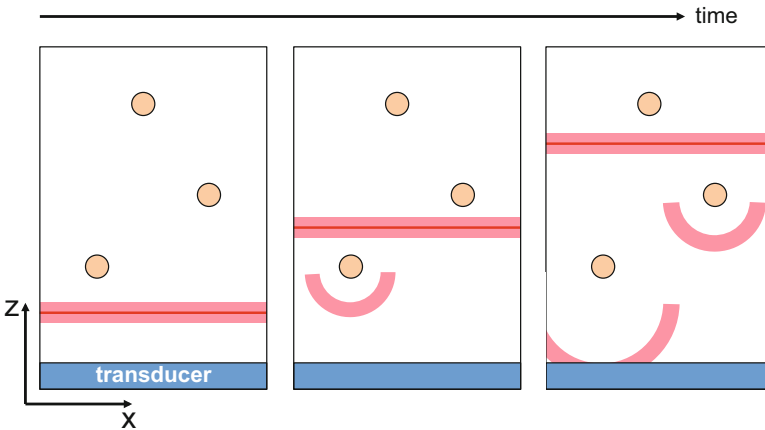

Fig. 2.4 Illustration of how ultrasound reflects back from scatterers. The scatterers are represented by the orange disks, the head of the transducer is the blue rectangle, and the ultrasound wave pulses are represented by the red bands

detected signals between adjacent piezoelectric elements, we can find the x position of the scatter. By measuring the time of flight, we can find the z position of the scatterer given the speed of sound in the surrounding medium. As a result, to reconstruct images correctly, firstly we need to measure the speed of sound in the tested material as introduced in Sect. 2.3.

With the ability to measure the positions of scatterers, ultrasound allows us to track the motion of the material in which the scatters are embedded by applying particle image velocimetry (PIV) to the reconstructed images. To check the reliability of this method, we measured the velocity field in a gelatin block with embedded particles under simple shear. As illustrated in Fig. 2.5a, the gelatin sample was a cuboid made of 10% (w/w) gelatin in water, with a layer of glass spheres uniformly distributed in the middle of the sample. The experimental setup is sketched in Fig. 2.5b. The gelatin block was placed vertically (meaning the particle layer was vertical) on a 5/64 inch thick acrylic board and sheared by a plane that slid horizontally on the top. An L12-5 (50 mm wide) transducer ($f = f_c = 8.93$ MHz) was placed below the acrylic board, and the imaging plane (x–z plane in Fig. 2.1b) was aligned with the layer of particles in the sample. Since gelatin is optically transparent, we observed the motion of the particles simultaneously with a high-speed camera (Phantom V9), at a spatial resolution of 65.6 μm/pixel. In this way, the ultrasound images could be directly compared with the optical images.

We tried spherical scatterers with two different diameters: $d = 300$–$400\,\mu$m ($\approx 2\lambda$) and $d = 45$–$63\,\mu$m ($\approx 0.3\lambda$), where $\lambda \approx 0.17$ mm was the wavelength. The spatial resolution of the reconstructed images is limited by the wavelength—only objects with a length scale greater than λ can be resolved. As shown in Fig. 2.5c, d, the positions of individual particles were captured in the ultrasound images when $d \approx 2\lambda$, but we can only see a speckle pattern that does not have a one-to-one correspondence with the real particle positions when $d \approx 0.3\lambda$. However, in both cases, the motion of the speckle pattern represented the motion of the materials.

To test the correlation between the speckle motion and the material motion, we moved the sliding surface back and forth horizontally by hand and took consecutive images with the camera and the ultrasound simultaneously. We performed PIV analysis with both optical and ultrasound images. Each image was divided into square elements, and the velocity of each element was calculated through a cross-correlation algorithm between two subsequent frames. As expected for an elastic solid, the local horizontal velocities increased linearly with the height, and the two independent measurements showed excellent agreement, for both large and small scatters. An exemplary result is shown in Fig. 2.5e, which compares horizontal velocities as a function of time measured by the two methods at a certain height of the sample with $d \approx 0.3\lambda$ spheres. Since the sample was randomly sheared by hand, there were many fine features in its motion. Nevertheless, the ultrasound measurements captured all the details in the changing velocity.
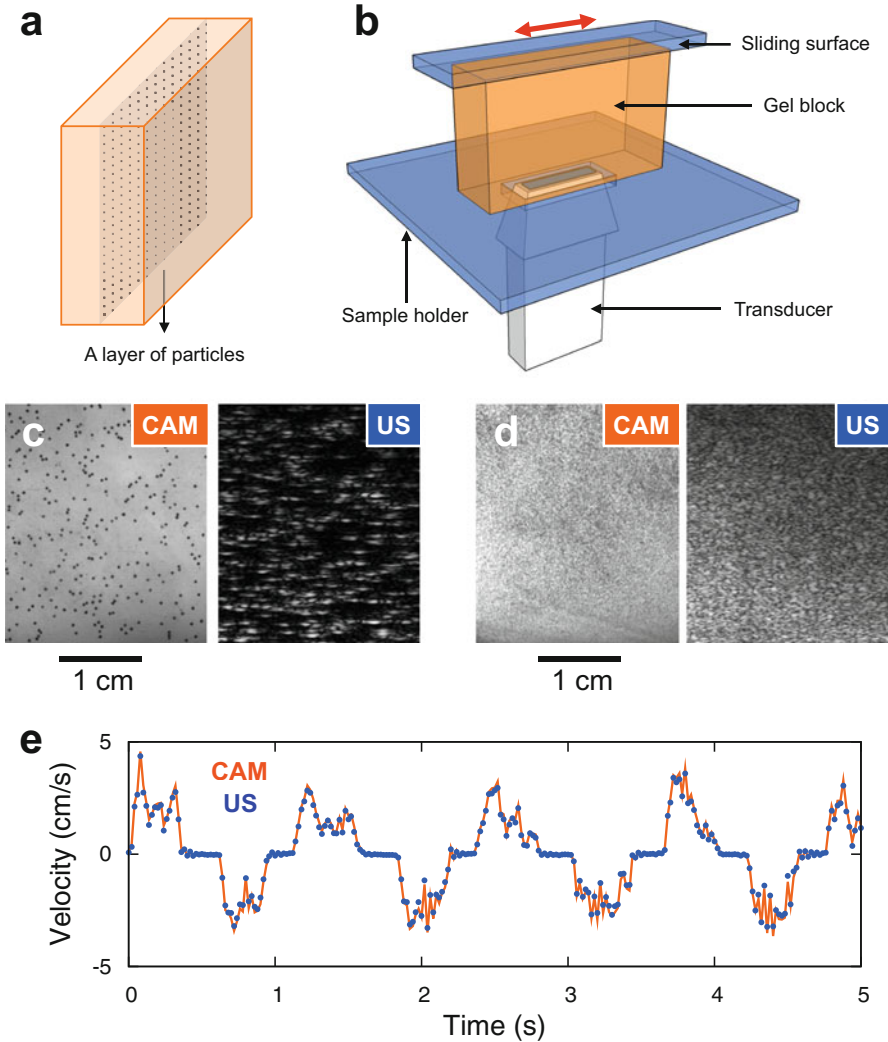
Fig. 2.5 (**a**) Gelatin block with a layer of embedded glass particles. (**b**) Experimental setup. The slider on the top moves horizontally. (**c**) Comparison between a camera (CAM) image and an ultrasound B-mode image (US) for 300–400 μm (≈ 2λ) particles. (**d**) Comparison for 45–63 μm (≈ 0.3λ) particles. (**e**) Horizontal velocity as a function of time obtained from the camera (orange) and the ultrasound (blue) at the same height, for the sample in (**d**)

2.6 Visualizing Flows of Dense Suspensions

When sound waves propagate from one medium into another, reflections happen at the interface. The intensity reflection coefficient R_I is defined as the ratio between the intensity magnitudes of the reflected wave and the incident wave. For normal

Table 2.1 Speed of sound c, density ρ, and acoustic impedance Z in some materials at room temperature ($20\,°C$)

Material	c (m s^{-1})	ρ (kg m^{-3})	Z (kg m^{-2} s^{-1})
Air	340	1.20	408
Water	1480	1000	1.48×10^6
Density-matched solvent	1647	1630	2.68×10^6
Cornstarch suspension	1939	1630	3.16×10^6
VoroWhite plastics	2412	1210	2.92×10^6
Acrylic	2744	1180	3.24×10^6

The density-matched solvent was a mixture of 44.3% CsCl, 27.8% glycerol, and 27.8% water by mass. The Cornstarch suspension was prepared with the solvent above at packing fraction $\phi = 0.48$

incidence, we have

$$R_I = \left(\frac{Z_2 - Z_1}{Z_2 + Z_1} \right)^2, \tag{2.11}$$

where $Z = \rho c$ is the acoustic impedance, and 1, 2 represent the media on each side of the interface. The corresponding intensity transmission coefficient for normal incidence is $T_I = 1 - R_I$. The acoustic impedance of some materials is listed in Table 2.1.

As Table 2.1 shows, air has a very different impedance compared to water or cornstarch suspensions. As a result, when there are air bubbles in the suspensions, we receive strongly scattered signals. After preparing a dense cornstarch suspension, we immediately transferred it into a 10 ml syringe, sealed the nozzle, and observed with ultrasound by pushing the transducer against the wall of the syringe. The B-mode image obtained is shown in Fig. 2.6a. We saw very strong signals close to the transducer, and the sound wave did not penetrate deeply. We then left the suspension rest for 30 min, and observed with ultrasound again, as shown in Fig. 2.6b. Now the system became more transparent, and we can see the wall of the syringe on the opposite side, but there was still strong scattering in the suspension. Lastly, we debubbled the suspension by pulling the plunger of the syringe to create a low pressure inside. The size of the bubbles expanded, and by tapping the syringe, we got rid of most of the bubbles visible by the ultrasound as shown in Fig. 2.6c. A strong reflection is seen from the opposite wall. We average the corresponding RF data of the three images along the x direction, and plot the averaged signal amplitudes as functions of the depth z in Fig. 2.6c. From the plot, we can see dramatically reduced scatterings, and a much stronger transmission signal reflected from the opposite wall at $z \approx 13$ mm.

A similar effect can be obtained by pressurizing the suspension. We kept the syringe sealed, and pushed its plunger with an Instron material tester. The results are plotted in Fig. 2.6e, which can be directly compared to (d). Again, we can see that the amplitude of the signals in the sample decreased when the applied
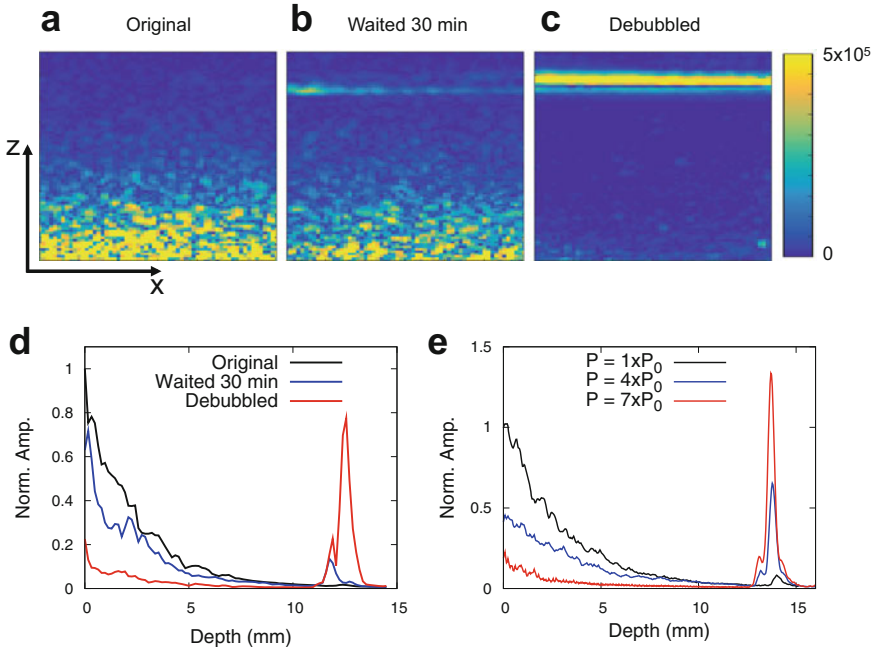
Fig. 2.6 Effect of air bubbles in ultrasound imaging of dense suspensions. (**a**–**c**) Ultrasound B-mode images of dense cornstarch suspensions in a 10 ml syringe. The transducer is at the bottom of these images. (**d**) Amplitude of RF signals in suspensions with different air concentrations. (**e**) Amplitude of RF signals in suspensions under different pressure

pressure increased from P_0 to $7 \times P_0$ (P_0 is the atmospheric pressure). The amplitude of the signal reflected from the opposite wall increased with pressure, which confirmed that the decrease of brightness in the bulk was not due to increased energy dissipation (attenuation), but less scattering. We think this phenomenon is caused by the decrease in bubble sizes, which leads to smaller scattering cross-sections, at high pressure. Potentially, this method could be used to detect pressure in the suspensions, but much more careful calibration is required.

To track the motion of the suspensions, we need an appropriate speckle density in the B-mode images. A freshly made dense suspension normally has too many bubbles in it, as shown in Fig. 2.7c. In this case, the penetration depth of the signal is highly limited, and when the suspension moves, the speckles show significant deformation besides translations, which makes the tracking more difficult. Thus for ultrasound imaging, we debubbled a suspension first, so that it became almost acoustically transparent and featureless as shown in Fig. 2.7a. Then we added a certain amount of air bubbles back to the suspension by slowly stirring with a spatula. Figure 2.7b shows an example of the speckle concentration and contrast that worked well in practice. The speckle pattern in a flowing suspension is demonstrated in Fig. 2.7d. In this kymograph, vertical slices taken at the same position from a
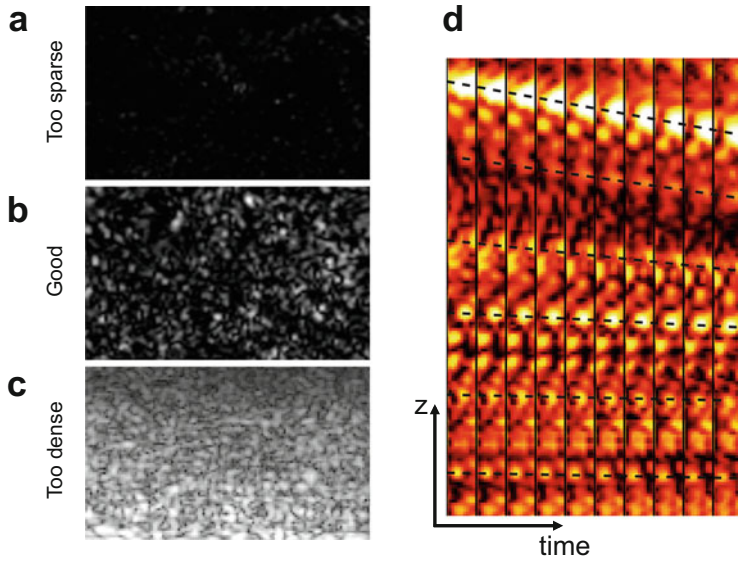
Fig. 2.7 Speckle patterns in dense suspensions for tracking. (**a–c**) Speckle patterns generated by different air bubble concentrations in dense suspensions: (**a**) too few scatterers; (**b**) good speckle pattern; (**c**) too many scatterers. (**d**) Exemplary kymograph. Each column segregated by the thin black lines is obtained from the same x position in a series of B-mode images

series of B-mode images are stitched next to each other. The speckles moved with the flow in the vertical direction, as labeled by the dashed black lines. The slope of each line represents the local vertical velocity of the suspension, which agrees with the results obtained from the PIV analysis.

Lastly, we checked the effect of air bubbles on the mechanical properties of dense suspensions with steady-state rheology experiments. When the suspension was just made (corresponding ultrasound image is shown in Fig. 2.6a), it had higher viscosity at low shear stress compared to the debubbled suspension, which led to stronger shear thinning. At shear stress above 1 Pa, there was no difference between the two samples according to the rheology measurements. For a non-debubbled sample that was tested 30 min after preparation, there was still a significant amount of air bubbles in the suspension as shown in Fig. 2.6b, but its rheological properties were identical to a fully debubbled suspension across the whole stress range tested. Thus we conclude that adding a limited number of small air bubbles as tracers does not change the mechanical properties of the suspensions that we are interested in here.

Chapter 3
Investigating Impact-Activated Fronts with Ultrasound

3.1 Introduction

In this chapter, we will reveal the mechanism of impact-activated solidification by applying the ultrasound techniques described in Chap. 2 to a series of impact rheology experiments. As introduced in Sect. 1.4, impact on the surface of a dense suspension can generate a front that propagates across the system faster than the impactor itself [54]. This front transforms the suspension from a fluid-like state into a solid-like state. Initially, a model [60] based on jamming by compression and thus densification [26] was proposed to explain this dynamic jamming transition. Although the model well captures the major features of the phenomenon, it has certain limitations, which we will briefly revisit here.

While preparing suspensions, we can match the density of the interstitial liquid to the density of the particles. Density matching makes it possible to prepare a three-dimensional granular material at packing fractions ϕ well below ϕ_J. Consequently, jamming by densification implies significant change in ϕ: $\Delta\phi = \phi_J - \phi$, given that such systems still exhibit impact-induced solidification. However, unless the impact speed U_p is so fast that the liquid becomes compressible [93], densification of the particle sub-phase during a short time is counteracted by the hydrodynamic interactions. Therefore the mechanism underlying Eq. (1.6) becomes questionable, even though its primary outcome agrees with experimental measurements, which shows that the ratio between the front speed and the impact speed increases dramatically as $\Delta\phi$ approaches zero [54, 59].

One recently emerged alternative mechanism is the concept of jamming by shear [27, 43]. As an extension of frictionless, standard jamming, it proposes that the presence of frictional interactions between particles enables the system under shear to start from an isotropic, unjammed initial configuration at $\phi < \phi_J$, and rearrange

---

E. Han, *Transient Dynamics of Concentrated Particulate Suspensions Under Shear*, Springer Theses, https://doi.org/10.1007/978-3-030-38348-0_3

the particles into anisotropic fragile or jammed configurations without changing ϕ. Shear jamming is also observed in frictionless systems, albeit over a much narrower range in $\Delta\phi$ [29]. So far, shear jamming has been studied experimentally in two-dimensional (2D) dry granular systems under quasi-static conditions [27]. Investigating the role of shear jamming in impact-induced dynamic solidification of dense suspensions in 3D requires non-invasive, high-speed imaging of the jamming fronts and the associated, quickly evolving flow field in the interior of an optically opaque system.

Ultrasound satisfies all these requirements. Related techniques have been applied to studying dry granular materials [65, 66] and steady-state flows in suspensions [63, 64, 94–96]. As the suspension jams, we obtained an upper bound on the change of packing fraction $\Delta\phi$ by measuring the speed of sound c. We found that in the regime of $U_\mathrm{p} \ll c$, $\Delta\phi$ was significantly below the value required if impact-activated solidification was primarily driven by densification. In the regime of slow U_p, the suspension behaved like a viscous fluid. In the regime of fast U_p, it shear thickened dramatically and developed solid-like characteristics, which we identified by investigating the flow fields using high-speed ultrasound. We observed the emergence of concentrated shear bands at the location of the propagating jamming fronts. The invariant packing fraction and the existence of shear bands provide direct evidence of dynamic shear jamming in three-dimensional suspensions. Furthermore, the ability to map out the full flow field allowed us to extract the local shear rates and identify the origin of a key, but so far unexplained, feature of the jamming fronts: their longitudinal propagation speed exceeds the transverse propagation speed, and the ratio was close to two [59].

3.2   Impact Experiment with Ultrasound

Our experimental setup is illustrated in Fig. 3.1. The ultrasound imaging and speed of sound measurements were performed with a Verasonics Vantage 128 system. We used a prototypical suspension: cornstarch particles dispersed in water–glycerol–cesium chloride (CsCl) solutions. To increase the amount of sound energy transmitted into the suspensions, we made the sample container with materials that closely matched the acoustic impedance of the suspensions. According to Table 2.1, we could use either "VeroWhitePlus" plastic, which is a UV-cured resin, or acrylic. Here the sample container was 3D-printed with VeroWhitePlus (Objet Geometries Inc.). The inner diameter of the container was 10.0 cm and the typical depth H of the suspension was 2.5–3.5 cm. This diameter-depth ratio ensured that the front reached the bottom before it interacted with the sidewall. The impactor was a cylinder with a flat head, and its diameter was 6 or 10 mm. It was driven by a computer-controlled linear actuator (SCN5, Dyadic Systems) and equipped with a force sensor (DLC101, Omega). The ultrasound transducer (Philips L7-4) had 128 independent elements, and its total width was 3.8 cm. The head of the transducer contacted the bottom of the container through a thin layer of ultrasound gel.
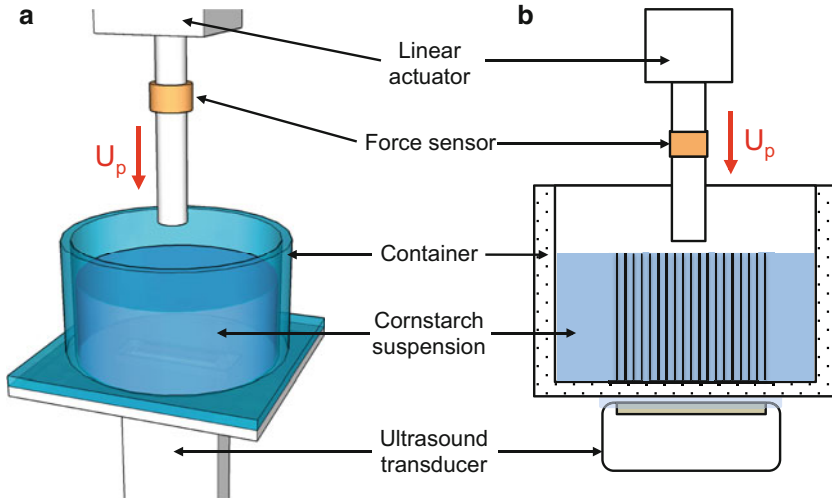
Fig. 3.1 Schematic of the experimental setup. (**a**) shows a 3D sketch of the setup, and (**b**) shows the 2D cross-section. The sample container and impactor are both cylindrical and concentric. The ultrasound transducer scans a vertical slice along the central axis (z axis), providing a field of view as indicated by the striped area

In an impact experiment, the impactor moved downward vertically with a constant speed U_p. The ultrasound system was triggered when the impactor reached a certain distance above the suspension surface. Once triggered, it made several hundred acquisitions consecutively. The images were taken at a rate of 10–10,000 frames per second, adjusted based on U_p. In one acquisition, all the transducer elements transmitted the same ultrasonic pulse at the same time, and each element received an individual time series of the reflected signal. Each pulse was a 5 MHz sinusoidal wave modulated by a Gaussian profile, and the length of one pulse was six periods. From the time series received by all the elements and using the previously measured speed of sound c, we reconstructed B-mode images [69] that captured speckle patterns that reflect the positions of the tracer particles (air bubbles) in the suspension. The spatial resolution in our experiments was about 0.4 mm, limited by the wavelength of the ultrasound. By tracking the motion of the speckle patterns with a particle imaging velocimetry (PIV) algorithm, we obtained a 2D flow field from within the bulk of the suspension. We verified that a proper amount of bubbles did not suppress the penetration of the ultrasound in the suspensions, and their effect on the speed of sound was negligible. We also determined that the suspension viscosity was barely affected by the embedded bubbles (see Sect. 2.6). Between successive impact experiments, the suspension was relaxed by gently shaking and rotating the container.

3.3 Measurement of Flow Field

A representative flow field (u_r, u_z) inside the suspension during an impact is shown in Fig. 3.2a–c. The horizontal and vertical axes in the image correspond to the r and z directions in the cylindrical coordinates, and the z axis overlaps with the central line of the impactor. The flow field shows a solid-like (or highly viscous) plug under the impactor, as evidenced by the fact that every point moves vertically with a velocity close to U_p. Also evident is a strong velocity gradient around the
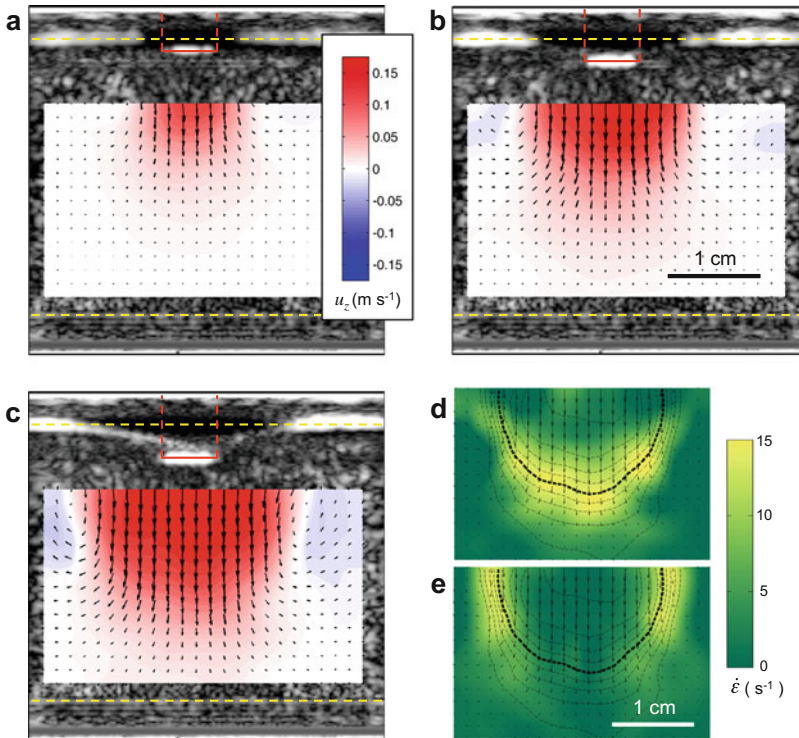
Fig. 3.2 Visualization of the flow field with ultrasound. (**a**)–(**c**) Velocity field during an impact at time 6.0 ms (**a**), 13.2 ms (**b**), and 20.3 ms (**c**) (the impactor reached the surface at time $t = 0$ ms). The images are B-mode images (shown in gray scale) with overlaid velocity field from PIV analysis. The color code represents the magnitude and sign of the vertical component of the local velocity u_z (red corresponds to downward, blue to upward flow). Dashed yellow lines indicate the locations of the free surface of the suspension and of the bottom of the container. The impactor is outlined in red. The experimental parameters were $\phi = 0.47$, $U_p = 175$ mm·s^{-1}, liquid viscosity $\eta_0 = 4.6 \pm 0.2$ mPa·s, fill depth $H = 30$ mm, and impactor diameter of 6.0 mm. The black scale bar in (**b**) represents 1 cm for (**a**)–(**c**). (**d, e**) Two components of the shear rate tensor, $|\dot{\varepsilon}_{zz}|$ (**d**) and $|\dot{\varepsilon}_{rz}|$ (**e**), shown for the same instant in time as the flow field in (**c**). Dashed lines are contours connecting points with the same u_z. The thicker line indicates $u_z = U_p/2$. The white scale bar is 1 cm for (**d**) and (**e**)

periphery of the solid-like region. To show this more explicitly, we calculate the local shear rate tensor $\dot{\boldsymbol{\varepsilon}}$ from the velocity field (u_r, u_z). Given rotational symmetry, it can be written as

$$
\dot{\boldsymbol{\varepsilon}} = \begin{bmatrix}
\frac{\partial u_r}{\partial r} & 0 & \frac{1}{2}\left(\frac{\partial u_r}{\partial z} + \frac{\partial u_z}{\partial r}\right) \\
0 & \frac{u_r}{r} & 0 \\
\frac{1}{2}\left(\frac{\partial u_r}{\partial z} + \frac{\partial u_z}{\partial r}\right) & 0 & \frac{\partial u_z}{\partial z}
\end{bmatrix}. \tag{3.1}
$$

Figure 3.2d, e show two important components in $\dot{\boldsymbol{\varepsilon}}$: $|\dot{\varepsilon}_{zz}| = -\frac{\partial u_z}{\partial z}$ and $|\dot{\varepsilon}_{rz}| = -\frac{1}{2}\left(\frac{\partial u_r}{\partial z} + \frac{\partial u_z}{\partial r}\right)$. Underneath the solid-like region, i.e., in the longitudinal direction, the diagonal terms dominate. This corresponds to a uniaxial compression (or pure shear in 2D) that compresses the suspension in the z direction and allows it to expand radially. By contrast, along the sides of the solid-like plug, the non-diagonal term $\dot{\varepsilon}_{rz}$ dominates, and within it, the main contribution arises from $\frac{\partial u_z}{\partial r}$. In other words, the gradient of the velocity is perpendicular to U_p in the transverse direction. This is analogous to the simple shear as seen, for example, in parallel plate setups. In Sect. 3.5, we will revisit this point and reveal the significant implications of having both types of shear.

3.4 Invariant Packing Fraction During Front Propagation

The shear modulus vanishes in an unjammed suspension of solid particles in a Newtonian liquid. In the limit where the wavelength is much longer than the size of the solid particles, the speed of sound is $c = (K/\rho)^{\frac{1}{2}}$, where K is the average bulk modulus and ρ the average density of the suspension [72, 97]. In our experiments, the particles and suspending liquid were density matched, but the average K still increases with ϕ since cornstarch particles have a larger bulk modulus than the liquid (see Sect. 2.4). As shown in Fig. 3.3a, the resulting dependence of c on ϕ is, to a good approximation, linear across the regime of ϕ in which an impact can jam the suspension dynamically. This allows us to find any variation in packing fraction $\Delta\phi = \phi_f - \phi_0$ straightforwardly by detecting changes in c with ultrasound, where ϕ_f is the packing fraction in the solid-like region, and ϕ_0 is the initial packing fraction of the quiescent suspension.

The experimental setup has been shown in Fig. 3.1. Initially, the head of the impactor just touched the surface of the suspension, and then it pushed down a distance z_p. The position of the impactor was measured with a high-speed camera (Phantom V9, Vision Research). At the same time, we used ultrasound to measure the time of flight T of the signal from when it left the transducer to when it returned after being reflected by the impactor. The average speed of sound $\bar{c}$ along this path is

$$
\bar{c} = 2\frac{H - z_p}{T}, \tag{3.2}
$$
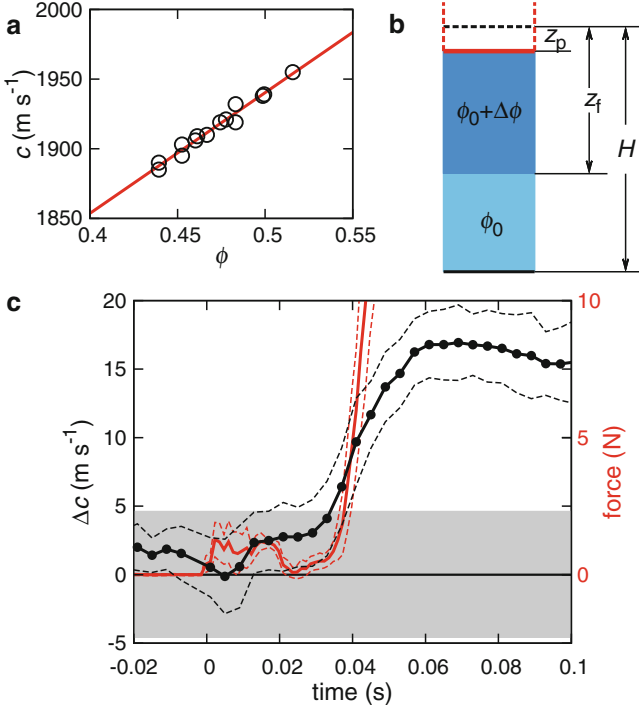
Fig. 3.3 Direct measurement of packing fraction variations. (**a**) Speed of sound c as a function of packing fraction ϕ. All data were taken with suspensions in their quiescent fluid-like state, at ϕ well below ϕ_J. (**b**) Sketch of the region beneath the impactor. The black dashed line represents the initial suspension surface at a fill height H above the bottom of the container (bold black solid line). As the impactor (outlined in red) pushes down a vertical distance z_p the front (dark blue region) propagates a distance z_f. (**c**) Change in sound speed Δc as a function of time (black trace) at $\phi_0 = 0.48$. Impact at the free suspension surface occurs at $t = 0$ ms. Once the front has reached the bottom of the container (at $t \approx 35$ ms), the force on the impactor (red trace) rises dramatically. Note that within our experimental uncertainties, the speed of sound does not increase until the shear-jammed region becomes compressed. Data are averages from seven experiments that simultaneously measured force and sound speed as functions of time. Dashed lines indicate one standard deviation. The gray region shows the uncertainty (given by one standard deviation) in determining Δc at low U_p, where no solidification takes place

where H is the original depth of the suspension.

As a calibration, we firstly performed a low speed experiment at $U_p = 5$ mm·s^{-1} to measure the speed of sound in the unjammed, fluid-like suspension, where $\bar{c} = c(\phi_0)$. Defining T_0 as the round-trip time of flight when $z_p = 0$ mm, we have $H = c(\phi_0)T_0/2$. Since $c(\phi_0)$ is supposed to be invariant during the whole process, plug the expression for H into Eq. (3.2), we find

$$c(\phi_0) = \frac{2z_p}{T_0 - T}. \tag{3.3}$$

The initial packing fraction ϕ_0 of the suspension here was 0.48. The solvent was a mixture of 44.3% CsCl, 27.8% glycerol, and 27.8% water by mass. Its viscosity was $\eta_0 = 4.6$ mPa·s and its density was $\rho = 1.63 \times 10^3$ kg·m^{-3}. From six measurements we obtain $c(\phi_0) = 1939.2 \pm 4.6$ m·s^{-1} and $H = c(\phi_0)T_0/2 = 34.1 \pm 0.1$ mm.

At a fast speed $U_p = 200$ mm·s^{-1}, a front was generated as illustrated in Fig. 3.3b. The sketch indicates two regions: the solid-like region (dark blue) directly underneath the impactor and an unjammed region (light blue) ahead of the front. Here we use the value of H measured above and Eq. (3.2) to calculate $\bar{c}$. The time of flight now becomes

$$T = 2\left[\frac{H - z_f}{c(\phi_0)} + \frac{z_f - z_p}{c(\phi_0 + \Delta\phi)}\right]. \tag{3.4}$$

For $\Delta\phi = 0$, $T_{\Delta\phi=0} = 2(H - z_p)/c(\phi_0)$. If $\Delta\phi > 0$, there will be a difference between T and $T_{\Delta\phi=0}$, and this difference becomes increasingly more significant as z_f increases, which leads to an increase in $\bar{c}$ according to Eq. (3.2).

Note that when a suspension transforms from an unjammed state to a jammed state, an increase in ϕ may not be the only cause for a faster speed of sound. There are two other possible mechanisms: (1) an increase in effective bulk modulus K; (2) the development of a finite shear modulus G [26]. By measuring the speed of sound alone, we cannot determine how much these three mechanisms each contribute, but we can estimate the upper limit of each term assuming the other two zero.

Firstly, we estimate the maximum possible increase in ϕ. Figure 3.3c presents the experimentally measured $\Delta c = \bar{c} - c(\phi_0)$ when a suspension with $\phi_0 = 0.48$ was under impact. The impactor head started moving at time $t = 0$ s from the suspension surface and generated a front that reached the bottom of the container at $t \approx 0.035$ s. We identify this point because the force applied on the impactor increased dramatic, which is well established by prior work with quasi-2D [59] and 3D [54] systems. Before the front interacted with the bottom, $\Delta c = \bar{c} - c(\phi_0)$ kept below the noise floor of this measurement, which was about 5 m/s. Neglecting any increases in K and G due to jamming, we find that $\Delta c \approx 5$ m/s implies $\Delta\phi \approx 0.006$ from Fig. 3.3a. Therefore, ϕ could have increased to 0.49 at best. Furthermore, even at the maximum packing fraction $\phi = 0.52$ in Fig. 3.3a, the suspension still flowed when sheared slowly, which means that the isotropic jamming threshold ϕ_J must exceed 0.52. As a result, the actual increase in ϕ due to impact is much less than what the densification model (Eq. 1.6) requires.

If instead we assume $\Delta\phi = 0$ and use $c = \left[\left(K + \frac{4}{3}G\right)/\rho\right]^{\frac{1}{2}}$, which considers the non-zero shear modulus of the jammed solid [69], to describe the dependence of the speed of sound on K and G within the jammed region behind the front, the same noise floor $\Delta c \approx 5$ m/s implies that the net increase in the sum of the moduli $\tilde{K} = K + \frac{4}{3}G$ could not have exceeded $\Delta\tilde{K} \approx 32$ MPa. This is very small compared to the bulk modulus K_0 of the quiescent suspension at $\phi_0 = 0.48$: $\Delta\tilde{K}/K_0 \approx 0.5\%$.

In the regime where the front had reached the bottom and was compressed even more, we found $\Delta c \approx 16$ m·s^{-1}. While this is significantly above the noise floor,

the packing fraction did not increase more than $\Delta\phi \approx 0.02$, still less than necessary to reach ϕ_J. Nevertheless, the existence of the solid boundary significantly increases the stress in the dynamically jammed region, which should drive the suspension deeper into the shear-jammed state. We can, therefore, expect concomitant increases in bulk and shear moduli and thus in the speed of sound. From Fig. 3.3, the upper limit of the net increase in the sum of the moduli $\tilde{K}$ is $\Delta\tilde{K} \approx 101$ MPa in this regime.

3.5 Impact-Activated Fronts Are Shear Fronts

The flow fields in Fig. 3.2 allow us to extract the position of the propagating jamming front. We define the front position as the line of points where the vertical component of the local velocity u_z drops to $U_p/2$. In particular, we focus on the furthest reaching points in the flow field along the z and r directions, i.e., on the maximum longitudinal and transverse front speeds. As Fig. 3.4a shows, after an initial stage of faster growth, the front in both directions propagate essentially at constant speeds (positions as linear functions of time) before slowing down when it starts to interact with solid boundaries. As discussed above, when a front and a solid boundary interact, the incipient jammed region gets compressed by the impactor, and further compression quickly ceases the motion of the suspension in between. Here we investigate the linear regime, where the front propagates freely. To compare how quickly the front propagates relative to the driving speed U_p, we define the dimensionless front propagation speeds k_t and k_l as

$$k_t = \frac{U_{ft}}{U_p}, \; k_l = \frac{U_{fl}}{U_p} - 1, \tag{3.5}$$

where the subscripts t and l represent "transverse" and "longitudinal," respectively. The "-1" in k_l compensates for the vertical motion of the impactor itself.

The parameters that affect k_l and k_t include ϕ, U_p, and the suspending liquid's viscosity η_0. For a suspension with given η_0 and ϕ that is impacted very slowly, the response is fluid-like and both k_t and k_l are close to zero. However, beyond a threshold value U_{p0}, fronts start to appear. The normalized front speed initially increases quickly with U_p but eventually asymptotes to a fixed value k^*. The relation between k_l and U_p in suspensions with the same η_0 but different ϕ is shown in Fig. 3.4b; the behavior of k_t is similar. As ϕ increases the curves shift towards lower U_{p0} and higher k^*. For comparison, in suspensions with the same ϕ, larger solvent viscosity η_0 leads to lower threshold U_{p0}, but leaves k^* invariant [54]. In order to extract k^* and U_{p0} we fit the data to

$$\frac{k}{k^*} = \begin{cases} 0 & (U_p \leq U_{p0}), \\ 1 - e^{1 - U_p/U_{p0}} & (U_p > U_{p0}). \end{cases} \tag{3.6}$$
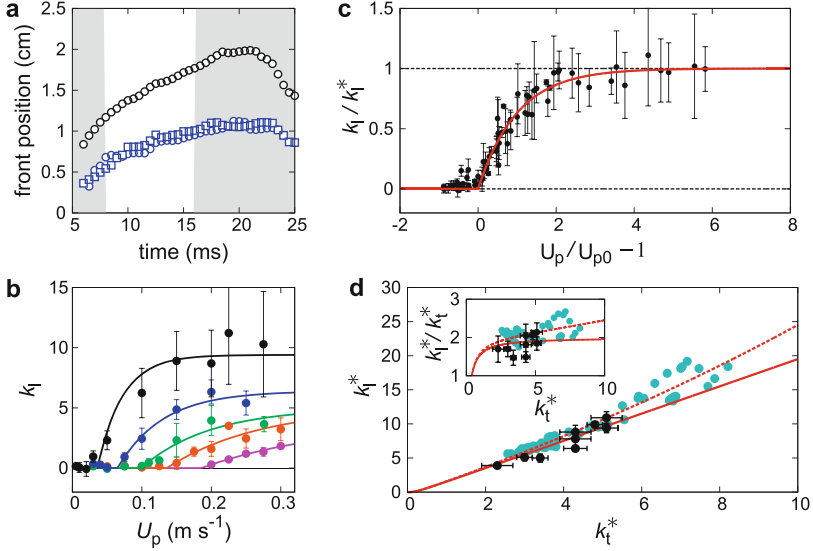
Fig. 3.4 Propagation of impact-activated fronts. (**a**) Front position in the longitudinal (black) and transverse (blue circles: right, blue squares: left) directions as functions of time. The head of the impactor reaches the suspension surface at time $t = 0$ ms. The gray regions indicate the initial front build-up stage (left) and the regime in which the front starts to interact with the bottom of the container and slows down (right). In this $U_p = 200$ mms, $\phi = 0.460$. (**b**) Dimensionless front propagation speed k_l in the longitudinal direction as a function of U_p for different ϕ (magenta: 0.439, orange: 0.453, green: 0.460, blue: 0.474, black: 0.498). All data are obtained with a suspending liquid with viscosity $\eta_0 = 4.6 \pm 0.2$ mPa·s. Error bars show the standard deviation of three measurements. (**c**) Front speed k_l/k_l^* normalized by its asymptotic value as function of impactor speed U_p normalized by threshold speed U_{p0}. Data from experiments with different ϕ and η_0 collapse onto a master curve of Eq. (3.6) (solid red line). (**d**) Relationship between the asymptotic front speeds k_l^* and k_t^*. Data from both quasi-2D [59] (turquoise) and 3D (black) impact experiments are shown. The solid red line is the prediction from Eq. (3.7). The slope approaches 2 as k_t^* increases. The dashed red line is a modified version of the model, which includes a small strain anisotropy δ, here plotted using a value of $\delta = 0.01$. Error bars are the asymptotic standard error from the fittings of each k-U_p curve with Eq. (3.6)

Equation (3.6) is a phenomenological relation that captures the key aspects of the experimental data: (1) $k = 0$ at small U_p; (2) k increases with U_p when $U_p > U_{p0}$; (3) k approaches a finite value k^* as $U_p \rightarrow \infty$. Plotting the data in terms of the normalized variables k/k^* and U_p/U_{p0} scales out the dependencies on ϕ and η_0. The resulting data collapse for the normalized front speed in the longitudinal direction k_l/k_l^* is shown in Fig. 3.4c. The transverse speed ratio k_t/k_t^* can be rescaled the same way.

The data collapse allows us to quantify the anisotropic front propagation speeds in the longitudinal and transverse directions. Combining results obtained from

experiments with various ϕ[1] and η_0, we plot k_l^* versus k_t^* in Fig. 3.4d. To a good approximation, all data follow $k_l^* \approx 2k_t^*$. In the figure we also present the data obtained with a quasi-2D suspension system [59], which show good agreement with the trend as well, except that for higher k_t the ratio k_l/k_t slightly exceeds 2.

Our data in Fig. 3.3c demonstrate that in a dense suspension prepared below the isotropic jamming point ϕ_J, impact-activated jamming can proceed without any significant increase in ϕ, and certainly, the system can jam without increasing ϕ up to ϕ_J. This result rules out an earlier model that connects the formation of such fronts with entering the jammed state via densification of the particle sub-phase [54, 60]. Moreover, analysis of the flow field reveals that the jamming fronts initiated by the impact coincide with where the local shear rate maximizes (Fig. 3.2d, e). Altogether, these two findings provide strong evidence for dynamic shear jamming: the impact triggers propagating fronts that locally create sufficient shear to reorganize particles into (anisotropic) jammed configurations without changing the average packing fraction. There are several implications of the shear jamming scenario for suspensions and several differences from dry granular systems, both of which we discuss next.

To start, we examine stress. In a dry granular system, stress is sustained only via direct contact between particles. By contrast, in a dense suspension, stress can be transmitted without contact because there are hydrodynamic interactions between the particles such as the lubrication force. As a result, while in dry granular systems there is only a single characteristic stress scale for entry into the shear-jammed regime [27], for a suspension, the situation can be more complicated. Some experiments [25, 33, 35, 50], simulations [38, 40, 41], and theoretical models [43] have recently suggested that beyond a stress threshold Σ_1, lubrication breaks down and particles start to experience frictional interactions. Thus, in the regime $\Sigma < \Sigma_1$, the suspension behaves like a viscous fluid, while at $\Sigma > \Sigma_1$, it behaves more like a frictional granular system. As Σ increases, the system firstly enters a fragile regime, and then at a higher second characteristic stress level Σ_2, crosses over into the shear-jammed regime [27, 28, 98]. Within this picture, we associate the transition at U_{p0} with the situation where the stress levels at the leading edge of the jamming front have reached Σ_1 and are large enough for frictional interactions to occur. Thus, when $U_p < U_{p0}$ the suspension is in the lubrication regime, but when $U_p > U_{p0}$ it transforms into a fragile state with behavior intermediate between solid and fluid [8, 27, 99]. As the stress increases, frictional contacts start percolating through the system to form a load-bearing network and eventually reach a shear-jammed state. We point out that a non-zero shear modulus is not strictly necessary for the front to propagate (with $k > 0$). The front will propagate as long as it transforms the initially liquid-like suspension into a state with sufficiently large viscosity. However, we know that the material solidifies while interacting with a system boundary [28, 54, 55, 59]. Thus, before a system-spanning jammed state has been established, how the shear modulus evolves behind the jamming front remains an open question.

---

[1]Both k_l^* and k_t^* increase with ϕ.

We will continue this discussion in Chaps. 4 and 5. We will exploit such jamming fronts to explore the state diagram of dense suspensions systematically, and link Σ_1 and Σ_2 to the onset stress of DST, Σ_{DST}, and of shear jamming, Σ_{SJ}.

The stress-based argument above also explains the relaxation or "melting" of the jammed region when the impact stops. During front propagation, it is the inertia of the suspension in the shear zone that sustains the stress inside the solid-like region. When the motion of the impactor stops, the shear zone disappears, and the stress applied on the boundary of the jammed suspension falls below Σ_1, insufficient to sustain frictional interactions between particles. Therefore, there is no network of force chains that can generate non-zero yield stress and support a load. As a result, the suspension returns to the lubrication regime.

However, while necessary, the existence of threshold stress levels is not sufficient to explain the asymptotic front speed k^* at high U_{p} and the seemingly universal anisotropy in front propagation, expressed by the ratio $k_1^*/k_t^* \approx 2$. Actually, particles need to move out of an initially uniform and isotropic distribution and reorganize under shear into anisotropic structures (force networks) that can support the stress. Such reorganization requires a minimum shear strain ε_c to engage neighboring particle layers. As a result, shear jamming happens only when stress and strain both reach their corresponding threshold values. In a quasi-static granular system [27, 42] the threshold strain only matters when the shear-jammed state is prepared or when the shear is reversed. In the dynamic systems considered here, the front continues to propagate into unperturbed suspension, and therefore, the front advances by applying strain ε_c locally during the whole process of front propagation.

Here we show that for dense suspensions in the high U_{p} regime, where the stress behind the front is way above the threshold, k^* is governed by ε_c and the anisotropy in front speeds is a direct consequence of the existence of one strain threshold. As described above, the suspension experiences pure shear in the longitudinal direction and simple shear in the transverse direction. In 2D, we can directly compare the two types of shear using the positive eigenvalues of the shear rate tensors, treating the propagation of the front in the longitudinal and transverse directions as two effectively 1D problems. We now assume that a suspension element jams when the shear strain it experiences reaches ε_c, irrespective of propagation direction. This leads to the following relations between k_1^*, k_t^* and ε_c (see Appendix C for details):

$$k_t^* = \frac{1}{2\varepsilon_c}, \ k_1^* = \frac{1}{e^{\varepsilon_c} - 1}, \tag{3.7}$$

and thus

$$k_1^* = \frac{1}{e^{1/(2k_t^*)} - 1}. \tag{3.8}$$

Equation (3.8) is plotted in Fig. 3.4d. For small ε_c, we find from Eq. (3.7) that $k_1^* \approx 2k_t^* = 1/\varepsilon_c$. In other words, the anisotropy ratio of 2 in the normalized front speeds originates from the factor $1/2$ in the non-diagonal terms of the shear rate tensor,

which in turn arises because simple shear can be decomposed into a combination of pure shear and solid body rotation.

In 3D, we cannot quantify the effects of pure shear and simple shear via the same approach. However, we can still represent the magnitude of shear strain with a scalar and calculate the ratio k_l^*/k_t^* assuming the threshold strain to jamming is identical everywhere. One possible solution is to use the "strain intensity" $\mathcal{D}$ [100], which leads to $k_l^*/k_t^* \approx 3/\sqrt{2} \approx 2.12$. Another method is to define the shear rate as $\dot{\mathcal{E}} = \sqrt{(\lambda_1^2 + \lambda_2^2 + \lambda_3^2)/2}$, where λ_1, λ_2, and λ_3 are the eigenvalues of the shear rate tensor (Eq. 3.1), and thus the strain is $\mathcal{E} = \int \dot{\mathcal{E}} dt$. Assuming $\mathcal{E}$ is the same in the longitudinal and transverse directions results in $k_l^*/k_t^* \approx \sqrt{3} \approx 1.73$. Details regarding $\mathcal{D}$ and $\mathcal{E}$ are described in Appendix D. As we can see, although the accurate value of the ratio depends on how the scalar is defined, the ratio is always ≈ 2, which matches the experimental data in 3D systems within our measurement precision. Recent experimental results [101] show that even when the impact is tilted instead of upright, this ratio is independent of the incident angle as long as the front is propagating freely and has no interaction with any solid boundary.

With increasing packing fraction ϕ, we expect the strain threshold ε_c to decrease, which agrees qualitatively with the measurements of ε_c in dry granular systems [27]. Via Eq. (3.7) this explains why k^* increases with ϕ as Fig. 3.4b shows: since it takes less strain to reorganize the particles into a shear-jammed network, the front will propagate faster given the same impact speed. We point out that Eq. (1.6), which formalizes such relationship between packing fraction and front speed, appears to capture the overall trend qualitatively. However, this seems fortuitous, since Eq. (1.6) was based on the assumption that the moving front significantly increases the packing fraction (driving it up to ϕ_J), which we now can rule out in this system. Besides, Eq. (1.6) cannot predict the observed anisotropy in front shape. Our next task, therefore, is to develop a model for $k^*(\phi)$ based on jamming by shear instead of densification. We will provide such a model in Chap. 4.

Another interesting aspect of the data in Fig. 3.4d is the deviation from the anisotropy ratio ≈ 2 at large k^* values or, equivalently, large packing densities. This deviation is most apparent in the data available for the quasi-2D system, and it indicates that the longitudinal speed becomes relatively faster. We speculate that this may be connected to a breakdown of the assumption of an isotropic strain threshold ε_c. For example, if the impact were to introduce a small amount of compression of the particle sub-phase in the longitudinal direction, ε_c would be reduced in that direction. This effect would become increasingly significant at large ϕ. We can model this by introducing a correction δ so that

$$k_l^* = \frac{1}{e^{\varepsilon_c - \delta} - 1}. \tag{3.9}$$

Using $\varepsilon_c = 1/(2k_t^*)$ and $\delta \approx 0.01$, we can reproduce the trend in Fig. 3.4d (dotted red line). However, this is just speculation, and there might be other reasons for the deviation.

3.6 Conclusions

In conclusion, these results provide valuable insights into the mechanism responsible for impact-induced solidification of dense suspensions. The finding that the packing fraction does not increase measurably during impact, together with the observation of strong shear at the leading edge of the propagating solidification fronts, rules out jamming via densification as the dominant mechanism and point to jamming by shear.[2] In dense suspensions, this introduces a new stress scale or, equivalently, an impact velocity threshold, which we associate with the breakdown of lubrication films between particles and the onset of frictional interactions [25, 33, 38, 43, 47, 50]. Behind the front, these frictional interactions create a dynamically shear-jammed region (corresponding to fragile or shear-jammed states in [27, 43]). Further support for the shear jamming scenario comes from the observation of anisotropic front propagation. We quantitatively explained why the front speed in the longitudinal direction is twice as fast as that in the transverse direction, and relate this anisotropy to the ability of the material to transmit shear strain. For dynamic shear jamming, both shear stress and strain need to exceed threshold values, and it is the critical shear strain that determines the front propagation speed.

---

[2]Densification is likely to play a significant role at much larger impact velocities when the interstitial liquid's compressibility can no longer be neglected [93].

Chapter 4
Modeling Shear Fronts in One Dimension

4.1 Introduction

As discussed in Chap. 1, efforts have been made to map out a state diagram that delineates the properties of dense suspensions as a function of packing fraction and the imposed forcing. However, previous work focused almost exclusively on steady-state conditions, which did not capture the many remarkable transient phenomena exhibited by suspensions [28, 52–55, 58, 59, 92, 102]. Only a few years ago it was discovered [54, 59] that the impact-activated solidification is a dynamic process where impact at the suspension surface initiates jamming fronts that rapidly propagate into the bulk of the material and transform the suspension from a fluid-like into a solid-like state in its wake. Since the suspensions are prepared below jamming, these jamming fronts are fundamentally different from the shock waves due to compression or shear observed in granular systems above jamming [103, 104] or in fragile networks [105]. In Chap. 3, with the help of high-speed ultrasound, we showed that the impact-activated solidification is not due to jamming by compression [106, 107]. However, so far, several key aspects have remained largely unresolved, including: (1) the conditions under which dense suspensions can develop jamming fronts; (2) the shape of the flow profile at the front; and importantly (3) the relation between the applied stress and the front speed. These questions underline the need to build a description that would encompass both the transient and steady-state properties of shear thickening and shear jamming materials.

In this chapter, we consider the arguably simplest geometry in which these properties can be measured: a plane of fluid that is sheared along one of its boundaries. The resulting flow field changes only along the direction perpendicular to the sheared boundary, which enables us to consider it as a one-dimensional (1D) system. A key finding here is that the velocity-stress relation measured at the boundary,

---

This chapter is based on [98].

i.e., the macroscopic response of the suspension to applied forcing, is governed by a microscopic, particle-scale quantity: the amount of strain accumulated locally when the jamming front passes through. This accumulated strain depends not only on the intrinsic properties of the suspension, such as the packing fraction, but also on the system's preparation condition. We can capture this transient behavior by introducing one additional parameter, a strain amplitude γ^* characterizing the crossover to steady-state flow, into a model developed initially for steady-state rheology [43]. This generalized model exhibits well-defined jamming fronts and allows us to compute their dependence on packing fraction and forcing conditions, leading to predictions for the three points raised at the end of the previous paragraph, which agree well with our experimental measurements.

4.2 Quasi-One-Dimensional Wide Gap Shear Experiment

As illustrated schematically in Fig. 4.2, our experimental system consisted of a layer of cornstarch suspension and a thin plate inserted in it. Starting from rest, the plate was impacted by a computer-controlled linear actuator (Parker ETT050) and then moved along the y-direction at constant speed U_0. The suspension floated on a heavy, low-viscosity oil (Fluorinert FC-3283 from 3M), which provided a nearly stress-free boundary condition [59]. This allowed us to deduce the stress applied at the boundary from the velocity field that we measured experimentally. A high-speed camera (Phantom V12) was used to image the motion of the suspension surface. The videos were analyzed using a particle imaging velocimetry (PIV) algorithm to obtain the flow field.

4.2.1 Features of Dynamic Shear Fronts

Shear fronts are generated at fast enough boundary speed U_0. The flow field obtained inside the dashed red box in Fig. 4.1 is shown in Fig. 4.2a. Colors represent the y component of local velocities v_y. In the yellow regions, the suspension moved with a velocity very close to $U_0 = 0.46$ m/s, and in the dark green regions, the suspension did not move. We can see a clear boundary between the yellow and green regions that propagate away from the plate and into the bulk. To a good approximation, the flow was a quasi-1D flow. There was a significant velocity gradient along the x direction, but the points at the same x position have almost identical velocities. Therefore, here we average the velocity field in the y direction and leave x as the only spatial coordinate. Figure 4.2b shows the evolution of the resulting averaged velocity profiles. As the red arrows indicate, a moving region rapidly expands outward to either side of the plate, while the shape of the velocity profiles stays approximately invariant.

Fig. 4.1 Illustration of the wide-gap shear experiment. The setup consists of a layer of cornstarch suspension (yellow) that floats on a heavy oil (blue). Dashed black lines represent rubber sheets confining the suspension. An acrylic plate with a roughened surface was inserted in the middle of the container (at $x = 0$ m) and moved with speed U_0. The dashed red box indicates the area used for data analysis. The cross-sectional area S_p is the surface area of the shaded region in the side view
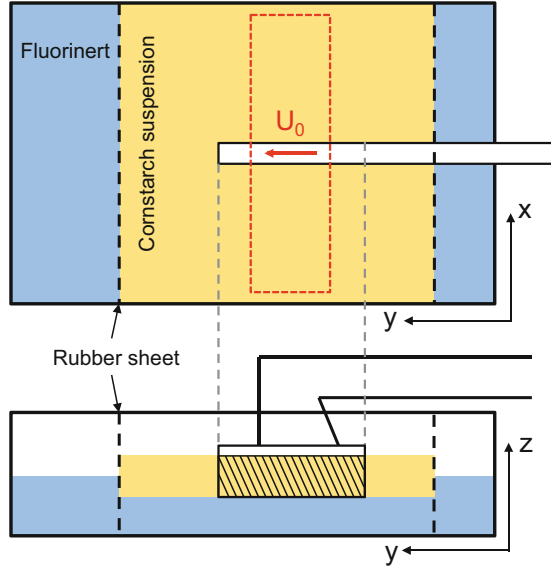
For convenience, we define the front position x_f as the position of the point on a velocity profile where $v_y = 0.45U_0$. As shown in Fig. 4.2c, x_f is a linear function of time on both sides of the plate, providing a well-defined, constant front propagation speed U_f. As an example, here $U_f = 3.60 \pm 0.03$ m/s, which is 7.8 times the plate speed $U_0 = 0.46 \pm 0.02$ m/s, but much slower than the speed of sound in the material (above 1900 m/s, see Chap. 3). Furthermore, we were able to extract the local accumulated strain γ from the flow fields at each time point. Because the velocity profiles are almost invariant in shape, we collapse $\gamma(t)$ at different x by shifting the curves using the time t_f when the front reaches that position, i.e., $x_f(t_f) = x$. Figure 4.2d shows $\gamma(t - t_f)$ after averaging. We can see that γ increases quickly at the beginning but then slows down because of shear thickening. The red curves are power law fits to the data in the region of $t > 0$ ms. Interestingly, the accumulated strain asymptotically approaches a finite value γ_∞ (in this case 0.12) under continued finite stress, which is a clear indicator of jamming.

To obtain the shear rate distribution along the velocity profiles, we averaged them after shifting the front positions x_f to zero. The absolute value of the local shear rate $|\dot{\gamma}| = |dv_y/dx|$ is shown in Fig. 4.2e.[1] The maximum shear rate $\dot{\gamma}_{max}$ is close to the front position. One important observation is that the shear rate profile is not symmetric with respect to $|x| - |x_f| = 0$. It exhibits a steeper gradient at the leading edge ($|x| > |x_f|$), and has a tail of small, but finite shear rate behind the front ($|x| < |x_f|$). Thus, strictly speaking, the region in the wake of the passing front does

---

[1]Since in our 1D system, γ always changes monotonically, we only consider the absolute value of $\dot{\gamma}$ and γ. In this thesis, the signs on $\dot{\gamma}$ and γ are ignored.
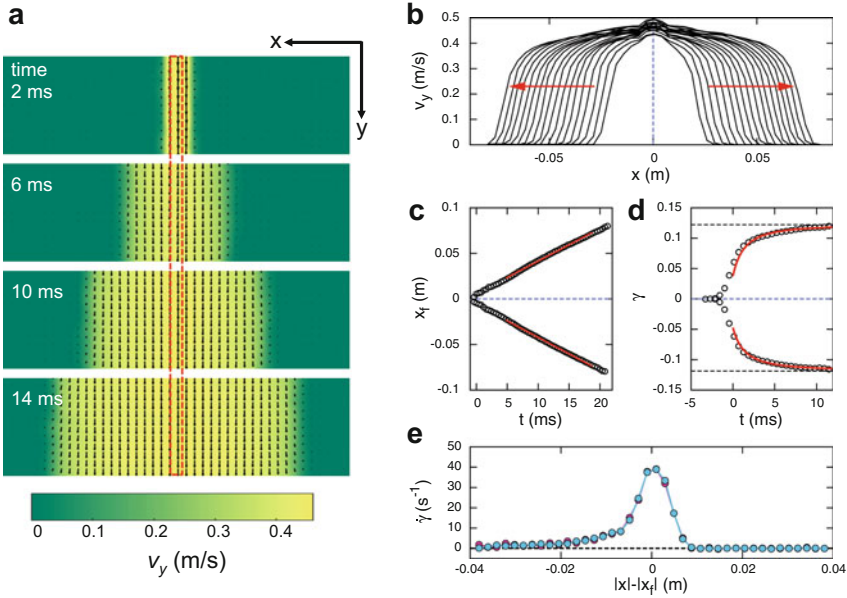
Fig. 4.2 Flow of the shear front obtained from the quasi-1D experiment. (**a**) Flow field on the suspension surface at four different times. Arrows label local velocities. Colors represent v_y. Dashed red box outlines the position and width of the plate. (**b**) Exemplary velocity profiles of a shear front for $\phi = 0.532$ and $U_0 = 0.46 \pm 0.02\,\text{m/s}$, propagating transversely to either side of the plate (dashed blue line). (**c**, **d**) Front position x_f and accumulated strain γ as functions of time t. In (**c**), red lines show the linear fits. In (**d**), time $t = 0\,\text{ms}$ represents the time when $x = x_\text{f}$. Red lines show fits to a power law. Black dashed lines indicate the asymptotic accumulated strain γ_∞. (**e**) Local shear rate calculated from the mean velocity profiles. Blue and pink represent the left and right branches, respectively, in (**b**)

not immediately become a jammed solid. However, as the front keeps moving ahead and the local strain approaches γ_∞, a jammed state with non-zero shear modulus will be reached at the end. By contrast, if a suspension does not "jam" but only shear "thickens," we expect the accumulated strain to keep growing and the shear rate to stay finite.

From this discussion, we extract three defining features for jamming fronts: (1) A well-defined, step-like velocity profile that stays invariant over time; (2) A constant propagation speed U_f; (3) An asymptotically accumulated strain that stays finite. These characteristics distinguish jamming fronts from the more diffusive response to applied shear that occurs at low driving speeds U_0 or low packing fractions, as will be discussed below. We will use these three features in comparing model calculations to the experiments.

4.2.2 Flow Profile at Slow Boundary Speed

Like the impact-activated fronts discussed in Chap. 3, the 1D shear fronts are generated only above a threshold boundary velocity. When U_0 was sufficiently slow, the suspension was in the lubrication regime and behaved like a Newtonian fluid. For a Newtonian fluid sheared in a semi-infinite 1D system, the flow profile is self-similar with a characteristic length scale $\sqrt{\nu t}$, where ν is the kinematic viscosity. If we define a normalized, time-dependent length scale $s_\nu = x/(\sqrt{\nu t})$, the velocity $v_y(x, t)$ is [3]

$$v_y(x, t) = U_0 \left[1 - \mathrm{erf}\left(\frac{s_\nu}{2}\right) \right], \tag{4.1}$$

where $\mathrm{erf}(x)$ is the error function. The numerically calculated and experimentally measured flow profiles at $\phi = 0.521$ and $U_0 = 0.01$ m/s are shown in Fig. 4.3 as an example. One difference is that in the calculation the system was strictly one dimensional and semi-infinite, so the local velocity was always positive during the whole process. However, in the experiment, negative flow velocity was observed further away from the plate, which originated from fluid re-circulation due to the finite container size. However, we can still define the "front position" x_f as the x position at which $u = 0.45 U_0$. As shown in Fig. 4.3c, in the calculation, x_f kept growing as a function of time, and before the flow reached the other boundary it satisfied $x_f \propto \sqrt{\nu t}$, where $\nu = \eta_0 (1 - \phi/\phi_0)^{-2}/\rho$. Here η_0 is the solvent viscosity, ρ is the suspension density, and ϕ_0 is the frictionless jamming packing fraction

Fig. 4.3 Flow profiles in the fluid-like regime and "front" position x_f at $\phi = 0.521$ and $U_0 = 0.01$ m/s. (**a**) Numerical calculation based on the model. (**b**) Experimental data. (**c**) Position of the front, defined as the position where $v_y = 0.45 U_0$
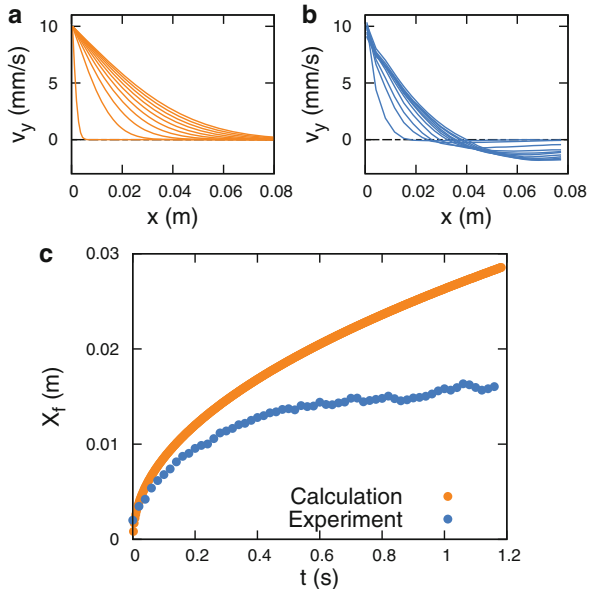
introduced in Sect. 1.3. In the experiments, the front almost stopped propagating at late time and the system reached a steady state.

As U_0 increased, we started to see a front that propagated out. However, before U_0 is sufficiently fast, the flow did not exhibit the three defining features of jamming fronts. For example, the x_f-t relation was not strictly linear at a moderate driving speed. We now focus on the limit of sufficiently fast U_0, where we obtain jamming fronts as defined above. Behaviors of the material at moderate speeds will be discussed more in Chap. 5.

4.2.3   Front Speed and Accumulated Strain

From now on in this section, we will focus on the fast U_0 regime where jamming fronts are generated. We will discuss how U_f, γ_∞, the stress at the boundary Σ, and the maximum shear rate $\dot{\gamma}_{max}$ depend on U_0 at different ϕ, as shown in Fig. 4.4.
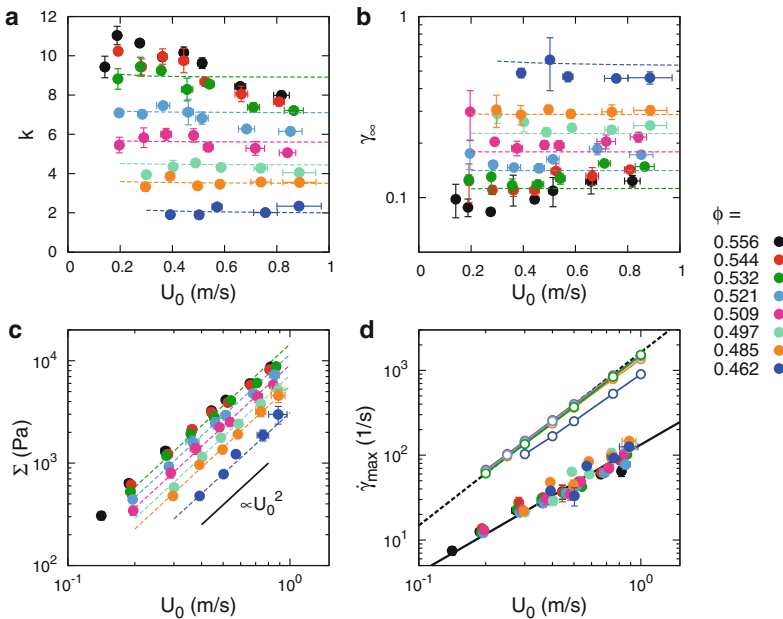
Fig. 4.4 Characteristics of propagating jamming fronts as functions of shearing speed U_0. Solid symbols show experimentally obtained data for different packing fractions ϕ. In (**a–c**), dashed lines are from model calculations. (**a**) Dimensionless front propagation speed k. (**b**) Asymptotic accumulated strain γ_∞. (**c**) Stress at the boundary Σ. Solid circles are calculated by plugging the experimentally measured U_0 and k into Eq. (4.3). Dashed lines show the stress at the boundary obtained from the numerical calculations, which satisfy $\Sigma \sim U_0^2$. (**d**) Maximum shear rate $\dot{\gamma}_{max}$. Open circles are from the model (the same color scheme is used for data from the experiments). Black lines are power law fits
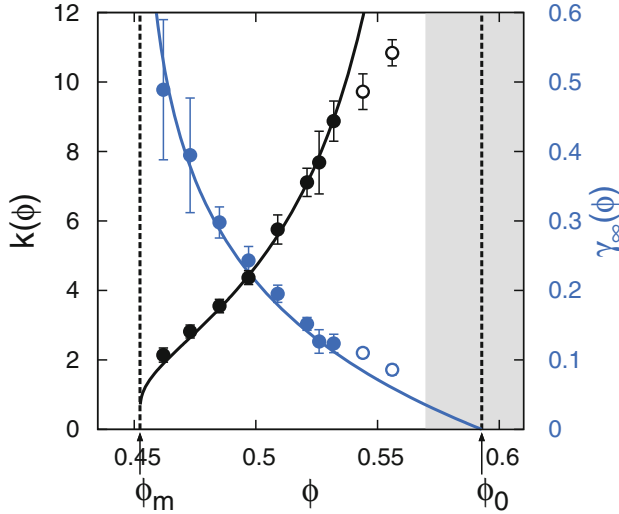
Fig. 4.5 Dimensionless front propagation speed k (black) and asymptotic accumulated strain γ_∞ (blue) as functions of packing fraction ϕ. The blue curve shows Eq. (4.19) and the black curve shows its reciprocal, both with $\gamma^* = 0.197$. Data at $\phi = 0.556$ and 0.544 are represented by open circles

We define the normalized front propagation speed as $k \equiv U_f/U_0$. The variation of k as a function of U_0 is presented in Fig. 4.4a, b shows the corresponding γ_∞. At $\phi \leq 0.5$, both k and γ_∞ are essentially constant. For the highest values of ϕ and U_0 we probed, departures from this constant behavior were detected, an effect whose relative magnitude was as large as 30%. But still, for each $\phi < 0.54$, we find a range in which k and γ_∞ are nearly independent of U_0. Using the average value in such a range, we define $k(\phi)$ and $\gamma_\infty(\phi)$ at each ϕ. Note that $k(\phi)$ increases with ϕ, but the trend is reversed for $\gamma_\infty(\phi)$. These results are documented in Fig. 4.5.

Visual inspections of Figs. 4.4a,b, and 4.5 suggest an inverse relationship between k and γ_∞, which we now derive. The total accumulated strain when the front passes through is $\gamma_\infty = \int_{-\infty}^{+\infty} \dot{\gamma} \, dt$. For a propagating front with an invariant shape, we have $\dot{\gamma} = \frac{\partial v}{\partial x} = \frac{\partial v}{U_f \partial t}$, so that

$$\gamma_\infty = \frac{1}{U_f} \int_0^{U_0} dv = \frac{U_0}{U_f} = \frac{1}{k}. \tag{4.2}$$

Thus, how fast a jamming front propagates depends on how much total strain is accumulated locally as the jamming front moves through. The physical picture is that a finite strain is required to shear the suspension out of an initial state, where the particles are uniformly distributed, into a contact network that jams. The denser the particles pack, the less rearrangement is necessary toward jamming, and consequently, the front propagates faster.

Fig. 4.6 Front position as a function of time for different pre-shear. The fast plate speed was $U_0 = 360\,\text{mm/s}$ and the slow pre-shear speed U_{pre} varied as labeled in the plot. Positive U_{pre} represents pre-shear in the same direction as U_0 and negative U_{pre} was in the opposite direction
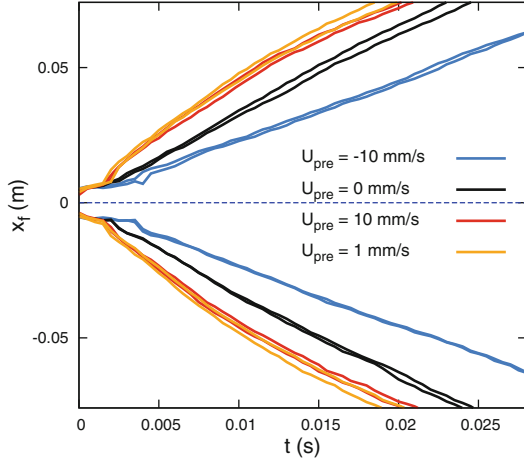
To further prove that the front propagation speed depends on the microscopic particle configuration, we prepared an anisotropic initial state of the suspension by moving the plate at a slow speed U_{pre} before the high-speed shear. We moved the plate 10 mm forward or backward at $U_{\text{pre}} = 1\,\text{mm/s}$ or $10\,\text{mm/s}$, and then applied fast shear at a much faster U_0. Results for $\phi = 0.526$ and $U_0 = 0.36\,\text{m/s}$ are shown in Fig. 4.6 as an example. The front propagated faster (slower) when the suspension was pre-sheared along the same (opposite) direction. This suggests that the front propagation speed not only depends on ϕ but also on the system preparation conditions and straining history.

We performed pre-shear at different U_{pre} (from 0.1 to 10 mm/s), and waited for different lengths of time between pre-shear and fast shear, from several seconds to 10 min. In each case we obtained almost identical x_f-t curves, as long as U_{pre} was slow enough so that the suspension remained fluid-like. It shows that cornstarch suspensions can be treated as an athermal system over time scales as long as several minutes. Note that in our experiments, the velocity profile was not always linear during the pre-shear. This was due to the limited range the plate could move, so the distribution of "pre-strain" was not the same everywhere. When the pre-shear finished, the accumulated strain close to the plate was the maximum, and it decreased gradually to the side. As a result, in the following step, when sheared at speed U_0, U_f slowed down as it propagated away from the plate, which can be seen in Fig. 4.6.

4.2.4   Relation Between Applied Stress and Front Speed

In our system, a relation connecting the applied stress Σ to the velocity U_0 is readily extracted from momentum conservation. The momentum of an elongating jammed

part of the material with a cross-sectional area S_p in the plane perpendicular to the front propagation direction is $p = \rho S_p x_f U_0$. Equating the time derivative of this quantity with the force ΣS_p, one obtains

$$\Sigma = \rho U_0 U_f = \rho k U_0^2, \tag{4.3}$$

where $\rho = 1.63 \times 10^3 \, \text{kg/m}^3$ is the density of the suspension. We calculated Σ with Eq. (4.3) using the experimental data. As Fig. 4.4c shows, the dependence of Σ on U_0 matches a quadratic power law well. Interestingly, the form of Eq. (4.3) is identical to the expression for the dynamic pressure, except that the density is renormalized by a factor k, so the effective density becomes $\rho_{\text{eff}} \sim k\rho$, where k can be as big as a factor of 10 according to our experiments. This "added mass" generated by the propagating fronts was tracked and imaged in previous impact experiments [54, 59, 92].

Note that as the shear stress increases with U_0, so does the normal stress. As the front passes by, the surface of the suspension turns from smooth to matte due to the dilation of grains [108]. The protrusion of particles increases the confining stress applied by surface tension at the suspension-air interface [23]. However, there is an upper limit in confinement stress at the free interface, which is of order 10^3 Pa for our suspensions [13]. As a result, at sufficiently fast U_0 the material could expand near the surface, causing ϕ to decrease in the bulk [34]. This effect may lead to the departure of the power law behavior in Fig. 4.4c for the highest stresses we probed, or equivalently (according to Eq. (4.3)) to the erosion of the U_0-independent behavior of k in Fig. 4.4a. In the model developed below, we neglect this dilation effect. Thus it predicts a constant $k(U_0)$ at fast U_0.

4.2.5 Maximum Shear Rate

The maximum shear rate $\dot{\gamma}_{\text{max}}$ characterizes the steepness of the fronts. It is inversely related to the front width Δ since dimensionally we must have $\Delta \sim U_0 / \dot{\gamma}_{\text{max}}$. Figure 4.4d shows $\dot{\gamma}_{\text{max}}$ as a function of U_0. To a good approximation, the experimental data for different ϕ from 0.462 to 0.532 collapse onto a single curve, revealing a power law of the form $\dot{\gamma}_{\text{max}} \propto U_0^b$, with the exponent $b_{\text{exp}} = 1.51 \pm 0.09$. From this observation we can deduce that $\Delta \propto U_0^{1-b} \propto U_0^{-0.5}$. Since $\dot{\gamma}_{\text{max}}$ is roughly independent of ϕ, we predict the front width to be insensitive to ϕ, which is different from what was found in the case of compression front [106].

4.3 Validating the Original Wyart–Cates Model with Steady-State Rheology

The steady-state rheology experiments were performed with an Anton Paar MCR 301 rheometer. The suspensions were tested between parallel plates, and the

diameter of the upper plate was 25 mm (tool PP25). An enclosed solvent trap was used to prevent evaporation. We performed both shear rate controlled and shear stress controlled experiments at different ϕ. Before each measurement, the suspension was pre-sheared by ramping from $\Sigma = 0.1$ to 100 Pa for 50 s in total, then sheared slowly at $\Sigma = 0.1$ Pa for 30 to 60 s. After these two steps of preparation, we ran the actual measurements, where we took 20 data points in a scan from low to high $\dot{\gamma}$ or Σ (from approximately 0.1 to 1000 Pa). At each point, the measurement lasted for 10 to 30 s, and we made sure that the time was long enough so that the viscosity did not vary with time. Some exemplary viscosity-shear rate data (η-$\dot{\gamma}$ curves) at different ϕ are shown in Fig. 4.7a.

The steady-state model by Wyart and Cates [43] predicts that, for suspensions in the CST and DST regimes, the η-$\dot{\gamma}$ curves have two Newtonian regimes: $\eta_{N,1}$ at low stress and $\eta_{N,2}$ at high stress. Both $\eta_{N,1}$ and $\eta_{N,2}$ increase with ϕ, and the stress threshold Σ^* controls the stress at which the transition occurs from one regime to the other. In the experiments, there are several differences from this model, which we need to account for. Firstly, dense suspensions show shear thinning at
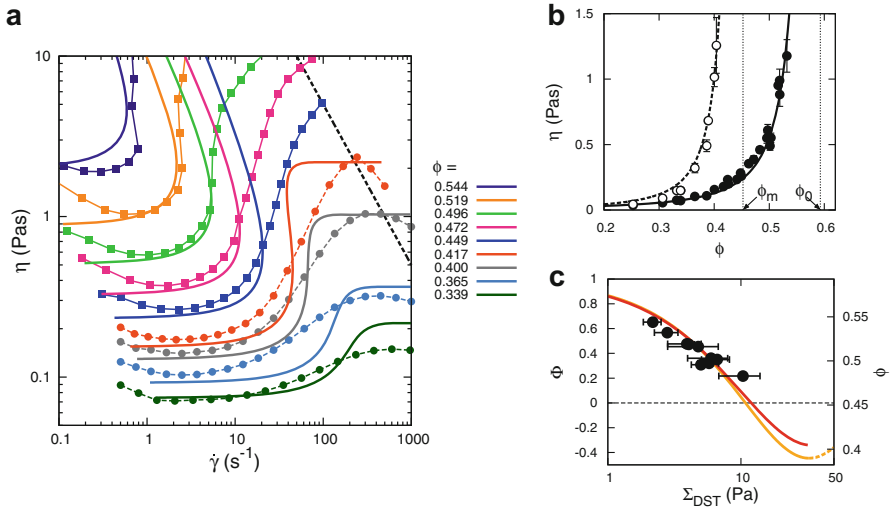
Fig. 4.7 Validate the Wyart–Cates model with steady-state rheology. (**a**) Viscosity η at different shear rates $\dot{\gamma}$ and packing fractions ϕ. Squares connected by thin solid lines represent stress controlled experiments; circles connected by thin dashed lines represent shear rate controlled experiments. The predictions of the Wyart–Cates model are shown by the thick curves with the same color as the experiments. The dashed black line indicates a constant stress $\Sigma = 500$ Pa, which is provided by surface tension and corresponds to the upper limit of stress in steady-state experiments using our shear cell geometry. (**b**) The lower Newtonian viscosity $\eta_{N,1}$ (solid circles) and higher Newtonian viscosity $\eta_{N,2}$ (open circles) at different ϕ. The two curves show the best fit of $\eta_{N,1}$ and $\eta_{N,2}$ with Eq. (4.5). The vertical dashed lines label ϕ_m (left) and ϕ_0 (right) obtained from the fitting. (**c**) Relation between rescaled packing fraction Φ and onset stress Σ_{DST}. For each Φ, the corresponding ϕ is labeled on the right. The solid black points are experimental data. The red curve is the prediction of the model for $\Sigma^* = 20.4$ Pa

low shear rate. To accommodate this, we took the average viscosity in the flat section near the minimum of a η-$\dot{\gamma}$ curve as $\eta_{N,1}$. Secondly, the higher branches of the η-$\dot{\gamma}$ curves are more like smooth peaks instead of plateaus. We therefore took the peak values of η as $\eta_{N,2}$. Lastly, in steady-state rheology experiments, there is another stress limit set by the surface tension at the suspension-air interface, which confines the suspensions between the parallel plates. The empirical relation is $\Sigma_{max} \approx 0.1\Gamma/d$, where Γ is the surface tension of the solvent and d is the particle diameter [13, 23]. The surface tension of our solvent was about 75 N/m, and the average diameter of cornstarch granules was about 15 μm. As a result, Σ_{max} was 500 Pa approximately. Above this stress, the surface tension could not confine the suspension, and the measurements became unreliable, i.e., the data could no longer be used to extract $\eta_{N,2}$.

According to the model, the viscosity of a suspension is

$$\eta = \frac{\Sigma}{\dot{\gamma}} = \eta_0 \left[1 - \frac{\phi}{\phi_J(\Sigma)} \right]^{-2}. \tag{4.4}$$

In the two limits of Σ, Eq. (4.4) has two asymptotes

$$\eta_{N,1} = \eta_0(1 - \phi/\phi_0)^{-2}, \ (\Sigma \to 0),$$
$$\eta_{N,2} = \eta_0(1 - \phi/\phi_m)^{-2}, \ (\Sigma \to +\infty). \tag{4.5}$$

This predicts that though both $\eta_{N,1}$ and $\eta_{N,2}$ increase with ϕ, they grow with different rate and diverge at different ϕ: $\eta_{N,2}$ diverges at $\phi = \phi_m$, while $\eta_{N,1}$ diverges at ϕ_0. Figure 4.7b shows $\eta_{N,1}$ and $\eta_{N,2}$ as functions of ϕ. We fit both $\eta_{N,1}$ and $\eta_{N,2}$ simultaneously on log scales to Eq. (4.5) and obtain the parameters $\eta_0 = 13.6$ mPas, $\phi_0 = 0.593$, and $\phi_m = 0.452$.

We can then use the onset stress of DST, Σ_{DST}, to obtain the threshold stress Σ^*. Σ_{DST} is the stress at the turning point where a η-$\dot{\gamma}$ curve becomes vertical, so we have

$$\left. \frac{d\dot{\gamma}}{d\Sigma} \right|_{\Sigma=\Sigma_{DST}} = 0. \tag{4.6}$$

Now with the three parameters η_0, ϕ_0, and ϕ_m already extracted, Σ_{DST} is only a function of ϕ and Σ^*. Equivalently, we can define a rescaled packing fraction Φ:

$$\Phi = \frac{\phi - \phi_m}{\phi_0 - \phi_m}. \tag{4.7}$$

Figure 4.7c shows the relation between Φ and Σ_{DST} obtained from experiments. To obtain the Σ^* that best fits Φ-Σ_{DST}, we varied Σ^* from 15 to 25 Pa. For each Σ^*, we calculated the Σ-$\dot{\gamma}$ curve and found the corresponding Σ_{DST} at the experimentally measured packing fractions. Then we calculated the sum of squared residuals (SSR)

between the measured and calculated Σ_{DST}, and obtained $\Sigma^* = 20.4\,\mathrm{Pa}$, for the minimum SSR (Fig. 4.10).

The four parameters to describe the steady-state behavior of our suspensions are: $\eta_0 = 13.6 \times 10^{-3}\,\mathrm{Pas}$, $\phi_0 = 0.593$, $\phi_m = 0.452$, and $\Sigma^* = 20.4\,\mathrm{Pa}$. With these in hand, we can calculate the η-$\dot{\gamma}$ relation at any packing fraction and compare it with the experimental measurement, as shown in Fig. 4.7a. The lowest three curves (green, light blue, and gray) are in the CST regime with $\phi < \phi_m$. The next two curves above, at $\phi = 0.417$ and 0.449, are in the DST regime where $\phi_m < \phi < \phi_0$. In this regime, one might expect to see a discontinuous jump in viscosity, while the transitions seen in the experiments are less sharp than the model predicts. We note that this "sharpness" may be affected by the size distribution of the particles. It has been shown that the onset stress of shear thickening is a function of the particle size [50]: The larger the particles, the smaller the onset stress. Since cornstarch is highly poly-disperse, there should be a distribution of onset stress in the system, which smooths the transition. Lastly, the curves at the four highest packing fractions (from 0.472 to 0.544) are in the jamming regime where $\phi > \phi_m$.

4.4   Generalized Wyart–Cates Model for Transient Flows

4.4.1   Generalize the Wyart–Cates Model

The Wyart–Cates model for steady-state rheology of suspensions has been introduced in Sect. 1.3 and tested in Sect. 4.3. To model transient phenomena, consider an initial isotropic state where particles are not touching. There must be a characteristic strain γ^* beyond which the microscopic structure becomes anisotropic, and particles start to make contact. Let us denote the fraction of such particles by $g(\gamma)$, whose contacts can be frictional or not (if the force is insufficient). The exact functional form of $g(\gamma)$ is not crucial, but it must be a growing function, such as:

$$g(\gamma) = 1 - \exp\left(-\gamma/\gamma^*\right). \tag{4.8}$$

The density of frictional contacts can now be estimated as $g(\gamma)f(\Sigma)$. We thus obtain for the jamming packing fraction:

$$\phi_J(\Sigma, \gamma) = g(\gamma)f(\Sigma)\phi_m + [1 - f(\Sigma)g(\gamma)]\phi_0, \tag{4.9}$$

where

$$f(\Sigma) = 1 - \exp(-\Sigma/\Sigma^*), \tag{4.10}$$

and $\Sigma^* = \mu P^*$. Additionally, assuming the viscosity of the transient flow only depends on ϕ_J,[2] we obtain the shear stress (in the spirit of Eq. (1.5)):

$$\Sigma = \eta_0 \dot{\gamma} \left[1 - \frac{\phi}{\phi_J(\Sigma, \gamma)} \right]^{-2}, \tag{4.11}$$

where η_0 is the solvent viscosity. Note that this equation can be applied to higher dimensions as well, where Σ and $\dot{\gamma}$ then indicate the shear stress and shear strain tensors, respectively.[3] Equations (4.8), (4.9), and (4.11) lead to a closed relationship for $\Sigma(\gamma, \dot{\gamma}, \phi)$. If the suspension does not jam, we can take the limit $\gamma \to +\infty$, and Eq. (4.9) reverts back to Eq. (1.4) for a steady-state system, as it should.

4.4.2   Numerical Calculations

Furthermore, to study transient flows such as the fronts, Newton's second law must be included. The equation of motion is

$$\rho \frac{\partial v_y}{\partial t} = -\frac{\partial \Sigma}{\partial x}, \tag{4.12}$$

where the minus sign is because Σ decreases when x increases, but $\partial v_y / \partial t$ is always positive. Here we calculate the velocity and stress distributions in a one-dimensional model system with a finite element method, as illustrated in Fig. 4.8. It is comprised
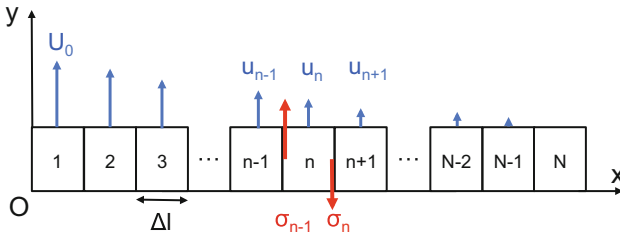
Fig. 4.8 Schematic illustration of the model system used for the numerical calculations. The black boxes represent the fluid elements, the blue arrows represent the local velocities, and the red arrows show the shear stress applied on the left and right boundaries of the n-th element. The boundary conditions are $u_1 = U_0$ and $u_N = 0$. The width of an element is Δl

---

[2]This is a simplification, as the viscosity should not only depend on the fraction of frictional contacts, but also on the anisotropy of the contact network characterized by γ. Our results support that this dependence is not essential to describe fronts.

[3]To describe propagating fronts in two or three dimensions, one may further assume that ϕ is constant in space since particle migration is slow, and the material is incompressible.

of N elements aligned in the x direction as labeled. Each element is allowed to move in the y direction only. The initial condition is zero velocity and zero strain for every element. At the time $t = 0$ s the velocity of the 1st element is set to be U_0 and kept fixed throughout the calculation.

The velocity change of the n'th element Δv_n over a time step Δt is set by the shear stresses σ_{n-1} and σ_n applied on its left and right boundaries, respectively. Using Eq. (4.12), we get

$$\Delta v_n = \frac{\Delta t}{\rho \Delta l}(\sigma_{n-1} - \sigma_n), \tag{4.13}$$

where Δl is the width of individual element. We set $v_1 = U_0$ and $v_N = 0$ throughout the calculation. For the other elements, the velocity $v_n(t)$ is calculated using the forward Euler method. From time step i to $i + 1$, we have

$$v_n(i + 1) = v_n(i) + \Delta v_n(i). \tag{4.14}$$

The stresses $\sigma_{n-1}(v_{n-1}, v_n)$ and $\sigma_n(v_n, v_{n+1})$ are calculated as

$$\sigma_n = \eta_0 \dot{\gamma}_n \left[1 - \phi/\phi_{J,n}\right]^{-2}, \tag{4.15}$$

where

$$\dot{\gamma}_n = \frac{v_n - v_{n+1}}{\Delta l}. \tag{4.16}$$

In Eq. (4.15), $\phi_{J,n}$ is calculated according to the generalized model discussed above (Eqs. 4.8–4.10). The increment of strain to calculate $g(\gamma)$ in every step is

$$\gamma_n(i + 1) = \gamma_n(i) + \dot{\gamma}_n \Delta t. \tag{4.17}$$

Note that in the transient regime the inertia of the suspension plays a role on the macroscopic scale because of the acceleration term $\partial \mathbf{u}/\partial t$. However, on the length scale of a particle, the Stokes number $St = \rho_p d_p^2 \dot{\gamma}/\eta$ [40] is still at least two orders of magnitude smaller than one in our experiments. Some basic parameters are: particle diameter $d_p \approx 15\,\mu$m; density of the particles ρ_p matched to the density of the solvent ρ_l, $\rho_p = \rho_l \approx 1.6 \times 10^3$ kg/m^3; dynamic viscosity of the solvent $\eta \approx 14$ mPas. Even at the maximum shear rate applied in the experiments, $\dot{\gamma} \approx 200\,\text{s}^{-1}$, we get $St \approx 5 \times 10^{-3} \ll 1$. As a result, the "no inertia" requirement of the original model by Wyart and Cates [43] is still met.

On the macroscopic level, when it comes to the effect of inertia in a transient flow, we need to consider both terms in the material derivative of velocity $\partial \mathbf{u}/\partial t + (\mathbf{u}\cdot\nabla)\mathbf{u}$ in the Navier–Stokes equations. In a steady flow $\partial \mathbf{u}/\partial t = 0$, and the effect of inertia is indicated by the Reynolds number Re, which is the ratio between the inertia term $(\mathbf{u} \cdot \nabla)\mathbf{u}$ and the viscous term $\nu\nabla^2\mathbf{u}$. In a transient flow, however, the $\partial \mathbf{u}/\partial t$ term

should also be considered. In our case, the time scale T for the front to propagate through its width Δ is $T \sim \Delta/(kU_0)$, and this time is also comparable to the time for the suspension to accelerate from 0 to U_0. This allows us to estimate the order of each term:

$$O\left(\frac{\partial \mathbf{u}}{\partial t}\right) \sim O\left(\frac{U}{T}\right) \sim \frac{kU_0^2}{\Delta},$$

$$O\left((\mathbf{u} \cdot \nabla)\mathbf{u}\right) \sim O\left(\frac{U^2}{L}\right) \sim \frac{U_0^2}{\Delta}, \quad (4.18)$$

$$O\left(\nu\nabla^2\mathbf{u}\right) \sim O\left(\nu\frac{U}{L^2}\right) \sim \nu\frac{U_0}{\Delta^2},$$

where U, L, T represent the characteristic speed, length, and time scales, respectively. In our experiments k ranges from ~ 2 to ~ 10 depending on ϕ (Fig. 4.5), thus $\partial \mathbf{u}/\partial t$ is several times larger than $(\mathbf{u} \cdot \nabla)\mathbf{u}$, except for ϕ very close to ϕ_{m}. Actually, in an ideal one-dimensional system (with this specific geometry), the $(\mathbf{u} \cdot \nabla)\mathbf{u}$ term simply vanishes because the direction along which the flow velocity varies is perpendicular to the direction of the flow itself. So finally, it is a balance between the acceleration term $\partial \mathbf{u}/\partial t$ and the viscous term $\nu\nabla^2\mathbf{u}$, just in this case ν is not a constant. As a result, before the front reaches any outside boundary, the inertia will always play a role. The suspension close to the front is accelerating, thus there must be a stress gradient. This should be a valid result as long as the flow in the suspension is still laminar and no circulation or instability is generated.

4.4.3 Transition from Slow to Fast U_0

To better understand the transition from slow U_0 to fast U_0, we look at the evolution of the Σ-$\dot{\gamma}$ relation as γ accumulates, as shown in Fig. 4.9. The Σ-$\dot{\gamma}$ relation for a steady-state system is labeled by the dashed black curve in (d). Since $\phi > \phi_{\mathrm{m}}$, it intersects with the $\dot{\gamma} = 0\,\mathrm{s}^{-1}$ axis and does not have an upper branch. However, in the generalized model, since we introduced the $\mathrm{g}(\gamma)$ term, the Σ-$\dot{\gamma}$ relation evolves as γ accumulates. When $\gamma = 0$, the relation between Σ and $\dot{\gamma}$ is linear with a constant viscosity $\eta_0(1 - \phi/\phi_0)^{-2}$. As γ increases, the Σ-$\dot{\gamma}$ curve turns from linear to sigmoidal, and finally approaches the black dashed line as $\gamma \to +\infty$.

Given the Σ-$\dot{\gamma}$ relation at any γ, we now discuss, as a specific example, the variation of Σ with $\dot{\gamma}$ in element number two of the numerical 1D system, which we call the "state" of that element. When $U_0 = 0.01$ m/s, the state moves up along the Newtonian fluid line and then turns back down along an almost identical path as $\dot{\gamma}$ is varied (black line). In contrast, at $U_0 = 0.5$ m/s, the stress quickly reaches the upper branch of the sigmoidal curves and stays up there as γ keeps accumulating and $\dot{\gamma}$ slows down. If γ keeps increasing, the shear rate approaches $\dot{\gamma} = 0\,\mathrm{s}^{-1}$. Since
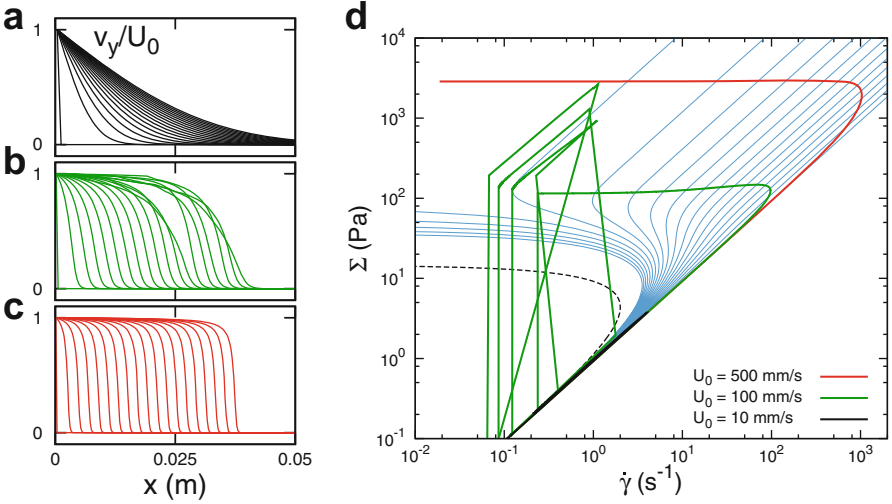
Fig. 4.9 (**a**–**c**) Velocity profiles at different times for $\phi = 0.521$, $U_0 = 0.01$ m/s (**a**), 0.1 m/s (**b**), and 0.5 m/s (**c**). (**a**) is in the fluid-like regime, (**b**) is in the unstable regime, and (**c**) is in the front regime. (**d**) Evolution of Σ-$\dot{\gamma}$ at $\phi = 0.521$. The blue curves show the Σ-$\dot{\gamma}$ relations at different γ (starting from zero, with strain increments of 0.0105 between adjacent curves), as predicted by the generalized Wyart–Cates model. The dashed black line corresponds to the relation at steady state ($\gamma \to +\infty$). The thick black, green, and red lines show the relation between stress and shear rate in element no. 2, calculated numerically for different U_0 as indicated

Σ stays constant, the viscosity of the suspension diverges as $\dot{\gamma} \to 0$, which leads to a jammed state (red line). At intermediate U_0, the system can enter a regime where the flows become unstable (green lines). Here the stress reaches the upper branch and forms a plateau at the beginning. However, as γ accumulates and $\dot{\gamma}$ slows down, the state of the element (at that stress level) enters a section of the S-shaped Σ-$\dot{\gamma}$ curves with a negative slope. As a consequence, the stress has to jump down to the lower branch and then build up again. As this cycle repeats, the flow becomes unstable.

4.5 Validation of the Generalized Model

4.5.1 Qualitative Predictions of the Model

When U_0 (or equivalently the stress Σ) is sufficiently small, $\phi_J \approx \phi_0$ and the viscosity is constant according to Eq. (4.11). Injecting this relation into Eq. (4.12) leads to a diffusion equation, and one recovers the usual flow profile for a Newtonian liquid, evolving with a characteristic length scale $\sqrt{\nu t}$ toward a steady-state shear
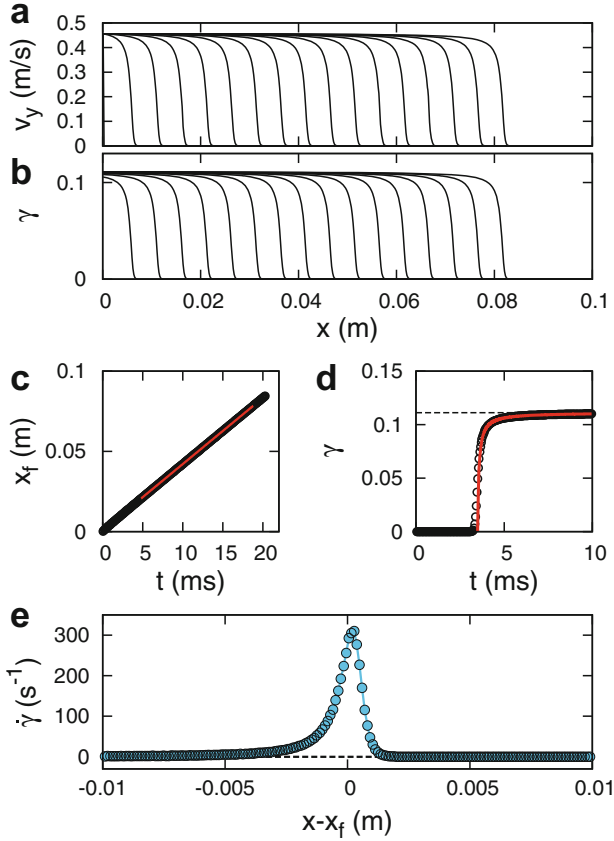
Fig. 4.10 Calculated 1D front based on the generalized Wyart–Cates model. The parameters used in the calculation are obtained from Sect. 4.3. Here we used $\phi = 0.532$ and $U_0 = 0.456$ m/s, so the results can be directly compared with the experiment shown in Fig. 4.2. (**a, b**) Velocity profiles and accumulated strain γ at different time. (**c**) Front position x_f as a function of time. The red line shows a linear fit. (**d**) Accumulated strain γ as a function of time in element $n = 80$. The red curve is a fit to a power law. The dashed black line indicates the asymptotic strain. (**e**) Local shear rate calculated from the mean velocity profile

flow, where ν is the kinematic viscosity. We did recover such a diffusive profile in our finite element implementation of the model, as shown in Fig. 4.9a.

By contrast, if U_0 is large and $\phi > \phi_m$, then there must exist a front separating the solid-like and fluid-like regions. According to Eq. (4.3), this front must move with a constant speed. This was recovered in our numerics as well. Figure 4.10 shows the numerically obtained velocity (a) and local accumulated strain (b) profiles at different times, as well as the front location x_f (c), the accumulated strain γ at a fixed position(d), and local shear rate $\dot{\gamma}$ (e). The parameters are indicated in the figure caption, and they were chosen (see below) to correspond to the experimental

data in Fig. 4.2, allowing a direct comparison. The model reproduces a front that propagates with a constant speed. The local accumulated strain always approaches a finite value asymptotically, which is in close agreement with observations. The shape of the $\dot{\gamma}(x)$ curve plotted in panel (e) also agrees with the experimental data in several key aspects. The maximum shear rate is obtained near $x = x_f$, and both curves show asymmetry with respect to $|x| - |x_f| = 0$: $\dot{\gamma}$ grows quickly as the front approaches, but decays with a tail after the front has passed by. However, the front is sharper than in the experiments, which will be quantified later.

Finally, at intermediate U_0 the model predicts a regime of instability (not seen in our experiments), exemplified in Fig. 4.9b. After propagating across a certain distance, the shape of the velocity profile in the co-moving frame oscillates back and forth. Such instability is not entirely surprising: for these velocities, the stress Σ lies inside the S-shaped portion of the flow curves (see Sect. 4.4). In that stress range, a complex sequence of instabilities and chaotic behaviors in steady-state systems have been reported experimentally [109], which appears to be sensitive to the presence of a free surface that can be deformed. Modeling the front in this velocity regime in the one-dimensional geometry discussed here may thus require to allow for deformation of the free surface. This goes beyond the scope of this work, and here we focus on the fast U_0 regime.

4.5.2 Quantitative Comparison with Experiments

There are five parameters in our model, but we can obtain four of them, ϕ_0, ϕ_m, η_0, and Σ^*, from steady-state rheology. This is shown in Sect. 4.3 where we obtain $\phi_0 = 0.593$, $\phi_m = 0.452$, $\eta_0 = 13.6\,\text{mPa·s}$, and $\Sigma^* = 20.4\,\text{Pa}$. We are left with a single parameter, $\gamma^* = 0.197 \pm 0.002$, obtained by fitting the front propagation speed k and its inverse γ_∞ at different ϕ, as shown in Fig. 4.5. Interestingly, a threshold strain of approximately 0.2 is also found in regular granular materials [110] and in suspensions [102] as the strain scale below which transient, start-up behavior is observed.

Note that the most essential predicted quantities (k and γ_∞) can be estimated analytically in our model in the limit of large U_0. In this case, the stress is so large when the front passes through that we may take $f(\Sigma) \approx 1$ in Eq. (4.9). Jamming occurs when $\phi_J = \phi$, leading to $g(\gamma^*) = (\phi_0 - \phi)/(\phi_0 - \phi_m)$. For our choice of g this implies

$$\gamma_\infty = \gamma^* \cdot \ln\frac{\phi_0 - \phi_m}{\phi - \phi_m}. \tag{4.19}$$

To further test the model we compute k, γ_∞, Σ, and $\dot{\gamma}_{max}$ across a range of packing fractions ϕ and boundary speeds U_0, and compare the results with experiments directly in Fig. 4.4. As follows from Eq. (4.19), we predict k and γ_∞ to be essentially independent of U_0 for large values, and $\Sigma \sim U_0^2$. These

predictions match the data very well at each ϕ (except for the largest ϕ values where k shows some decay, presumably induced by the deformation of the free interface, as discussed above).

As shown in Fig. 4.4d, $\dot{\gamma}_{max}$ obtained from experiments (solid circles) and calculations (hollowed circles) both obey power laws as functions of U_0, and their pre-factors are both relatively ϕ-independent over the range $\phi \in [0.462, 0.532]$ (see Appendix E). However, the model predicts an exponent around $b = 2$ instead of $b = 1.5$, and the pre-factor is about one order of magnitude larger. For both transient and steady-state systems (see Sect. 4.3), the model overestimates the sharpness of the transition from low to high viscosity. Firstly, this could be due to the complexity of cornstarch granules (irregular shape, poly-dispersity, etc.). Secondly, more sophisticated models describing not only the fraction of frictional contacts but also the evolution of the anisotropy of the contact network with strain may be required for a more detailed treatment of the front width.

4.6 Conclusions

By studying the rapidly propagating jamming fronts generated when applying a sudden shear, we proposed and validated a phenomenological framework for fluid–solid front propagation in dense particulate suspensions. We found that besides the applied stress, the properties of such fronts are controlled by the local accumulated shear strain as well. These transient, start-up dynamics can be captured by introducing a characteristic strain scale γ^* into a model [43] that describes the steady-state rheology of shear-thickening suspensions. Despite its simplicity, this extended model gives good agreement with the experiments. It quantitatively reproduces the dependence of the normalized front speed k and the locally accumulated shear strain γ_∞ on the packing fraction ϕ. It also correctly predicts the qualitative relation between the maximum shear rate $\dot{\gamma}_{max}$ and the system and forcing parameters.

Importantly, the generalized model introduced here establishes a direct link between the steady-state and transient behaviors in dense suspensions. It shows that to obtain jamming fronts, the packing fraction of the suspension must be above the frictional jamming packing fraction ϕ_m. In the range between ϕ_m and the frictionless jamming packing fraction ϕ_0, the suspension will evolve into a state that jams at high stress, but can still flow at low stress.

While we discussed the model in its simplest form, appropriate for a semi-infinite 1D system, the same ideas and numerical approaches should allow for several extensions. This includes accounting for the presence of walls (which can take up significant stress once reached by the fronts) as well as extensions to 2D or 3D systems (where the fronts propagate with different speeds in the directions along the applied forcing and perpendicular to it as discussed in Chap. 3 and in [59, 92, 102]).

Chapter 5
Rheology in the Shear Jamming Regime

5.1 Introduction

Non-Newtonian behaviors of suspensions include continuous shear thickening (CST) [17, 19, 20] and discontinuous shear thickening (DST) [13, 22, 23]. Even richer dynamics occur when ϕ approaches the threshold for jamming [7, 27]: at sufficiently high shear stress, suspensions can reversibly transform from a viscous fluid into a solidified state [28, 54]. Experiments [23, 24, 33, 34, 36, 47, 50] and simulations [38, 111] both suggest that strong thickening and solidification due to shear are related to a stress-dependent change in particle–particle interactions, which switch from lubrication at low stress to direct, frictional contact at high stress. In Chap. 1, we have introduced a phenomenological model developed by Wyart and Cates [43] that unifies CST and DST within a framework based on such stress-dependent interactions. Predictions of this model for the shear thickening regime have been validated by experimental [50, 51, 109] and numerical [39–41, 111] work. However, the model also predicts the transition into the shear-jammed, solid-like state, which has not yet been tested.

A key reason for this is that conventional rheology experiments, as well as simulations, establish steady-state shearing conditions and assume spatially uniform flows. Neither of these is appropriate in situations where a fluid is about to transform into a solid. Stress-activated solidification in dense suspensions has been studied extensively under non-stationary conditions, including impact [54–56, 92], extension [58, 102], and simple shear [28, 98]. In each case, rapid external forcing turns the suspension into a jammed solid, which can "melt" and return to a fluid state once the applied stress vanishes [28, 52–54]. The critical element here is that this dynamic jamming, irrespective of how it is triggered, proceeds via propagating fronts that build up a region that sustains high stress between the front and the solid driving boundary. In Chap. 4, we have brought up the point that in the co-moving frame, such flows can establish a local environment that is exquisitely stress controlled [98].

In this chapter, we are going to compare steady-state rheology in a narrow gap, and transient flows in a wide gap, for suspensions in the shear jamming regime. We will demonstrate how propagating fronts can be exploited to perform stress-controlled rheology in regimes inaccessible to methods based on steady-state driving. For the first time, we quantitatively test a significant prediction of the Wyart–Cates model [43]—the location of the boundary delineating DST and shear-jammed states as a function of packing fraction and applied stress.

5.2 Limitations of Narrow-Gap Steady-State Rheology

Under steady driving conditions, the state of a dense suspension with packing fraction ϕ can be described by two parameters: the shear stress Σ and the shear rate $\dot{\gamma}$. Together, they define a flow curve. As an example, the black line in Fig. 5.1a shows the flow curve predicted by the Wyart–Cates model [43] for a suspension in the shear jamming regime under stress-controlled conditions. With increasing Σ it bends back towards low $\dot{\gamma}$, and eventually, intersects with the vertical axis where $\dot{\gamma} = 0$ s^{-1}. At that intersection, the suspension can sustain non-zero shear stress at zero shear rate, and therefore must have developed a finite, non-zero shear modulus. This means the suspension is now jammed. We call the stress at this point the onset stress of shear jamming (SJ) Σ_{SJ}. As Σ increases, presumably, the jammed suspension remains solid (the vertical portion of the black line along the y-axis), until Σ eventually exceeds the yield stress of the jammed solid (not shown). Note that throughout this chapter, we plot flow curves in a conventional manner, with Σ
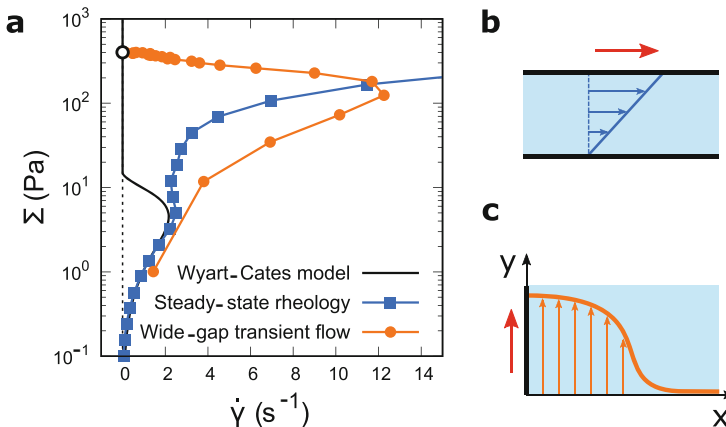

Fig. 5.1 (**a**) Relation between shear stress Σ and shear rate $\dot{\gamma}$ for a suspension in the shear-jamming regime. Steady-state rheology was performed with parallel plates sketched in (**b**), and the transient flow in a wide-gap geometry is shown in (**c**). Red arrows indicate the motions of the solid boundaries

on the y-axis, even though we are discussing stress-controlled protocols where Σ is the independent variable.

However, when this model is compared to steady-state experimental data (blue squares in Fig. 5.1a), we see apparent deviations. The data were taken with a cornstarch suspension of $\phi = 0.52$, using a parallel-plate geometry (Fig. 5.1b) under stress-controlled shearing conditions. Its concentration was well above the frictional jamming packing fraction $\phi_{\mathrm{m}} = 0.45$ (see Chap. 4), which is the lower limit of ϕ that allows shear jamming. Though the model works well at $\Sigma < 5$ Pa, the measured Σ–$\dot{\gamma}$ curve bends only slightly towards low $\dot{\gamma}$ at high Σ. Instead of intersecting with the $\dot{\gamma} = 0$ s^{-1} axis as expected for shear jamming, the curve eventually bends forward again. Such a behavior is typical for DST, a regime in which the Wyart–Cates model predicts s-shaped Σ–$\dot{\gamma}$ curves [43, 50, 51]. The question thus arises: what causes these deviations from the model?

Rheology experiments can be performed with a variety of geometries, including parallel plates, cone and plate, and concentric cylinders (Couette cell). For these three geometries, the basic idea is similar: the sample is placed inside a narrow gap (normally 0.1–1 mm) and sheared continuously. In order to obtain the correct viscosity from such measurements, certain conditions must hold: the flow must be steady such that $\partial\mathbf{u}/\partial t = 0$; $\dot{\gamma}$ and Σ in the bulk must have well-defined spatial profiles so they can be calculated from the boundary conditions; and there can be no boundary slip. For Newtonian fluids, the velocity profile across the gap can be calculated straightforwardly (e.g., it is linear for a parallel plate geometry as shown in Fig. 5.1b), but for dense suspensions, this can become more complex [24, 63]. When Σ exceeds the onset stress of DST, Σ_{DST}, there are complex spatial and temporal rate fluctuations even though the average stress at the boundary remains constant [109, 112–114] and, in addition, boundary slip can be significant [28, 63, 113, 115]. As a result, it is exceedingly difficult to maintain a uniformly sheared jammed state under steady-state driving or to even approach a jammed state in a truly stress-controlled manner with typical, narrow-gap rheology experiments.

5.3   Steady-State Rheology Using One-Dimensional Transient Flows

As shown in Fig. 5.1a, there is another, experimentally accessible, path to shear jamming. Instead of moving up along the black curve, we can get toward shear-jammed states (e.g., the state indicated by the open black circle) as asymptotic limits of specific Σ–$\dot{\gamma}$ paths like the one indicated by the orange circles. These data were taken with the same suspension, but using a wide-gap shear configuration shown in Fig. 5.1c. Note how this curve bends back significantly and gets much closer to the vertical axis than the blue data. We now describe how the flow curves of this type can be used to perform rheology measurements.

The experimental setup for the wide-gap shear is identical to the one described in Chap. 4. A 1 cm thick, horizontal layer of suspension was floated on a heavy oil, and a straight vertical plate in the suspension was used as the solid boundary that applied the shear. Figure 5.1c sketches the top view of the system. In each test, the solid boundary on the left moves with a constant speed U_0 along the y-direction. Immediately after start-up, a transient flow develops in the x-direction, perpendicular to the movement of the boundary, and spreads across the initially quiescent suspension. For suspensions with $\phi > \phi_m$, this flow generates a shear jamming front when U_0 is sufficiently fast, i.e., the applied stress is sufficiently large. As discussed in Chap. 4, the profile of such a front has an approximately invariant shape, thus it can be represented as

$$F(x, t) = F(x - U_f t), \tag{5.1}$$

where F can be Σ, $\dot{\gamma}$, or the y component of the velocity v. We define the front position x_f as where $v = 0.45 U_0$, which is also approximately where $\dot{\gamma}$ peaks. The front propagates with a constant speed $U_f \equiv k U_0$, where k is the dimensionless front propagation speed. With increasing U_0, k plateaus at k_p, which increases with ϕ.

To use the fronts for rheology, we need to know the local shear rate and stress. Given our effective 1D flow, the equation of motion is

$$\rho \frac{\partial v}{\partial t} = -\frac{\partial \Sigma}{\partial x}, \tag{5.2}$$

which reflects the fact that the viscous stress is always balanced by the acceleration of the suspension. This equation allows us to obtain the local shear stress without measuring forces, simply by calculating the stress needed for the suspension to accelerate. From Eqs. (5.1) and (5.2), we obtain $\Sigma = \rho U_f v$, and therefore $\Sigma(x, t)$ has the same shape as $v(x, t)$, but with a prefactor ρU_f. The mean velocity profile $v(x - x_f)$ is shown in Fig. 5.2a. Here $v(x, t)$ was shifted by x_f and then averaged to obtain $v(x - x_f)$. The corresponding shear stress is shown in Fig. 5.2b. As $(x - U_f t) \to -\infty$, $v \to U_0$, and Σ asymptotically approaches $\Sigma_\infty = \rho k U_0^2$. Since this stress originates from the acceleration of the whole flow, which develops with little variation in shape before the front reaches a solid boundary, Σ_∞ is very stable. Note that here we assumed no boundary slip, but it is not necessary because we obtained Σ from velocity measurement instead of the force applied on the boundary (like in standard rheology).[1]

The local shear rate $\dot{\gamma} = |\partial v / \partial x|$ calculated from the averaged velocity profile is also shown in Fig. 5.2b. Because ours is a 1D system, we take $\dot{\gamma}$ to be positive for simplicity. We can see that both Σ and $\dot{\gamma}$ increase at the leading edge of the front ($x > x_f$). However, behind the front ($x < x_f$), Σ keeps increasing and approaches

---

[1]The boundary slip is minor according to our measurements. It only happens at extremely high ϕ and Σ. Even if the boundary slightly slips, as long as the slip is not intermittent, the conclusions above are still valid by replacing U_0 with the actual speed of the flow right next to the boundary.
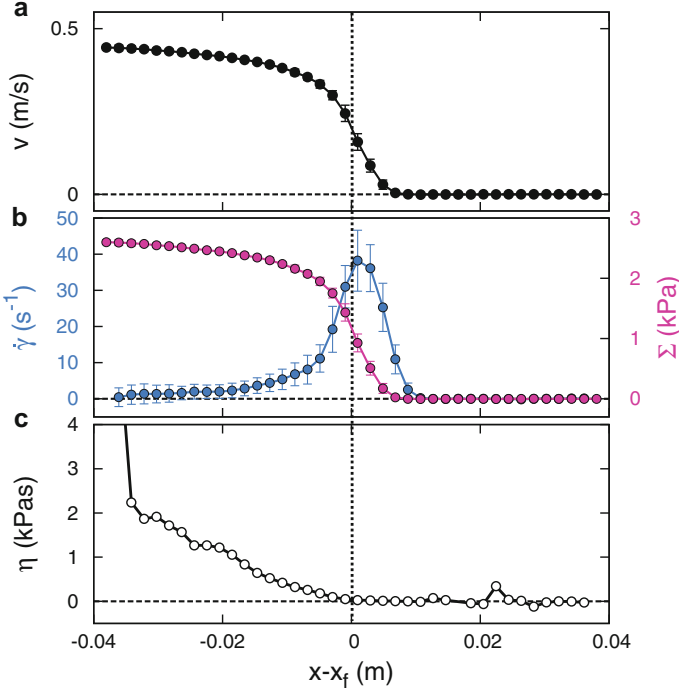
Fig. 5.2 Front profiles in the co-moving frame for a suspension with $\phi = 0.53$. (**a**) Velocity profile $v(x - x_f)$. (**b**) Shear stress Σ (magenta) and shear rate $\dot{\gamma}$ (blue) profiles. (**c**) Local viscosity $\eta = \Sigma/\dot{\gamma}$

Σ_∞, while $\dot{\gamma}$ decreases and approaches zero. This means that the viscosity $\eta = \Sigma/\dot{\gamma}$ increases dramatically behind the front, as shown in Fig. 5.2c. Using our suspension at $\phi = 0.53$ as an example, its viscosity in the Newtonian regime prior to shear thickening was $\eta_N = 1.3$ Pa·s. At only 2 cm behind the front x_f, the suspension is already almost 1000-fold more viscous than η_N.

Moreover, compared to DST under steady-state conditions, where $\eta \propto \Sigma$, the viscosity increase here is "beyond discontinuous," because now $\eta(\Sigma)$ diverges as $\Sigma \to \Sigma_\infty$. In other words, once the front passes, the suspension will evolve toward a solid-like, shear-jammed state with a finite shear modulus so that $\dot{\gamma}|_{t \to +\infty} \to 0$.

While we plot the orange curve in Fig. 5.1a together with the steady-state prediction and experiment, this transient flow curve needs to be interpreted differently. For any point on a steady-state flow curve, the overall accumulated strain γ is irrelevant since the curve describes a stationary state. In contrast, under transient conditions, the state of the suspension evolves with time, and each point on the Σ–$\dot{\gamma}$ curve corresponds to a different γ. For the orange curve in Fig. 5.1, this evolution begins with $\gamma = 0$ at small Σ. As the strain accumulates while the front sweeps through, the suspension experiences increasing shear stress Σ and shear rate $\dot{\gamma}$. In accordance
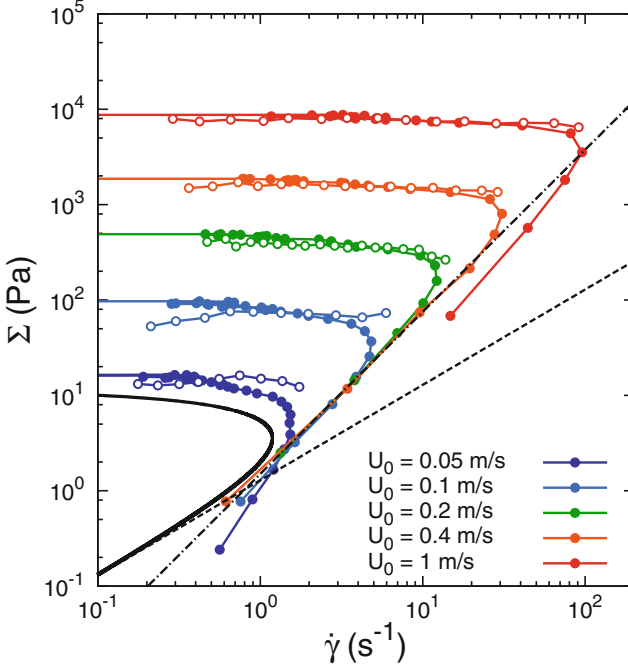
Fig. 5.3 Σ–$\dot{\gamma}$ flow curves for a suspension with $\phi = 0.53$, driven at different boundary speeds U_0. The solid circles represent data obtained from the velocity profiles as in Fig. 5.2. The open circles are obtained by calculating $\dot{\gamma}$ and Σ at each time, and then averaging. The solid black curve shows the prediction of the Wyart–Cates model. The dashed black line shows $\Sigma = \eta_N\dot{\gamma}$. The dash-dot black line is $\Sigma \propto \dot{\gamma}^{1.7}$

with Fig. 5.2b, $\dot{\gamma}$ then abruptly decreases until the flow curve terminates on the vertical axis.

Importantly, the specific stress level within the range of jammed states that is approached in this manner is fully controlled by U_0. This means that by changing U_0, we can drive the suspension toward different jammed stress levels Σ_∞, as shown in Fig. 5.3. We used two analysis methods to obtain the data here: The solid points are from the mean velocity profiles $v(x - x_f)$, and Σ and $\dot{\gamma}$ were extracted the same way as in Fig. 5.2. The open circles were obtained by first calculating Σ and $\dot{\gamma}$ from the velocity profiles at each time step, and then averaging Σ and $\dot{\gamma}$. The two methods provide well-matched results, especially at large U_0.

5.4   Boundary of Shear Jamming in Suspensions

We now use this wide-gap method to probe suspensions in a stress-controlled manner and map out the onset stress Σ_{SJ} of steady-state shear jamming. To obtain Σ_{SJ}, we need to find the stress above which such jamming fronts can be generated.

Fig. 5.4 (**a**) Normalized dimensionless front propagation speed k/k_p as a function of shear stress Σ_∞ for different packing fractions ϕ. (**b**) Predictions of the generalized Wyart–Cates model (Eq. 5.6)
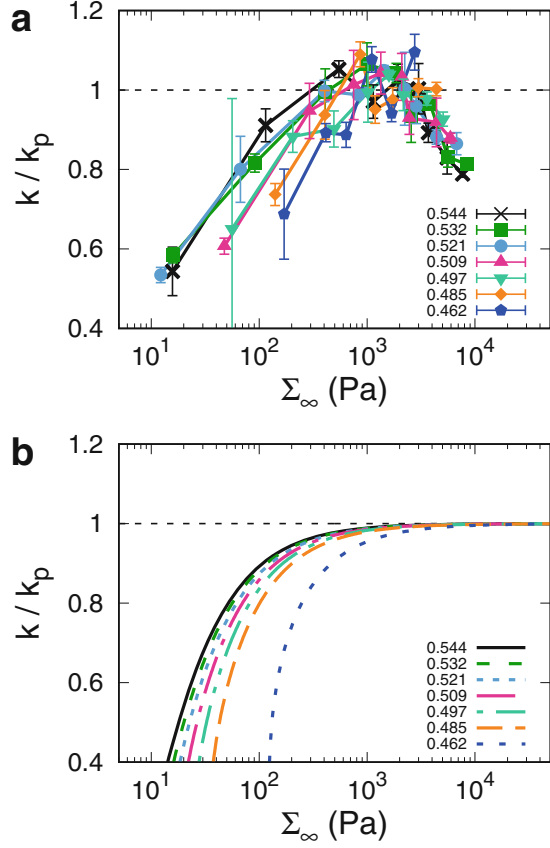
To be more quantitative, we not only find the conditions under which a jamming front is observed but also look at its dimensionless front speed k as a function of Σ_∞ as shown in Fig. 5.4a. In the shear jamming regime, since $\dot{\gamma} \rightarrow 0\,\text{s}^{-1}$ eventually, the accumulated strain (area under the blue curve in Fig. 5.1b) approaches a finite value γ_∞ asymptotically. The dimensionless front propagation speed is directly controlled by this asymptotic strain, as $k = 1/\gamma_\infty$ (see Chaps. 3 and 4 for details). Since γ_∞ is a function of ϕ, so is k. For suspensions prepared with different ϕ, we normalize $k(\phi)$ by its mean peak height, $k_p(\phi)$. In general, k/k_p grows from 0 to 1 as Σ_∞ increases, with suspensions at smaller ϕ requiring larger stress Σ_∞ to reach the same k/k_p.

Now we compare the experimental measurements with the generalized Wyart–Cates model described in Chap. 4, in which the constitutive relation is written as

$$\Sigma = \eta_0 \dot{\gamma} \left[1 - \frac{\phi}{\phi_0 - f(\Sigma)g(\gamma)(\phi_0 - \phi_m)} \right]^{-2}, \qquad (5.3)$$

where η_0 is the solvent viscosity and ϕ_0 is the frictionless jamming packing fraction. As long as f and g are continuous monotonic functions that satisfy $f(0) = g(0) = 0$ and $f(+\infty) = g(+\infty) = 1$, the model works qualitatively. For the suspensions that we use, $g(\gamma) = 1 - \exp(-\gamma/\gamma^*)$ agrees well with experimental results [98]. The form of $f(\Sigma)$, on the other hand, has been proposed in various forms [43, 112, 116, 117]. Here we use $f(\Sigma) = \exp(-\Sigma^*/\Sigma)$ [116, 117]. In the equations, γ^* and Σ^* are the characteristic strain and stress scales, respectively. The corresponding values have been reported in Chap. 4.

The suspension reaches a shear-jammed state when the terms in the square bracket in Eq. (5.3) becomes 0. As a result, we have

$$f(\Sigma_\infty)g(\gamma_\infty) = \frac{\phi_0 - \phi}{\phi_0 - \phi_m} \equiv 1 - \Phi, \qquad (5.4)$$

thus

$$\gamma_\infty(\Sigma_\infty) = g^{-1}\left[\frac{1 - \Phi}{f(\Sigma_\infty)}\right], \qquad (5.5)$$

where Φ is a rescaled packing fraction and g^{-1} is the inverse function of g. In the regime of high stress where $\Sigma_\infty \gg \Sigma^*$, $f(\Sigma_\infty) = 1$, thus $\gamma_\infty(\Sigma_\infty \gg \Sigma^*) = g^{-1}(1 - \Phi)$, which corresponds to $1/k_p$ in the high stress limit. Finally, we get the relation between k/k_p and Σ_∞:

$$\frac{k}{k_p} = \frac{1/\gamma_\infty(\Sigma)}{1/\gamma_\infty(\Sigma \gg \Sigma^*)} = \frac{g^{-1}(1 - \Phi)}{g^{-1}[(1 - \Phi)/f(\Sigma_\infty)]}. \qquad (5.6)$$

The results are presented in Fig. 5.4b, and we see the stress dependence of k in agreement with the experiments. Note that in the experiments, at stress above approximately 2000 Pa, k/k_p deviates from 1 and decreases. We suspect that this is due to excessive dilatancy of the system in the direction perpendicular to the $x-y$ plane shown in Fig. 5.1c, which was not confined in our experiments. In the model, we assume that ϕ is a constant, so any effect due to ϕ variation is not captured.

The agreement between the experiments and the model allows us to map out the boundary of the shear jamming regime in the state diagram, as shown in Fig. 5.5. From steady-state rheology experiments, we obtained ϕ_m, ϕ_0, and the stress scale Σ^* (see Chap. 4). As expected, shear jamming is only observed when ϕ is between ϕ_m (left) and ϕ_0 (right) labeled by the vertical dashed lines. The solid black curve shows the boundary of the DST regime. The lower part of this curve (the section with negative slope) labels the onset stress of DST Σ_{DST}. Experimental measurements from steady-state rheology with parallel plates (black squares) (Chaps. 4 and [98]) and wide-gap Couette cell (open squares) [28] lie right on top of this predicted boundary. This boundary, along with the mechanical properties of suspensions on the left side of ϕ_m, have been extensively studied by prior experiments [50, 109] and simulations [39, 41].

Fig. 5.5 State diagram.
Squares show Σ_{DST} obtained
from standard rheology with
parallel plates (black) [98]
and wide-gap Couette cell
(open) [28]. Solid circles
show the shear jamming
regime mapped out by our
experiments with transient
flows. Open circles are the
onset stress of SJ from Peters
et al. [28]. The red region
shows the DST regime and
the green curve shows Σ_{SJ}
(Eq. 5.7) predicted by the
Wyart–Cates model [43]
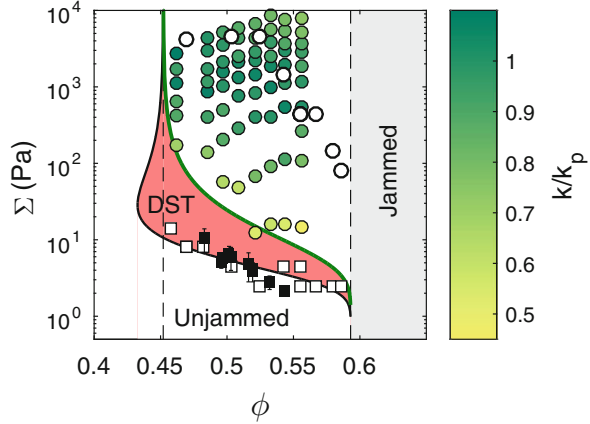
With the parameters ϕ_{m}, ϕ_0, and Σ^* obtained from rheology experiments, we can already predict Σ_{SJ} by setting $g(\gamma) = 1$, thus

$$\Sigma_{\mathrm{SJ}} = -\frac{\Sigma^*}{\ln(1 - \Phi)}. \tag{5.7}$$

It is shown by the solid green curve in Fig. 5.5, which our experiments now can test for the first time quantitatively. In a previous experiment by Peters et al., a stress boundary above which SJ is obtained was detected by poking the surface of sheared suspensions [28], and this boundary is shown by the open circles in Fig. 5.5. As we can see, it is significantly above what the model predicts. In comparison, our experimental method does a much better job detecting possible shear-jammed states at relatively low stress. The solid circles in Fig. 5.5 show the region where jamming fronts are observed, and their colors map out the corresponding k/k_{p}. Combining results shown in Figs. 5.4 and 5.5, we confirm that the Wyart–Cates model provides a reasonably good prediction of the threshold stress for shear jamming.

5.5   Conclusions

In this chapter, we pointed out that conventional steady-state rheology has limitations while testing suspensions in the regime where shear jamming is approached. To obtain flow curves for suspensions in this regime, we introduced a new method that takes advantage of transient shear fronts in a wide-gap linear shear cell. As the front propagates, the dense suspension behind the front evolves toward a shear-jammed state, and the stress of this jammed state can be controlled by the speed of the shearing boundary. This made it possible to map out the onset stress of shear jamming for different packing fractions and, for the first time, we showed

that the Wyart–Cates model well predicts the unset stress of shear jamming, and its generalization captures transient phenomena such as stress-dependent front propagation speed as well.

Chapter 6
Conclusions and Outlook

6.1 Conclusions

In this thesis, we presented a detailed investigation of the dynamics of dense particulate suspensions, focusing in particular on their transient dynamics. To achieve a better understanding of the rapidly evolving flows in such optically opaque materials, we developed a technique to image flows at high frame rate (up to 10,000 frames per second) with ultrasound. Firstly, we studied a phenomenon called the impact-activated solidification by combining the speed of sound measurements and high-speed imaging. Previous work had shown that impact at the surface of dense suspensions generates a front that propagates fast into the bulk, and transforms the material from a fluid-like state into a solid-like state in its wake. We achieved the first direct observation of such fronts in a three-dimensional system. Our speed of sound measurement revealed that, within the experimental error, there was no detectable increase in the packing fraction behind the front, which ruled out a model that relates the front propagation speed to (isotropic) jamming via densification [54, 60]. From the measured flow fields, we noted that the front formation is closely related to a narrow, propagating zone of high shear rate. Based on these observations, we concluded that impact-activated fronts are shear fronts. Furthermore, we showed that the front propagation speed is controlled by the accumulated strain needed for shear jamming. We explained the anisotropic front propagation speeds in the directions along and transverse to the impact by tracing its origin to the differences in the mode of shear experienced.

Next, to understand this shear front even better and model it quantitatively, we performed further experiments in a quasi-one-dimensional system, which is arguably the simplest geometry. We confirmed that the dimensionless front propagation speed is the inverse of the accumulated strain required to shear jam the suspension. This strain scale is the key that links steady-state rheology to transient flows. To prove this, we generalized the Wyart and Cates model [43] that was

developed to describe steady-state conditions by introducing a strain term. The experiment and theory matched very well both qualitatively and quantitatively.

Lastly, we extended the links between steady-state rheology and transient flows even further by realizing that transient flows can be used to study steady-state shear jamming, which is difficult, if not impossible, with conventional rheology experiments. We demonstrated that by using an experimental setup that corresponds to a shear flow across a sufficiently wide gap, we can drive suspensions to evolve towards shear jammed states at precisely controlled stress levels. Using this new method, we can then map out the onset stress for shear jamming in a state diagram for dense suspensions.

6.2   Outlook

Particulate suspensions are complex systems that involve interactions on a wide range of length scales. On the macroscopic level, the characteristic length scales are of order 1 mm. For example, in standard steady-state rheology, the gap size ranges from 10^{-4} to 10^{-2} m, and for shear fronts, the characteristic length scale is the front width, which is approximately 10^{-3}–10^{-2} m. A smaller length scale that matters is the particle size, which is in the range of 10^{-6}–10^{-4} m. Parameters on this scale include, but are not limited to, particle size, shape, and their spatial configuration, which all control the mechanical properties of the suspension. At an even smaller length scale, we have contact interactions between two particles, which is of order 10^{-9} m or less. Among different contact interactions between particles, a crucial one is "friction," which can be related to the frictional coefficient of the materials, the surface roughness of particles, the interactions between polymer brushes on the particle surfaces, or chemical interactions such as hydrogen bonds [47].

Comparatively, phenomena on the macroscopic length scales are the most well understood. Over the years, massive data have been collected by rheology experiments, on shear thinning, shear thickening, and recently, shear jamming. A separation of length scales allows us to model the macroscopic flows without considering details on the micron and nanometer levels. Till now, the mean-field theory by Wyart and Cates and our generalization of this model work reasonably well. With the state diagram $\eta(\phi, \Sigma)$, which has as few as four parameters (solvent viscosity η_0, frictionless and frictional jamming packing fractions ϕ_0 and ϕ_m, and a threshold stress scale Σ^*) all measurable on a rheometer, one can predict behaviors of suspensions under different steady-state driving conditions. Shear fronts constitute a clean, exemplary system that helps us reveal the links between steady flows and transient flows in such shear thickening fluids. With one more parameter, a threshold strain scale γ^*, qualitative or even quantitative predictions can be made. However, there are still many other transient phenomena that need to be included to enrich this model. In principle, our current model in one-dimension can be extended to three dimensions by considering the tensorial forms of strain and stress. Oscillatory shear is another useful model system to study transient flows,

especially for investigating the effect of strain. Last but not least, as discussed in Chap. 5, standard rheology techniques have certain limitations in the jammed regime. We demonstrated a new experimental method to overcome certain of these limitations, but clearly, there is still much room for improvement. It will be helpful if a standardized test for shear jamming materials can be added to the toolbox of rheologists.

When it comes to the micron and nanometer scales, the party has just started. The phenomenological models on macroscopic scales rely on the state diagram, but the parameters that are necessary to map out the diagram are all controlled by properties on the microscopic level. Understanding how microscopic interactions affect macroscopically measurable parameters will not only lead to deeper and richer physics but also guide us to design and engineer suspensions with expected properties. Currently, some of those links from micro to macro are still missing. For example, we expect that γ^* is related to the rearrangement of particle configuration in space, but most experiments that explore this relation are performed with quasi-static dry granular systems in two dimensions. To understand how microscopic properties affect macroscopic behaviors of real suspensions, we need to perform experiments on the microscopic level, for example, combine techniques such as confocal microscopy, x-ray scattering or tomography, and atomic force microscopy (AFM) with rheology experiments. Simulations are excellent tools for studying the effect of particle configurations, but until now numerical approaches have been mostly focusing on steady-state systems, where a relatively small system with several thousand particles is sufficient. When it comes to transient phenomena, however, the system might need to be much larger because of the emergence of other longer length scales such as the front width, and consequently, the computation will be more expensive.

In recent years, research on dense suspensions has progressed dramatically. New ideas are emerging, more powerful frameworks are being established, and bigger pictures are being drawn. The result is a rich field with tremendous opportunities as well as challenges, and surprises might appear on many different length scales.

Appendix A
Effective Density of
Non-density-Matched Suspensions

For non-density-matched suspensions, many models have been proposed for their effective density ρ_{eff} [87, 118–122]. Among them, Ament [87] better describes the experimental data [76, 97]. To model sound propagation there are two important length scales: the wavelength of the ultrasound λ and the length scale of the viscous layer δ. All the models described here only work in the regime where λ is much larger than the particle radius a. The thickness of the viscous layer can be expressed as

$$\delta = \sqrt{\frac{2\eta}{\omega \rho_{\text{l}}}}, \tag{A.1}$$

where $\omega = 2\pi f$ is the angular frequency of the ultrasound wave and η and ρ_{l} are the dynamic viscosity and density of the liquid in the suspension, respectively. The ratio a/δ is analogous to the Reynolds number. The system is in the inertial regime when $a/\delta \gg 1$ and in the Stokes regime when $a/\delta \ll 1$. In our experiments the suspensions were in the inertial regime.

Ament [87] derived a function for ρ_{eff} by considering the relative motion of particles and liquid in non-density-matched suspensions. He got

$$\rho_{\text{eff}} = \bar{\rho} - 2(\rho_{\text{s}} - \rho_{\text{l}})^2 \phi(1 - \phi) \frac{Q}{Q^2 + U^2} \tag{A.2}$$

where $\bar{\rho}$ is the mean density shown in Eq. (2.4), $Q = 2(\rho_{\text{s}} - \rho_{\text{l}})(1-\phi) + (\frac{9}{2}\frac{\delta}{a} + 3)\rho_{\text{l}}$, and $U = \frac{9}{2}\rho_{\text{l}}[\frac{\delta}{a} + (\frac{\delta}{a})^2]$. By plugging $\bar{\kappa}$ and ρ_{eff} into Eq. (2.2) we obtain the speed of sound c.

Appendix B
Preparation of Suspensions

The solid particles we used to make suspensions were cornstarch granules (producers: Ingredion and Roquette). They are non-spherical poly-disperse particles whose diameter ranges from 5 to 30 μm [54, 77], with an average of about 15 μm [123]. The density of cornstarch particles was $\rho_{cs} = (1.63 \pm 0.01) \times 10^3$ kg/m³ measured by density matching. Detailed procedure can be found in [76]. The suspending solvent was a mixture of cesium chloride (CsCl), glycerol, and deionized water. The mass ratio between glycerol and water in the solvent controlled its viscosity. The density of the solvent was $\rho_l = 1.62 \times 10^3$ kg/m³, which was matched to ρ_{cs} to prevent sedimentation.

When a suspension was prepared, we mixed m_{cs} grams of cornstarch particles with m_l grams of the solvent. The dry cornstarch particles were stored in a temperature and humidity controlled environment at $22.5 \pm 0.5\,°C$ and $44 \pm 2\%$ relative humidity (RH), so they contained some moisture before mixing [77]. Every m_{cs} grams of cornstarch dispersed into the solvent actually contained $(1 - \xi)m_{cs}$ grams of cornstarch "material" and ξm_{cs} grams of water. At 44% RH, the moisture content (mass fraction) ξ is approximately $13 \pm 1\%$ according to literature [77, 80]. The "material" volume fraction ϕ_M for cornstarch is

$$\phi_M = \frac{(1 - \xi)m_{cs}/\rho_{cs}}{(1 - \xi)m_{cs}/\rho_{cs} + m_l/\rho_l + \xi m_{cs}/\rho_w}, \tag{B.1}$$

where "w" represents water. Here ϕ_M specifically is the fraction of the volume occupied by the impermeable part of the amylose/amylopectin network that comprises the cornstarch particles. The mean density of the suspension $\bar{\rho}$ is also affected by the moisture content, and this in turn affects ρ_{eff} (Eq. A.2). If we assume that the water initially contained within the cornstarch particles completely mixes with the solvent, then

$$\bar{\rho} = \frac{m_{\mathrm{cs}} + m_{\mathrm{l}}}{(1 - \xi)m_{\mathrm{cs}}/\rho_{\mathrm{cs}} + m_{\mathrm{l}}/\rho_{\mathrm{l}} + \xi m_{\mathrm{cs}}/\rho_{\mathrm{w}}}. \tag{B.2}$$

As discussed in Sect. 2.4, the volume fraction ϕ occupied by the fully soaked particles is $\phi = \phi_{\mathrm{M}}/(1 - \psi)$ (Eq. 2.6), where $\psi = 0.31$ is the porosity of the cornstarch granules. In this thesis, the packing fractions we report are all calculated using Eqs. (B.1) and (2.6).

After mixing the particles and the solvent, we left the suspension to sit still for approximately 2 h before performing experiments to allow full wetting of the particles and for big air bubbles to escape. However, for ultrasound visualization, there were still too many bubbles after resting, as shown in Sect. 2.6. Therefore, the suspensions were debubbled before measurements. To prevent solvent evaporation during debubbling, we placed the mixed suspension samples into 10 or 50 mL syringes, sealed the nozzles with rubber septa, and withdrew the plungers to generate low pressure in the syringes. The walls of the syringes were tapped to liberate trapped bubbles. This method has proven effective in getting rid of bubbles in suspensions, as shown in Sect. 2.6.

The debubbled suspensions were almost entirely black in the ultrasound B-mode images. They were used directly in the speed of sound measurements. For imaging the flow field (e.g., Chap. 3), a small number of air bubbles were added back to the debubbled suspensions to act as tracer particles. This was done by slowly stirring the suspension, then tilting and slowly rotating the container till the bubbles were uniformly distributed.

With the speed of sound measurements, we confirmed two more properties of the suspensions: (1) The speed of sound in density-matched suspensions did not change with time over at least 16 h. (2) The cornstarch particles do not partially dissolve and thereby affect the solvent's speed of sound. To test the second point, we prepared suspension samples with cornstarch and DI water at different particle concentrations. The suspensions in this case were not density matched, so the particles settled. We decanted the clear supernatant after 2 h and measured its speed of sound. No significant difference was observed.

Appendix C
Relation Between k Value and Accumulated Strain in 2D

For an idealized 2D system, we define Cartesian coordinates with x-axis in the transverse direction and y-axis in the longitudinal direction. To obtain the relation between the strain threshold ε_c and the normalized front speeds k we consider how much shear strain a suspension element experiences when it accelerates from $u_y = 0$ to $u_y = U_p$. We consider the propagation in the transverse and longitudinal directions separately as two quasi-1D problems. Exemplary sketches of the velocity profiles are provided in Fig. C.1. The experimental data did not show a significant change in front width, so here we assume the shape of the front does not change during propagation. In this case, the velocity profiles can be expressed as

$$u_y(x, t) = f_t(x - v_{ft}t) \tag{C.1}$$

in the transverse direction and

$$u_y(y, t) = f_l(y - v_{fl}t) \tag{C.2}$$

in the longitudinal direction. In both equations t is the time, v_{ft} and v_{fl} are the front propagation speeds. $f_t(X)$ and $f_l(X)$ are the functions that satisfy $f_t = f_l = U_p$ as $X \to -\infty$ and $f_t = f_l = 0$ as $X \to +\infty$.

On either side of the impactor the front propagates transversely with a speed $v_{ft} = k_t U_p$, while the local velocity of the flow is perpendicular to the front propagation direction. The acceleration of a suspension element in the transverse direction is

$$\frac{Du_y(x, t)}{Dt} = \frac{\partial f_t}{\partial t} = -k_t U_p f_t' = -k_t U_p \frac{\partial u_y}{\partial x}, \tag{C.3}$$

where D/Dt is the material derivative and $f_t' = df_t(X)/dX$. Below the impactor there are two differences: one is that the suspension element now moves in the same direction as the front, and the other is $v_{fl} = (k_l + 1)U_p$ as defined in Eq. (3.5). Thus the acceleration becomes
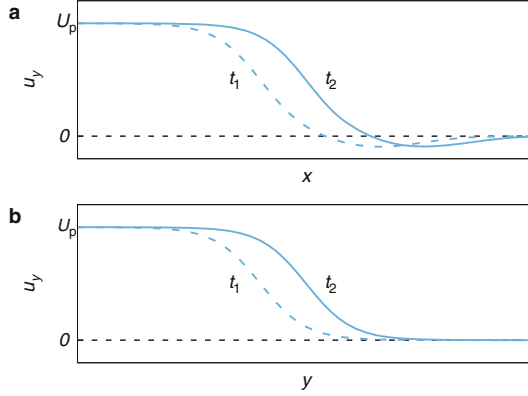
Fig. C.1 Schematic illustrations of the front profiles along the transverse (x) and longitudinal (y) directions in 2D. (**a**) Front profiles in the transverse direction at two times t_1 and t_2 ($t_2 > t_1$). In the jammed region $u_y = U_p$ and in the shear zone it drops quickly to zero. It goes slightly negative at larger x because of the circulation outside of the jammed region, which can be seen in Fig. 3.2. U_p returns back to zero far away from the impactor. (**b**) Front profiles in the longitudinal direction at t_1 and t_2. Both front profiles $f_t(x - U_{kt}t)$ and $f_l(y - U_{kl}t)$ approach U_p when x or $y \to 0$ and approach 0 when x or $y \to +\infty$

$$\frac{Du_y(y,t)}{Dt} = \frac{\partial f_1}{\partial t} + \left(u_y \frac{\partial}{\partial y}\right) f_1 = [u_y - (k_1 + 1)U_p]f_1'$$

$$= [u_y - (k_1 + 1)U_p]\frac{\partial u_y}{\partial y}. \tag{C.4}$$

Now we look at the relation between the local shear rate $\dot{\varepsilon}$ and the velocity gradient. In general, for an incompressible 2D fluid the shear rate tensor is

$$\dot{\boldsymbol{\varepsilon}} = \begin{bmatrix} \frac{\partial u_x}{\partial x} & \frac{1}{2}\left(\frac{\partial u_x}{\partial y} + \frac{\partial u_y}{\partial x}\right) \\ \frac{1}{2}\left(\frac{\partial u_x}{\partial y} + \frac{\partial u_y}{\partial x}\right) & \frac{\partial u_y}{\partial y} \end{bmatrix}, \tag{C.5}$$

where $\frac{\partial u_x}{\partial x} + \frac{\partial u_y}{\partial y} = 0$. From experimental observation, we have $\frac{\partial u_x}{\partial y} \ll \frac{\partial u_y}{\partial x}$. In the transverse direction, where simple shear dominates, the diagonal terms vanish and the shear rate tensor becomes

$$\dot{\boldsymbol{\varepsilon}}_t = \begin{bmatrix} 0 & \frac{1}{2}\frac{\partial u_y}{\partial x} \\ \frac{1}{2}\frac{\partial u_y}{\partial x} & 0 \end{bmatrix}, \tag{C.6}$$

while for pure shear in the longitudinal direction the off-diagonal terms vanish and we have

$$\dot{\boldsymbol{\varepsilon}}_1 = \begin{bmatrix} -\frac{\partial u_y}{\partial y} & 0 \\ 0 & \frac{\partial u_y}{\partial y} \end{bmatrix}. \tag{C.7}$$

In either case the matrix has two eigenvalues with the same magnitude but opposite sign and the eigenvalues represent the shear rate on the principal axes. Thus we can represent the shear intensities by the tensors' positive eigenvalues: $\dot{\boldsymbol{\varepsilon}}_1 = \left| \frac{\partial u_y}{\partial y} \right| = -\frac{\partial u_y}{\partial y}$ and $\dot{\boldsymbol{\varepsilon}}_t = \frac{1}{2} \left| \frac{\partial u_y}{\partial x} \right| = -\frac{1}{2} \frac{\partial u_y}{\partial x}$.

Using the velocity gradient, we relate the local shear rate with the acceleration of the element:

$$\dot{\varepsilon}_t = \frac{1}{2} \frac{1}{k_t U_p} \frac{Du_y}{Dt}, \tag{C.8}$$

$$\dot{\varepsilon}_1 = \frac{1}{(k_1 + 1)U_p - u_y} \frac{Du_y}{Dt}. \tag{C.9}$$

Consequently, the total shear strain ε a suspension element experiences before jamming is

$$\varepsilon_t = \int_0^\infty \dot{\varepsilon}_t dt = \int_0^{U_p} \frac{1}{2k_t U_p} du_y = \frac{1}{2k_t}, \tag{C.10}$$

and

$$\varepsilon_1 = \int_0^\infty \dot{\varepsilon}_1 dt = \int_0^{U_p} \frac{1}{(k_1 + 1)U_p - u_y} du_y = \ln\left(\frac{k_1 + 1}{k_1}\right). \tag{C.11}$$

Equation (C.11) gives $\varepsilon_1 \approx 1/k_1$ for $k_1 \gg 1$. If we assume the threshold strain to jamming ε_c is isotropic, then $k_t = 1/(2\varepsilon_c)$ and $k_1 = 1/(e^{\varepsilon_c} - 1)$.

Appendix D
Relation Between k_l and k_t in 3D

The shear rate tensor in three dimensions is shown in Eq. (3.1). In the longitudinal direction pure shear dominates and the shear rate tensor is

$$\dot{\boldsymbol{\varepsilon}}_1 = \begin{bmatrix} \frac{\partial u_r}{\partial r} & 0 & 0 \\ 0 & \frac{u_r}{r} & 0 \\ 0 & 0 & \frac{\partial u_z}{\partial z} \end{bmatrix}, \tag{D.1}$$

where $\frac{\partial u_r}{\partial r} \approx \frac{u_r}{r}$ and $\frac{\partial u_r}{\partial r} + \frac{u_r}{r} + \frac{\partial u_z}{\partial z} = 0$. In the transverse direction simple shear dominates. This gives

$$\dot{\boldsymbol{\varepsilon}}_t \approx \begin{bmatrix} 0 & 0 & \frac{1}{2}\frac{\partial u_z}{\partial r} \\ 0 & 0 & 0 \\ \frac{1}{2}\frac{\partial u_z}{\partial r} & 0 & 0 \end{bmatrix}, \tag{D.2}$$

where we have used $\frac{\partial u_r}{\partial z} \ll \frac{\partial u_z}{\partial r}$. Though the system is three dimensional, simple shear only operates in the rz plane while leaving the azimuthal direction invariant. The corresponding eigenvalues are $\dot{e}_1 = \left\{-\frac{1}{2}\frac{\partial u_z}{\partial z}, -\frac{1}{2}\frac{\partial u_z}{\partial z}, \frac{\partial u_z}{\partial z}\right\}$ and $\dot{e}_t = \left\{-\frac{1}{2}\frac{\partial u_z}{\partial r}, 0, \frac{1}{2}\frac{\partial u_z}{\partial r}\right\}$. Unlike the 2D case, we cannot simply use a positive eigenvalue to represent the shear intensity. However, we can define infinitesimal strains e_i ($i = 1, 2, 3$) along the three principal axes and rank-order them according to $e_1 > e_2 > e_3$. Following the definition given in Ref. [100], the "strain intensity" $\mathcal{D}$ is

$$\mathcal{D} = \sqrt{\left(\ln\frac{1+e_1}{1+e_2}\right)^2 + \left(\ln\frac{1+e_2}{1+e_3}\right)^2}$$
$$\approx \sqrt{(e_1 - e_2)^2 + (e_2 - e_3)^2}. \tag{D.3}$$

For pure shear in the longitudinal direction $e_1 = e_2 = -e_3/2$ and $\dot{e}_3 = \frac{\partial u_z}{\partial z}$, so $\mathcal{D}_l \approx \frac{3}{2}|e_3|$, which leads to $\dot{\mathcal{D}}_l \approx -\frac{3}{2}\frac{\partial u_z}{\partial z}$. For simple shear in the transverse direction $e_1 = -e_3$, $e_2 = 0$, and $\dot{e}_3 = \frac{1}{2}\frac{\partial u_z}{\partial r}$. This leads to $\mathcal{D}_t \approx \sqrt{2}|e_3|$, and therefore $\dot{\mathcal{D}}_t \approx -\frac{\sqrt{2}}{2}\frac{\partial u_z}{\partial r}$. Following the procedure for the 2D case we have

$$\dot{\mathcal{D}}_t = \frac{\sqrt{2}}{2}\frac{1}{k_t U_p}\frac{Du_z}{Dt}, \tag{D.4}$$

$$\dot{\mathcal{D}}_l = \frac{3}{2}\frac{1}{(k_l + 1)U_p - u_z}\frac{Du_z}{Dt}. \tag{D.5}$$

Integration then leads to

$$\mathcal{D}_t = \frac{\sqrt{2}}{2}\frac{1}{k_t}, \quad \mathcal{D}_l = \frac{3}{2}\ln\left(\frac{k_l + 1}{k_l}\right). \tag{D.6}$$

Now we again assume that the system shear-jams when $\mathcal{D}$ reaches a threshold strain value $\mathcal{D}_c$, independent of the type of shear it experiences. From this we find

$$k_l^* = \frac{1}{e^{\sqrt{2}/(3k_t^*)} - 1} \tag{D.7}$$

and $k_l^*/k_t^* \approx 3/\sqrt{2} \approx 2.12$ for large k.

There is another way to define a scalar that represents the magnitude of strain, and we label it as $\mathcal{E}$. For simplicity, here we write Eq. (3.1) as

$$\dot{\boldsymbol{\varepsilon}} = \begin{bmatrix} a & 0 & d \\ 0 & b & 0 \\ d & 0 & c \end{bmatrix}, \tag{D.8}$$

where $a + b + c = 0$ because the suspension is incompressible. We write the eigenvalues of the matrix in Eq. (D.8) as λ_1, λ_2, and λ_3, and sort them so that $|\lambda_1| \geq |\lambda_2| \geq |\lambda_3|$. Their values are

$$\lambda_1 = b$$
$$\lambda_{2,3} = -\frac{b}{2} \pm \frac{1}{2}\sqrt{(a - c)^2 + 4d^2}. \tag{D.9}$$

In this case, they each represent the strain rate along the corresponding principal axis. We can then write the diagonal matrix $\mathrm{diag}(\lambda_1, \lambda_2, \lambda_3)$ in the form

$$\dot{\boldsymbol{\varepsilon}} \sim \frac{2\dot{\mathcal{E}}}{\sqrt{3+4\alpha^2}} \begin{bmatrix} 1 & 0 & 0 \\ 0 & -(\frac{1}{2}+\alpha) & 0 \\ 0 & 0 & -(\frac{1}{2}-\alpha) \end{bmatrix}, \tag{D.10}$$

where $\alpha = \frac{\sqrt{(a-c)^2+4d^2}}{2|b|} \in [0, 1/2]$ and $\dot{\mathcal{E}} = \sqrt{(\lambda_1^2 + \lambda_2^2 + \lambda_3^2)/2}$. For the uniaxial compression in z with isotropic flow in the $x-y$ plane,

$$\dot{\boldsymbol{\varepsilon}} = \begin{bmatrix} -\frac{1}{2}\frac{\partial u_z}{\partial z} & 0 & 0 \\ 0 & -\frac{1}{2}\frac{\partial u_z}{\partial z} & 0 \\ 0 & 0 & \frac{\partial u_z}{\partial z} \end{bmatrix}. \tag{D.11}$$

Thus in the longitudinal direction, we have $\alpha = 0$ and

$$\dot{\mathcal{E}}_l = \frac{\sqrt{3}}{2} \cdot \frac{\partial u_z}{\partial z}. \tag{D.12}$$

For the simple shear in the $x-z$ plane, we have

$$\dot{\boldsymbol{\varepsilon}} = \begin{bmatrix} 0 & 0 & \frac{1}{2}\frac{\partial u_z}{\partial r} \\ 0 & 0 & 0 \\ \frac{1}{2}\frac{\partial u_z}{\partial r} & 0 & 0 \end{bmatrix}. \tag{D.13}$$

In this case $\alpha = 1/2$ and

$$\dot{\mathcal{E}}_t = \frac{1}{2} \cdot \frac{\partial u_z}{\partial r}. \tag{D.14}$$

Here we have ignored $\partial u_r/\partial z$ in the non-diagonal terms because it is much smaller than $\partial u_z/\partial r$. Following the ideas of Eqs. (D.4) and (D.5), we get

$$\mathcal{E}_l = \frac{\sqrt{3}}{2}\ln\left(\frac{k_l+1}{k_l}\right) \approx \frac{\sqrt{3}}{2k_l},$$

$$\mathcal{E}_t = \frac{1}{2k_t}. \tag{D.15}$$

Again, if the threshold strain is the same for any direction, $\mathcal{E}_l = \mathcal{E}_t$, we obtain

$$\frac{k_l}{k_t} \approx \sqrt{3} \approx 1.73. \tag{D.16}$$

Appendix E
Some Calculations Regarding
the Generalized Model

Equation (4.19) is an approximate relation between γ_∞ and γ^* in the regime of sufficiently fast U_0, where the front speed is constant. To keep the calculation simple, we make three approximations that are appropriate for this high-speed limit: First, we approximate Eq. (4.11) by

$$\Sigma \approx \widetilde{\eta}_0 \cdot \dot{\gamma} \left[\phi_{\text{eff}} - \phi \right]^{-2}, \tag{E.1}$$

where $\widetilde{\eta}_0 \equiv \eta_0 \phi_0^2$. Second, in this limit Σ is much larger than Σ^*, so we take $f(\Sigma) \approx 1$. Finally, since the front profile has an approximately invariant shape while propagating, the accumulated strain can be written as $\gamma(x, t) = \gamma(U_{\text{f}}t - x) \equiv \gamma(X)$. This leads to

$$\gamma' \equiv \frac{d\gamma(X)}{dX} = \frac{1}{U_{\text{f}}} \frac{\partial \gamma}{\partial t} = -\frac{\partial \gamma}{\partial x}, \tag{E.2}$$

and

$$\gamma'' \equiv \frac{d^2\gamma(X)}{dX^2} = \frac{1}{U_{\text{f}}^2} \frac{\partial^2 \gamma}{\partial t^2} = \frac{\partial^2 \gamma}{\partial x^2}. \tag{E.3}$$

Plugging Eq. (E.1) into the equation of motion:

$$\rho \frac{\partial^2 \gamma}{\partial t^2} = \frac{\partial^2 \Sigma}{\partial x^2}, \tag{E.4}$$

we get

$$\rho \frac{\partial^2 \gamma}{\partial t^2} = \frac{\partial^2}{\partial x^2} \left\{ \frac{\widetilde{\eta}_0 \dot{\gamma}}{[(\phi_0 - \phi_{\text{m}})e^{-\gamma/\gamma^*} + \phi_{\text{m}} - \phi]^2} \right\}. \tag{E.5}$$

Using Eqs. (E.2) and (E.3), we obtain

$$\frac{d^2}{dX^2}\left\{\rho U_f^2 \gamma - \frac{\widetilde{\eta}_0 U_f \gamma'}{[(\phi_0 - \phi_m)e^{-\gamma/\gamma^*} + \phi_m - \phi]^2}\right\} = 0,$$

which leads to

$$\rho U_f^2 \gamma - \frac{\widetilde{\eta}_0 U_f \gamma'}{[(\phi_0 - \phi_m)e^{-\gamma/\gamma^*} + \phi_m - \phi]^2} = C_1 X + C_2, \tag{E.6}$$

where C_1 and C_2 are constants. In the region not yet reached by the front, both γ and γ' are zero. This means that as $X \to -\infty$ (at large x or small t), the left-hand side of Eq. (E.6) is zero, so the constants should be $C_1 = C_2 = 0$, and we obtain a first order equation governing the evolution of γ:

$$\frac{d\gamma}{dX} = \frac{\rho U_f}{\widetilde{\eta}_0}\gamma \cdot \left[(\phi_0 - \phi_m)e^{-\gamma/\gamma^*} + \phi_m - \phi\right]^2. \tag{E.7}$$

It has two fixed points. For any given x, γ increases with time from an unstable fixed point $\gamma = 0$ to a half-stable fixed point, which is the asymptotic accumulated strain in Eq. (4.19):

$$\gamma_\infty = \gamma^* \cdot \ln\frac{\phi_0 - \phi_m}{\phi - \phi_m}.$$

Written as a function of the rescaled packing fraction Φ defined in Eq. (4.7), it becomes

$$\gamma_\infty = -\gamma^* \ln\Phi. \tag{E.8}$$

This approximate result captures the relation between γ_∞ and γ^* very well. In Fig. E.1a we compare the numerically calculated k and γ_∞ at $\gamma^* = 0.197$ and $U_0 = 1$ m/s with Eq. (4.19).

Using Eqs. (E.2) and (E.7), we can write out the expression for the shear rate:

$$\dot{\gamma} = \left\{\frac{\rho k^2}{\widetilde{\eta}_0}\gamma \cdot \left[(\phi_0 - \phi_m)e^{-\gamma/\gamma^*} + \phi_m - \phi\right]^2\right\}U_0^2, \tag{E.9}$$

where we have replaced U_f by kU_0. The maximum shear rate $\dot{\gamma}_{max}$ is achieved at γ_m, where the function in the curly brackets reaches its peak. By calculating the first derivative, we find that this occurs when

$$e^{-\gamma_m/\gamma^*}\left(1 - 2\frac{\gamma_m}{\gamma^*}\right) = \Phi. \tag{E.10}$$
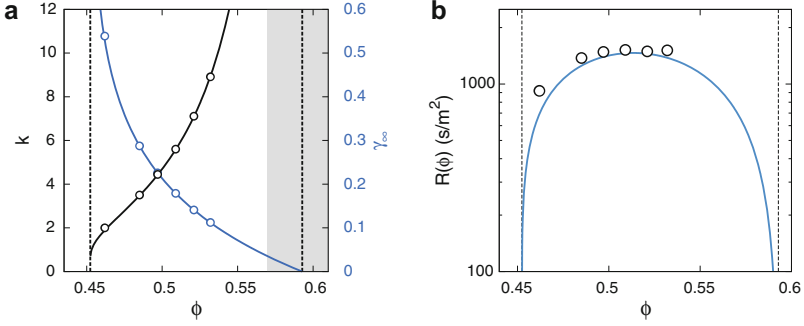
Fig. E.1 (a) Dimensionless front propagation speed k and asymptotic accumulated strain γ_∞ at different packing fraction ϕ obtained numerically at $\gamma^* = 0.197$ and $U_0 = 1$ m/s. The solid curves show Eq. (4.19) and its reciprocal at the same γ^*. (b) Comparison of $R(\phi)$ obtained from the numerical calculation (open circles) with the prediction of Eq. (E.9) (blue line). The dashed black lines show ϕ_m and ϕ_0

This can be evaluated numerically to find γ_m. Plugging γ_m into Eq. (E.9), everything in the curly brackets are independent of U_0. As a result, the prediction of the maximum shear rate by the model can be written as

$$\dot{\gamma}_{max} = R(\phi) \cdot U_0^2, \tag{E.11}$$

where the pre-factor $R(\phi)$ is simply a function of the packing fraction. As shown in Fig. E.1b, $R(\phi)$ vanishes as $\phi \to \phi_0$ and $\phi \to \phi_m$, but in the range $\phi \in$ [0.462, 0.532], it is relatively flat. This agrees well with the numerical results shown in Fig. 4.4d in the main text. To extract $R(\phi)$ we fit the numerically calculated $\dot{\gamma}_{max}(U_0)$ at each ϕ to Eq. (E.11). The results are given by the open circles in Fig. E.1b.

References

1. H.A. Barnes, J.F. Hutton, K. Walters, *An Introduction to Rheology* (Elsevier, Amsterdam, 1989)
2. L.D. Landau, E.M. Lifshitz, *Theory of Elasticity*, 2nd edn. (Pergamon Press, Oxford, 1970)
3. D.J. Acheson, *Elementary Fluid Dynamics* (Oxford University Press, Oxford, 2005)
4. A. Einstein, A new determination of the molecular dimensions. Ann. Phys. **19**, 289–306 (1906)
5. G.K. Batchelor, The effect of Brownian motion on the bulk stress in a suspension of spherical particles. J. Fluid Mech. **83**(01), 97 (1977)
6. R.C. Ball, P. Richmond, Dynamics of colloidal dispersions. Phys. Chem. Liq. **9**(2), 99–116 (1980)
7. A.J. Liu, S.R. Nagel, Jamming is not just cool any more. Nature **396**(6706), 21–22 (1998)
8. M.E. Cates, J.P. Wittmer, J.P. Bouchaud, P. Claudin, Jamming force chains and fragile matter. Phys. Rev. Lett. **81**(9), 4 (1998)
9. S.H. Maron, P.E. Pierce, Application of ree-eyring generalized flow theory to suspensions of spherical particles. J. Colloid Sci. **11**, 80–95 (1956)
10. I.M. Krieger, T.J. Dougherty, A mechanism for non-Newtonian flow in suspensions of rigid spheres. Trans. Soc. Rheol. **3**(1), 137–152 (1959)
11. J.F. Brady, The rheological behavior of concentrated colloidal dispersions. J. Chem. Phys. **99**(1), 567–581 (1993)
12. H.M. Shewan, J.R. Stokes, Analytically predicting the viscosity of hard sphere suspensions from the particle size distribution. J. Non-Newtonian Fluid Mech. **222**, 72–81 (2015)
13. E. Brown, H.M. Jaeger, Shear thickening in concentrated suspensions: phenomenology, mechanisms and relations to jamming. Rep. Prog. Phys. **77**(4), 046602 (2014)
14. V. Trappe, V. Prasad, L. Cipelletti, P.N. Segre, D.A. Weitz, Jamming phase diagram for attractive particles. Nature **411**, 772–775 (2001)
15. E. Brown, N.A. Forman, C.S. Orellana, H. Zhang, B.W. Maynor, D.E. Betts, J.M. DeSimone, H.M. Jaeger, Generality of shear thickening in dense suspensions. Nat. Mater. **9**(3), 220–224 (2010)
16. B.J. Maranzano, N.J. Wagner, The effects of particle size on reversible shear thickening of concentrated colloidal dispersions. J. Chem. Phys. **114**(23), 10514–10527 (2001)
17. X. Cheng, J.H. McCoy, J.N. Israelachvili, I. Cohen, Imaging the microscopic structure of shear thinning and thickening colloidal suspensions. Science **333**, 1276–1279 (2011)
18. E. Brown, H.M. Jaeger, Through thick and thin. Science **333**, 1230–1231 (2011)
19. N.J. Wagner, J.F. Brady, Shear thickening in colloidal dispersions. Phys. Today **62**(10), 27–32 (2009)

20. J.F. Brady, G. Bossis, The rheology of concentrated suspensions of spheres in simple shear flow by numerical simulation. J. Fluid Mech. **155**, 105 (1985)
21. J.F. Brady, G Bossis, Stokesian dynamics. Annu. Rev. Fluid Mech. **20**, 111 (1988)
22. H.A. Barnes, Shear-thickening ("dilatancy") in suspensions of nonaggregating solid particles dispersed in Newtonian liquids. J. Rheol. **33**(2), 329 (1989)
23. E. Brown, H.M. Jaeger, The role of dilation and confining stresses in shear thickening of dense suspensions. J. Rheol. **56**(4), 875 (2012)
24. Q. Xu, S. Majumdar, E. Brown, H.M. Jaeger, Shear thickening in highly viscous granular suspensions. Europhys. Lett. **107**(6), 68004 (2014)
25. N.Y. Lin, B.M. Guy, M. Hermes, C. Ness, J. Sun, W.C. Poon, I. Cohen, Hydrodynamic and contact contributions to continuous shear thickening in colloidal suspensions. Phys. Rev. Lett. **115**(22), 228304 (2015)
26. C.S. O'Hern, L.E. Silbert, A.J. Liu, S.R. Nagel, Jamming at zero temperature and zero applied stress: the epitome of disorder. Phys. Rev. E **68**(1), 011306 (2003)
27. D. Bi, J. Zhang, B. Chakraborty, R.P. Behringer, Jamming by shear. Nature **480**(7377), 355–358 (2011)
28. I.R. Peters, S. Majumdar, H.M. Jaeger, Direct observation of dynamic shear jamming in dense suspensions. Nature **532**(7598), 214–217 (2016)
29. N. Kumar, S. Luding, Memory of jamming–multiscale models for soft and granular matter. Granul. Matter **18**(3), 58 (2016)
30. W. Zheng, H. Liu, N. Xu, Shear-induced solidification of athermal systems with weak attraction. Phys. Rev. E **94**(6), 062608 (2016)
31. E. DeGiuli, G. Düring, E. Lerner, M. Wyart, Unified theory of inertial granular flows and non-Brownian suspensions. Phys. Rev. E **91**(6), 062206 (2015)
32. E. Lerner, G. Düring, M. Wyart, A unified framework for non-Brownian suspension flows and soft amorphous solids. Proc. Natl. Acad. Sci. **109**(13), 4798–4803 (2012)
33. N. Fernandez, R. Mani, D. Rinaldi, D. Kadau, M. Mosquet, H. Lombois-Burger, J. Cayer-Barrioz, H.J. Herrmann, N.D. Spencer, L. Isa, Microscopic mechanism for shear thickening of non-Brownian suspensions. Phys. Rev. Lett. **111**(10), 108301 (2013)
34. F. Boyer, E. Guazzelli, O. Pouliquen, Unifying suspension and granular rheology. Phys. Rev. Lett. **107**(18), 188301 (2011)
35. J.R. Royer, D.L. Blair, S.D. Hudson, Rheological signature of frictional interactions in shear thickening suspensions. Phys. Rev. Lett. **116**(18), 188301 (2016)
36. J. Comtet, G. Chatte, A. Nigues, L. Bocquet, A. Siria, A. Colin, Pairwise frictional profile between particles determines discontinuous shear thickening transition in non-colloidal suspensions. Nat. Commun. **8**, 15633 (2017)
37. C. Clavaud, A. Berut, B. Metzger, Y. Forterre, Revealing the frictional transition in shear-thickening suspensions. Proc. Natl. Acad. Sci. **114**(20), 5147–5152 (2017)
38. R. Seto, R. Mari, J.F. Morris, M.M. Denn, Discontinuous shear thickening of frictional hard-sphere suspensions. Phys. Rev. Lett. **111**(21), 218301 (2013)
39. R. Mari, R. Seto, J.F. Morris, M.M. Denn, Nonmonotonic flow curves of shear thickening suspensions. Phys. Rev. E **91**(5), 052302 (2015)
40. C. Ness, J. Sun, Shear thickening regimes of dense non-Brownian suspensions. Soft Matter **12**(3), 914–924 (2016)
41. A. Singh, R. Mari, M.M. Denn, J.F. Morris, A constitutive model for simple shear of dense frictional suspensions. J. Rheol. **62**(2), 457–468 (2018)
42. S. Sarkar, D. Bi, J. Zhang, J. Ren, R.P. Behringer, B. Chakraborty, Shear-induced rigidity of frictional particles: analysis of emergent order in stress space. Phys. Rev. E **93**(4), 042901 (2016)
43. M. Wyart, M.E. Cates, Discontinuous shear thickening without inertia in dense non-Brownian suspensions. Phys. Rev. Lett. **112**(9), 098302 (2014)
44. C. Song, P. Wang, H.A. Makse, A phase diagram for jammed matter. Nature **453**(7195), 629–632 (2008)

45. L.C. Hsiao, S. Jamali, E. Glynos, P.F. Green, R.G. Larson, M.J. Solomon, Rheological state diagrams for rough colloids in shear flow. Phys. Rev. Lett. **119**(15), 158001 (2017)
46. C.P. Hsu, S.N. Ramakrishna, M. Zanini, N.D. Spencer, L. Isa, Roughness-dependent tribology effects on discontinuous shear thickening. Proc. Natl. Acad. Sci. **115**(20), 5117–5122 (2018)
47. N.M. James, E. Han, R.A.L. de la Cruz, J. Jureller, H.M. Jaeger, Interparticle hydrogen bonding can elicit shear jamming in dense suspensions. Nat. Mater. **17**(11), 965–970 (2018)
48. M. Trulsson, E. DeGiuli, M. Wyart, Effect of friction on dense suspension flows of hard particles. arXiv preprint arXiv:1606.07650 (2016)
49. F. Blanc, F. Peters, E. Lemaire, Local transient rheological behavior of concentrated suspensions. J. Rheol. **55**(4), 835–854 (2011)
50. B.M. Guy, M. Hermes, W.C. Poon, Towards a unified description of the rheology of hard-particle suspensions. Phys. Rev. Lett. **115**(8), 088304 (2015)
51. Z. Pan, H. de Cagny, B. Weber, D. Bonn, S-shaped flow curves of shear thickening suspensions: direct observation of frictional rheology. Phys. Rev. E Stat. Nonlinear Soft Matter Phys. **92**(3), 032202 (2015)
52. B. Liu, M. Shelley, J. Zhang, Focused force transmission through an aqueous suspension of granules. Phys. Rev. Lett. **105**(18), 188301 (2010)
53. S. von Kann, J.H. Snoeijer, D. Lohse, D. van der Meer, Nonmonotonic settling of a sphere in a cornstarch suspension. Phys. Rev. E **84**(6), 060401 (2011)
54. S.R. Waitukaitis, H.M. Jaeger, Impact-activated solidification of dense suspensions via dynamic jamming fronts. Nature **487**(7406), 205–209 (2012)
55. M. Roche, E. Myftiu, M.C. Johnston, P. Kim, H.A. Stone, Dynamic fracture of nonglassy suspensions. Phys. Rev. Lett. **110**(14), 148304 (2013)
56. R. Maharjan, S. Mukhopadhyay, B. Allen, T. Storz, E. Brown, Constitutive relation for the system-spanning dynamically jammed region in response to impact of cornstarch and water suspensions. Phys. Rev. E **97**(5), 052602 (2018)
57. B. Allen, B. Sokol, S. Mukhopadhyay, R. Maharjan, E. Brown, System-spanning dynamically jammed region in response to impact of cornstarch and water suspensions. Phys. Rev. E **97**(5), 052603 (2018)
58. M.I. Smith, R. Besseling, M.E. Cates, V. Bertola, Dilatancy in the flow and fracture of stretched colloidal suspensions. Nat. Commun. **1**, 114 (2010)
59. I.R. Peters, H.M. Jaeger, Quasi-2d dynamic jamming in cornstarch suspensions: visualization and force measurements. Soft Matter **10**(34), 6564–6570 (2014)
60. S.R. Waitukaitis, L.K. Roth, V. Vitelli, H.M. Jaeger, Dynamic jamming fronts. Europhys. Lett. **102**(4), 44001 (2013)
61. S.R. Nagel, Experimental soft-matter science. Rev. Mod. Phys. **89**(2), 025002 (2017)
62. M.L. Cowan, I.P. Jones, J.H. Page, D.A. Weitz, Diffusing acoustic wave spectroscopy. Phys. Rev. E **65**, 066605 (2002)
63. S. Manneville, L. Bécu, A. Colin, High-frequency ultrasonic speckle velocimetry in sheared complex fluids. Eur. Phys. J. Appl. Phys. **28**(3), 361–373 (2004)
64. T. Gallot, C. Perge, V. Grenard, M.A. Fardin, N. Taberlet, S. Manneville, Ultrafast ultrasonic imaging coupled to rheometry: principle and illustration. Rev. Sci. Instrum. **84**(4), 045107 (2013)
65. X. Jia, C. Caroli, B. Velicky, Ultrasound propagation in externally stressed granular media. Phys. Rev. Lett. **82**(9), 1863–1866 (1999)
66. Y. Khidas, X. Jia, Anisotropic nonlinear elasticity in a spherical-bead pack: influence of the fabric anisotropy. Phys. Rev. E Stat. Nonlin. Soft Matter Phys. **81**(2 Pt 1), 021303 (2010)
67. S. van den Wildenberg, Y. Yang, X. Jia, Probing the effect of particle shape on the rigidity of jammed granular solids with sound speed measurements. Granul. Matter **17**(4), 419–426 (2015)
68. V. Langlois, X. Jia, Acoustic probing of elastic behavior and damage in weakly cemented granular media. Phys. Rev. E Stat. Nonlin. Soft Matter Phys. **89**(2), 023206 (2014)
69. R.S.C. Cobbold, *Foundations of Biomedical Ultrasound* (Oxford University Press, Oxford, 2007)

70. C. Errico, J. Pierre, S. Pezet, Y. Desailly, Z. Lenkei, O. Couture, M. Tanter, Ultrafast ultrasound localization microscopy for deep super-resolution vascular imaging. Nature **527**(7579), 499–502 (2015)

71. N. Goldenfeld, L.P. Kadanoff, Simple lessons from complexity. Science **284**, 87–89 (1999)

72. R.J. Urick, A sound velocity method for determining the compressibility of finely divided substances. J. Appl. Phys. **18**(11), 983 (1947)

73. A.B. Wood, *A Textbook of Sound* (G. Bell, London, 1941)

74. V.A. Del Grosso, C.W. Mader, Speed of sound in pure water. J. Acoust. Soc. Am. **52**(5B), 1442–1446 (1972)

75. N. Bilaniuk, G.S.K. Wong, Speed of sound in pure water as a function of temperature. J. Acoust. Soc. Am. **93**(3), 1609–1612 (1993)

76. E. Han, N. Van Ha, H.M. Jaeger, Measuring the porosity and compressibility of liquid-suspended porous particles using ultrasound. Soft Matter **13**(19), 3506–3513 (2017)

77. R.L. Whistler, J.N. Bemiller, E.F. Paschall, *Starch: Chemistry and Technology*, 2nd edn. (Academic, Cambridge, 1984)

78. R.F. Tester, J. Karkalas, X. Qi, Starch - composition, fine structure and architecture. J. Cereal Sci. **39**(2), 151–165 (2004)

79. N.H. Hellman, E.H. Melvin, Surface area of starch and its role in water sorption. J. Am. Chem. Soc. **72**, 5186–5188 (1950)

80. L. Sair, W.R. Fetzer, Water sorption by starches. Ind. Eng. Chem. **36**(3), 205–208 (1944)

81. E. Brown, H.M. Jaeger, Dynamic jamming point for shear thickening suspensions. Phys. Rev. Lett. **103**(8), 086001 (2009)

82. F. Gassmann, Uber die elastizitat poroser medien. Ver. Natur. Gesellschaft **96**, 1–23 (1951)

83. M.A. Biot, Theory of propagation of elastic waves in a fluid saturated porous solid. I. low-frequency range. J. Acoust. Soc. Am. **28**, 168–178 (1956)

84. R.J.S. Brown, J. Korringa, On the dependence of the elastic properties of a porous rock on the compressibility of the pore fluid. Geophysics **40**(4), 9 (1975)

85. M.L. Batzle, D. Han, R. Hofmann, Fluid mobility and frequency-dependent seismic velocity - direct measurements. Geophysics **71**(1), N1–N9 (2006)

86. D.L. Johnson, Theory of frequency dependent acoustics in patchy-saturated porous media. J. Acoust. Soc. Am. **110**(2), 682–694 (2001)

87. W.S. Ament, Sound propagation in gross mixtures. J. Acoust. Soc. Am. **25**(4), 638–641 (1953)

88. L. Gibiansky, S. Torquato, Rigorous connection between physical properties of porous rocks. J. Geophys. Res. **103**(B10), 23911–23932 (1998)

89. W. Pabst, E. Gregorova, G. Ticha, Elasticity of porous ceramics - a critical study of modulus - porosity relations. J. Eur. Ceram. Soc. **26**(7), 1085–1097 (2006)

90. S.R. Waitukaitis, Impact activated solidification of cornstarch and water suspensions. Thesis, The University of Chicago (2014)

91. G.N. Greaves, A.L. Greer, R.S. Lakes, T. Rouxel, Poisson's ratio and modern materials. Nat. Mater. **10**(11), 823–837 (2011)

92. E. Han, I.R. Peters, H.M. Jaeger, High-speed ultrasound imaging in dense suspensions reveals impact-activated solidification due to dynamic shear jamming. Nat. Commun. **7**, 12243 (2016)

93. O.E. Petel, S. Ouellet, J. Loiseau, D.L. Frost, A.J. Higgins, A comparison of the ballistic performance of shear thickening fluids based on particle strength and volume fraction. Int. J. Impact Eng. **85**, 83–96 (2015)

94. E.J. Windhab, B. Ouriev, Rheological study of concentrated suspensions in pressure-driven shear flow using a novel in-line ultrasound Doppler method. Exp. Fluids **32**(2), 204–211 (2002)

95. B. Ouriev, E.J. Windhab, Novel ultrasound based time averaged flow mapping method for die entry visualization in flow of highly concentrated shear-thinning and shear-thickening suspensions. Meas. Sci. Technol. **14**, 140–147 (2003)

96. B. Saint-Michel, H. Bodiguel, S. Meeker, S. Manneville, Simultaneous concentration and velocity maps in particle suspensions under shear from rheo-ultrasonic imaging. Phys. Rev. Appl. **8**(1), 014023 (2017)
97. D.J. McClements, M.J.W. Povey, Ultrasound velocity as a probe. Adv. Colloid Interf. Sci. **27**, 285–316 (1987)
98. E. Han, M. Wyart, I.R. Peters, H.M. Jaeger, Shear fronts in shear-thickening suspensions. Phys. Rev. Fluids **3**(7), 073301 (2018)
99. V. Vitelli, M. van Hecke, Marginal matters. Nature **480**, 325–326 (2011)
100. J.G. Ramsay, M.I. Huber, *The Techniques of Modern Structural Geology*, vol. 1, 1st edn. (Academic, Cambridge, 1983)
101. E. Han, L. Zhao, N. Van Ha, S.T. Hsieh, D.B. Szyld, H.M. Jaeger, Dynamic jamming of dense suspensions under tilted impact. Phys. Rev. Fluids **4**, 063304 (2019)
102. S. Majumdar, I.R. Peters, E. Han, H.M. Jaeger, Dynamic shear jamming under extension in dense granular suspensions. Phys. Rev. E **95**, 012603 (2017)
103. L.R. Gomez, A.M. Turner, M. van Hecke, V. Vitelli, Shocks near jamming. Phys. Rev. Lett. **108**(5), 058001 (2012)
104. L.R. Gomez, A.M. Turner, V. Vitelli, Uniform shock waves in disordered granular matter. Phys. Rev. E **86**(4), 041302 (2012)
105. S. Ulrich, N. Upadhyaya, B. van Opheusden, V. Vitelli, Shear shocks in fragile networks. Proc. Natl. Acad. Sci. **110**(52), 20929–20934 (2013)
106. S.R. Waitukaitis, L.K. Roth, V. Vitelli, H.M. Jaeger, Dynamic jamming fronts. Europhys. Lett. **102**(4), 44001 (2013)
107. I. Buttinoni, J. Cha, W.H. Lin, S. Job, C. Daraio, L. Isa, Direct observation of impact propagation and absorption in dense colloidal monolayers. Proc. Natl. Acad. Sci. **114**(46), 12150–12155 (2017)
108. M.E. Cates, M. Wyart, Granulation and bistability in non-Brownian suspensions. Rheol. Acta **53**(10-11), 755–764 (2014)
109. M. Hermes, B.M. Guy, W.C.K. Poon, G. Poy, M.E. Cates, M. Wyart, Unsteady flow and particle migration in dense, non-Brownian suspensions. J. Rheol. **60**(5), 905–916 (2016)
110. M. Pailha, M. Nicolas, O. Pouliquen, Initiation of underwater granular avalanches: influence of the initial volume fraction. Phys. Fluids **20**(11), 111701 (2008)
111. R. Mari, R. Seto, J.F. Morris, M.M. Denn, Shear thickening, frictionless and frictional rheologies in non-Brownian suspensions. J. Rheol. **58**(6), 1693–1724 (2014)
112. H. Nakanishi, S. Nagahiro, N. Mitarai, Fluid dynamics of dilatant fluids. Phys. Rev. E **85**(1), 011401 (2012)
113. B. Saint-Michel, T. Gibaud, S. Manneville, Uncovering instabilities in the spatiotemporal dynamics of a shear-thickening cornstarch suspension. Phys. Rev. X **8**(3), 031006 (2018)
114. V. Rathee, D.L. Blair, J.S. Urbach, Localized stress fluctuations drive shear thickening in dense suspensions. Proc. Natl. Acad. Sci. U.S.A. **114**(33), 8740–8745 (2017)
115. W.H. Boersma, P.J.M. Baets, J. Laven, H.N. Stein, Time-dependent behavior and wall slip in concentrated shear thickening dispersions. J. Rheol. **35**(6), 1093–1120 (1991)
116. A. Singh, R. Mari, M.M. Denn, J.F. Morris, A constitutive model for simple shear of dense frictional suspensions. J. Rheol. **62**(2), 457–468 (2018)
117. R.N. Chacko, R. Mari, M.E. Cates, S.M. Fielding, Dynamic vorticity banding in discontinuously shear thickening suspensions. Phys. Rev. Lett. **121**(10), 108003 (2018)
118. R.J. Urick, W.S. Ament, The propagation of sound in composite media. J. Acoust. Soc. Am. **21**(3), 115–119 (1949)
119. A.H. Harker, J.A.G. Temple, Velocity and attenuation of ultrasound in suspensions of particles in fluids. J. Phys. D Appl. Phys. **21**, 1576–1588 (1988)
120. H.K. Kytomaa, C.M. Atkinson, Sound propagation in suspensions and acoustic imaging of their microstructure. Mech. Mater. **16**, 189–197 (1993)

121. H.K. Kytomaa, Theory of sound propagation in suspensions: a guide to particle size and concentration characterization. Powder Technol. **82**, 115–121 (1995)
122. L. Schwartz, T.J. Plona, Ultrasonic propagation in close-packed disordered suspensions. J. Appl. Phys. **55**(11), 3971 (1984)
123. J.L. Paterson, A. Hardacre, P. Li, M.A. Rao, Rheology and granule size distributions of cornstarch dispersions from two genotypes and grown in four regions. Food Hydrocoll. **15**, 453–459 (2001)